Search for New Physics in the e + MET Final State in the 2016 CMS Dataset

von

Sebastian Wiedenbeck

Masterarbeit in Physik

vorgelegt der

Fakultät für Mathematik, Informatik und Naturwissenschaften der RWTH Aachen University

im Februar 2018

angefertigt im

III. Physikalisches Institut A

bei

Prof. Dr. Thomas Hebbeker

Zweitgutachter:

Prof. Dr. Christopher Wiebusch

Abstract

This thesis presents the search for new phyics in the electron plus missing transverse energy final state in proton-proton collisions at the LHC with a center-of-mass energy of $\sqrt{s} = 13\,\text{TeV}$. It uses recorded data provided by the CMS experiment in 2016 of $35.9\,\text{fb}^{-1}$ in integrated luminosity. The measured data is compared to the prediction from the Standard Model and interpreted in terms of a new heavy vector boson W'.

As no significant deviations from the Standard Model have been observed, exclusion limits have been set. The W' can be interpreted in the context of the Sequential Standard Model (SSM) and masses up to $4.9\,\text{TeV}$ can be excluded at a 95% confidence level. Coupling strength ratios $\frac{g_{W'}}{g_W}$ can be excluded from 0.02 for low masses up to 2 for high masses. Additionally, the decay of the W' into a W and a Z boson has been investigated and shows no sensitivity for this integrated luminosity.
A model independent cross section limit has been evaluated to $211\,\text{fb}$ for the lower transverse mass threshold of $300\,\text{GeV}$ and $0.13\,\text{fb}$ at a transverse mass threshold of $3000\,\text{GeV}$.
To investigate the influence of the expected luminosity at the end of Run II and Run III of the LHC, an extrapolation to $150\,\text{fb}^{-1}$ and $300\,\text{fb}^{-1}$ has been performed. The improvement on the exclusion limit in context of the SSM is expected to be small, thus the maximum sensitivity for this interpretation at $\sqrt{s} = 13\,\text{TeV}$ is nearly reached.

Kurzzusammenfassung

Diese Arbeit präsentiert die Suche nach neuer Physik in dem Endzustand mit einem Elektron und fehlender transversen Energie in Proton-Proton Kollisionen am LHC mit der Schwerpunktsenergie von $\sqrt{s} = 13\,\mathrm{TeV}$. Die genutzten Daten wurden vom CMS Experiment im Jahr 2016 zur Verfügung gestellt und umfassen $35.9\,\mathrm{fb}^{-1}$ an integrierter Luminosität. Die gemessenen Daten werden mit der Vorhersage durch das Standard Modell verglichen und mit Bezug auf ein neues, schweres Vektorboson W' interpretiert.

Da sich keine signifikanten Abweichungen vom Standard-Modell gezeigt haben, wurden Ausschlussgrenzen gesetzt. Das W' kann im Kontext des Sequential Standard Model (SSM) interpretiert werden und Massen bis zu $4.9\,\mathrm{TeV}$ können in einem Vertrauensbereich von 95% ausgeschlossen werden. Das Verhältnis der Kopplungsstärken $\frac{g_{W'}}{g_W}$ kann von 0.02 für kleine Massen bis zu 2 für große Massen ausgeschlossen werden. Zusätzlich wurde der Zerfall des W' in ein W und ein Z Boson untersucht und es wurde keine Sensitivität im Bereich dieser integrierten Luminosität gefunden.
Es wurde ein modelunabhängiges Limit auf den Wirkungsquerschnitt mit $211\,\mathrm{fb}$ für den niedrigen Minimalwert der transversen Masse von $300\,\mathrm{GeV}$ und $0.13\,\mathrm{fb}$ für einen Minimalwert der transversen Masse von $3000\,\mathrm{GeV}$ bestimmt.
Um den Einfluss der erwarteten Luminosität am Ende von Run II und Run III des LHCs zu untersuchen wurde eine Extrapolation zu $150\,\mathrm{fb}^{-1}$ und $300\,\mathrm{fb}^{-1}$ durchgeführt. Die erwartete Verbesserung der Ausschlussgrenzen im Kontext des SSM ist gering, daher ist die maximale Sensitivität dieser Interpretation mit $\sqrt{s} = 13\,\mathrm{TeV}$ fast erreicht.

Contents

Contents

1 Introduction

The discovery of the electron in 1897 by J.J Thomson [1] can be seen as the starting point of what we call now particle physics. The description of the blackbody spectrum by Max Planck in 1900 [2], which built the fundamentals of quantum mechanics, finally resulted in the development of the Standard Model. Particle physics has managed to give more and more insights in the possible underlying quantities and laws that make up the world as we see it around us.

Since the early days of the Large Hadron Collider at CERN, the search for a new heavy vector boson W' decaying into an electron and a neutrino has been a key analysis in the CMS collaboration [3–7]. This decay channel provides a clear signature which does not require complicated selection and can therefore provide model independent interpretation as well. As this analysis has a long history in the collaboration, the kinematic selection for this decay channel has already been optimized.

In 2016, CMS provided the biggest dataset to date with a certified integrated luminosity of $35.9\,\mathrm{fb}^{-1}$ at the center-of-mass energy of $\sqrt{s} = 13\,\mathrm{TeV}$. This high amount of statistics and the corresponding high number of simultaneous interactions at each bunch crossing gives more insights in the behavior of the detector and the reconstruction of the particles. Effects that where not visible at lower statistics, especially at the high energy regions and are challenging to understand, can be investigated.

This thesis will begin with a short introduction of the theoretical framework in Chapter 2. Chapter 3 will describe the experiment: the Compact Muon Solenoid (CMS) including its constituents and the used kinematic variables. Chapter 4 then explains the used data and simulated samples. Chapter 5 will show the general selection with the different object reconstructions and specific requirements to handle problems that appeared during the data reconstruction in 2016.

The details of the analysis of the 2016 dataset are described in Chapter 6 which will lead to the final results in Chapter 7. These results are used in Chapter 8 for a statistical interpretation of the measurement and an extrapolation to higher integrated luminosities will be presented.

2 Theoretical Background

The purpose of this section is to give an overview of the the theoretical background for this thesis. At first, a short overview over the Standard Model (SM) of particle physics is given, followed by the description of possible interpretations of the final state, which is looked into in this analysis, in terms of new physics.

This thesis uses the common unit system employed in particle physics. Variables describing energies are always given in terms of electron volt (1 eV= $1.60218 \cdot 10^{-19}$ J). The values of Planck's constant ($\hbar = 6.58212 \cdot 10^{-22}$ MeV s) and the speed of light ($c = 2.99792 \cdot 10^8$ ms) are set to 1. Therefore, properties like the mass or the momentum of a particle can be given in units of eV as well. The charge of a particle will be given in terms of the elementary charge e ($e = 1.60218 \cdot 10^{-19}$ C) [8].

2.1   Standard Model

If not stated otherwise, the content of the following section is based on "Introduction to Elementary Particles" by D. Griffiths [8].

The standard model of particle phyics is, besides Einsteins theory of general relativity [9], one of the most precisely tested theories of physics. It describes all elementary particles that we know of today and the interactions between them. It is a quantum field theory where particles can be interpreted as excited energy states of their corresponding field. The standard model as it is today consists of 61 particles. This number can be divided into two groups: fermions and bosons. Fermions are particles, that have a spin $s = \frac{1}{2}$ and are the constituents of the matter that appears in nature. Bosons have an integer spin, either $s = 0$ or 1, and are the mediators of the interactions between the particles.

The fermions can be divided into two sub-groups: leptons and quarks. The difference between these two groups is that quarks carry a color while the leptons do not. They are grouped again into three different generations according to their mass.

All leptons with their mass and charge are listed in Table 2.1.1. Additionally to these properties, each particle has a lepton number L_i ($i = e, \mu, \tau$). Each lepton has its anti-particle, a partner where all signs are reversed but leaving the mass unchanged. This leads to a final lepton count of 12. This thesis is mainly interested in the electrons and their neutrino. As these are the lightest leptons, they do not decay into other leptons and their momentum can be approximated to be equal to their energy at energies in colliders like the Large Hadron Collider (LHC).

Table 2.1.1: Generations of leptons and their properties. All values are taken from [10].

lepton	mass (MeV)	charge (e)
e	0.511	-1
ν_e	$< 2 \cdot 10^{-5}$	0
μ	105.7	-1
ν_μ	< 0.19	0
τ	1777	-1
ν_τ	< 18.2	0

The quarks can be seen in Table 2.1.2. Each quark can have one of three colors and carries an additional baryon number of 1/3 and strangeness (S), charm (C), beauty (B) and truth (T) according to the type of the quark. As the up-quark is the only one with $Q = \frac{2}{3}$ and $S = C = B = T = 0$, an additional "upness" is not needed. Similar things can be said about the down-quark. As for the leptons, anti-particles with reversed signs except the mass exist for each quark, leading to a total number of 36 quarks.

Table 2.1.2: Generations of quarks and their properties. All values are taken from [10].

quark	mass (MeV)	charge (e)	
down (d)	4.8	$-\frac{1}{3}$	
up (u)	2.3	$\frac{2}{3}$	
strange (s)	95	$-\frac{1}{3}$	$S = -1$
charm (c)	$1.28 \cdot 10^3$	$\frac{2}{3}$	$C = -1$
bottom (b)	$4.18 \cdot 10^3$	$-\frac{1}{3}$	$B = -1$
top (t)	$173.2 \cdot 10^3$	$\frac{2}{3}$	$T = -1$

As said before, the bosons are the mediators of the fundamental interactions between the particles. The photon γ, eight gluons and the Z and W$^\pm$ mediate the electromagnetic, strong and weak interaction, respectively. These are the spin 1 bosons. Whereas the photon and the gluons do not have a mass, the masses of the mediators of the weak interaction where measured to be $M_Z \approx 91.2\,\text{GeV}$ and $M_W \approx 80.4\,\text{GeV}$. Again, each boson has an anti-particle leading to 12 spin 1 bosons with the photon and the Z being their own anti-particle.

An additional massive boson with spin 0 arises from spontaneous symmetry breaking in the unification of electromagnetic and weak interaction (see Subsection 2.1.4), called Higgs-boson. This boson explains how the particles gain mass in the standard model. In 2012, a new particles with the expected properties of the Higgs-boson was

discovered [11–13].

The gravitation is not part of the standard model. At this time, there is no sufficient and tested quantum field theory of gravitation.

The standard model of particle physics is a gauge theory with local gauge invariance. Like the Lagrange-formalism of classical mechanics, the starting point is a Lagrangian, or more precisely a Lagrange density $\mathscr{L}$, with the Euler-Lagrange equation:

$$\partial_\mu \left(\frac{\partial \mathscr{L}}{\partial(\partial_\mu \phi_i)} \right) = \frac{\partial \mathscr{L}}{\partial \phi_i} (i = 1,2,3,...) \tag{2.1}$$

Here, $\mathscr{L}$ is a function of the fields ϕ_i and their derivatives. Demanding that the complete Lagrangian should be invariant under local gauge transformations leads to additional terms in the Lagrangian. These terms are the boson fields that introduce the interaction of particles into the Lagrangian.

2.1.1 Quantum Electrodynamics

As an example for local gauge invariance, one can start with the Dirac Lagrangian for a free spin-$\frac{1}{2}$ field:

$$\mathscr{L} = i\bar{\psi}\gamma^\mu \partial_\mu \psi - m\bar{\psi}\psi \tag{2.2}$$

Here, ψ is the spinor field or just spinor, γ^μ are the gamma matrices and m is the mass of the particle. One can demand the Lagrangian to be invariant under a local gauge transformation $\psi \to U\psi$, with U being a unitary matrix. In the case of electrodynamics, U is a unitary $1x1$ matrix which corresponds to the symmetry group $U(1)$. U can also be written as the exponential $U = e^{i\theta(x)}$. Applying this local gauge transformation on the Lagrangian, Equation 2.2 gives:

$$\mathscr{L} \to \mathscr{L} - \bar{\psi}\gamma^\mu \psi \left(\partial_\mu \theta \right) \tag{2.3}$$

To compensate the additional term of $\bar{\psi}\gamma^\mu \psi \left(\partial_\mu \theta \right)$, a new field A_μ is introduced:

$$\mathscr{L} = \left[i\bar{\psi}\gamma^\mu \partial_\mu \psi - m\bar{\psi}\psi \right] - \left(q\bar{\psi}\gamma^\mu \psi \right) A_\mu \tag{2.4}$$

Equation 2.3 shows, that this field needs to transform under the following rule:

$$A_\mu \to A_\mu + \partial_\mu - \frac{1}{q}\partial_\mu \theta(x). \tag{2.5}$$

With this new vector field introduced to the Lagrangian, one needs to add the term of a free field additionally to the coupling to ψ. The Proca Lagrangian describes a free massive vector field

$$\mathscr{L} = \frac{-1}{16\pi}F^{\mu\nu}F_{\mu\nu} + \frac{1}{8\pi}m_a^2 A^\nu A_\nu \tag{2.6}$$

with $F^{\mu\nu} \equiv (\partial^\mu A^\nu - \partial^\nu A^\mu)$, therefore being the electromagnetic field tensor, and m_A being the mass of the field. The term $A^\nu A_\nu$ in Equation 2.6 is not invariant under Equation 2.5, which leads to the conclusion, that $m_A = 0$ needs to hold to keep the Lagrangian invariant, therefore the field is massless.
The final Lagrangian for a spin-$\frac{1}{2}$ particle is:

$$\mathscr{L} = \underbrace{\left[i\bar\psi\gamma^\mu\partial_\mu\psi - m\bar\psi\psi\right]}_{\text{lepton propagation}} - \underbrace{\left[\frac{1}{16\pi}F^{\mu\nu}F_{\mu\nu}\right]}_{\text{photon propagation}} - \underbrace{(q\bar\psi\gamma^\mu\psi)\,A_\mu}_{\text{lepton-photon interaction}} \tag{2.7}$$

As the photon is massless, the range of the electromagnetic interaction is infinite. While all other interactions in the SM follow this scheme to formulate a Lagrangian based on the invariance under a group of transformations, the following sections will only cover their essential features.

2.1.2 Quantum Chromodynamics

Quantum chromodynamics describes the strong interaction between particles. Section 2.1 introduced quarks as fermions with a color charge: red, blue and green. This leads to three different spinors ψ_r, ψ_b and ψ_g that can be combined in a three component vector

$$\psi = \begin{pmatrix} \psi_r \\ \psi_b \\ \psi_g \end{pmatrix} \tag{2.8}$$

As in electrodynamics, one can now demand an invariance under a local gauge transformation. In addition the the U(1) group of the electrodynamic interaction, an invariance under a $SU(3)$ transformation is demanded to take the three-component vector of quantum chromodynamics into account. This leads to the introduction of eight gauge fields that correspond to the gluons. Even though that the gluons are massless, like the photons, their range is not infinite. The coupling strength of the strong interaction rises as the distance of the interacting quarks grows which leads to a constant force. This effect is called confinement. At some point, the energy in the system is high enough to create new quark-antiquark pairs. Additionally, only colorless bound states have been observed. Therefore, particles made from quarks must be a combination of a quark-antiquark pair (mesons) or they are combined of all three colors (baryons). Additional colorless combinations of single quarks are theoretical possible. In fact, in July 2015, a paper about the possible discovery of a pentaquark state (all three colors plus one color and its anti-color) was published [14].
The coupling strength behaves differently at very short distances. It decreases for an increasing momentum transfer $|Q^2|$. This effect is called asymptotic freedom and leads to the fact that, for $|Q^2| \gg 0$, quarks can approximately be seen as free particles. Therefore, they can be investigated, for example at hadron colliders.

2.1.3 Electroweak Unification

Like in QED and QCD, the weak interaction is mediated by bosons: the charged $W^\pm$ and the neutral Z. In contrast to the gluons and the photon, they both carry a mass ($M_W \approx 80.4\,\text{GeV}$, $M_Z \approx 91.2\,\text{GeV}$). The name "weak" interaction arises from the small range, due to the massive mediators, and the small coupling constant compared to the other two interactions of the SM. When looking at high energy regimes, a problem arises for the theory of weak interaction containing massive fields. It can not be renormalized which, for rising energies, results in rising cross sections. This problem was solved by unifying electromagnetic and the weak interactions.
The unification of the electromagnetic and weak interactions was proposed by Glashow, Weinberg and Salam [15–17]. The underlying symmetry corresponds to $SU(2) \otimes U(1)$ and leads to four massless fields, namely two charged fields, W^1 and W^2, and two neutral fields, W^3 and B. These single fields do not appear in nature but they actually mix to create:

$$W^\pm = \sqrt{\frac{1}{2\pi}} \left(W^1 \mp iW^2 \right)$$
$$Z = -B\sin(\Theta_W) + W^3\cos(\Theta_W)$$
$$A = B\cos(\Theta_W) + W^3\sin(\Theta_W)$$

(2.9)

Here, Θ_W corresponds to the mixing angle. It was experimentally determined to be $\sin^2(\Theta_W) = 0.2314$.
The W bosons correspond to the charged current of the weak interaction. It is the only interaction that can change the flavor of the particle, e.g. turn an electron into a neutrino, and only couples to left-handed particles which makes the coupling violating the parity maximally. The carried charge is also called weak isospin I. The Z is then representing the neutral weak current. Its "charge", so to say, is the weak hypercharge Y that is connected to the electric charge and the isospin by the Gell-Mann-Nishijima formula:

$$Q = I^3 + \frac{1}{2}Y$$

(2.10)

I^3 is the third component of the weak isospin. Instead of only coupling to left handed particles like the W boson does, the Z couples to right handed particles as well. The field A is the photon field that was already shown in Subsection 2.1.1.
While the GWS model can describe the weak and electromagnetic interactions between the particles very well, it has no explanation for the mass of the Z and W which are measured in experiments.

2.1.4 Higgs Mechanism

As the W and Z bosons are not massless, the local gauge invariance of the electroweak interaction is violated. Adding an additional field to the Lagrangian leads to a so-called "spontaneous symmetry breaking" which recovers the local gauge invariance and gives mass to the particles:

$$\mathcal{L} = \frac{1}{2} \left(\partial_\mu \psi \right)^* \left(\partial^\mu \psi \right) + \frac{1}{2} \mu^2 \left(\psi^* \psi \right) - \frac{1}{4} \lambda^2 \left(\psi^* \psi \right)^2 \tag{2.11}$$

$\psi = \psi_1 + i\psi_2$ is a single complex field and a real constant λ and a complex constant μ. Demanding that the system is invariant under local gauge transformations again leads to a new massive scalar particle, the Higgs particle, and a new massive field, the Higgs field. The coupling of the gauge bosons to the Higgs field gives masses to these particles. For $\mu > 0$, the minimum occurs at $\phi = \pm\mu/\lambda$. This asymmetry of the ground state recovers the symmetry of the electroweak Lagrangian. This solution was introduced by three different groups in 1964 [18–20] and lead to the nobel prize for Peter Higgs and François Englert in 2013 [21].
The fermions of the standard model gain their mass via the so-called Yukawa couplings to the Higgs field.

2.2 Beyond The Standard Model

Even though that the Standard Model is tested very well and describes all the particles that we know of today, there are different observations that it can not explain.
For example, the SM predicts massless neutrinos where in fact neutrino oscillations, e.g. the conversion of a muon neutrino ν_μ into a tau neutrino ν_τ, have been measured [22, 23]. This indicates, that neutrinos actually have a mass.
Another phenomenon is that the observation of the rotation curve of galaxies provides evidence for a new type of matter, so-called "dark matter", that is only visible due to its gravitational interaction [24].
Theories that go beyond the standard model often introduce new particles, e.g. supersymmetry introduces a supersymmetric partner to each of the standard model particles [25]. This analysis looks into a benchmark model introducing a new heavy partner to the Standard Model W boson. This approach using the "Sequential Standard Model" is described in the next section.

2.2.1 Sequential Standard Model

In this thesis, the decay of a new heavy vector boson W′ into an electron and a neutrino is investigated. The Sequential Standard Model (SSM)[26] provides an implementation of such a boson which, essentially, is a heavy copy of its standard model partner. This model is often used as a reference or benchmark model for

other BSM searches. The Feynman graph of this process can be seen in Figure 2.2.1 at leading order. In SSM, the coupling of the W' to fermions is assumed to be the
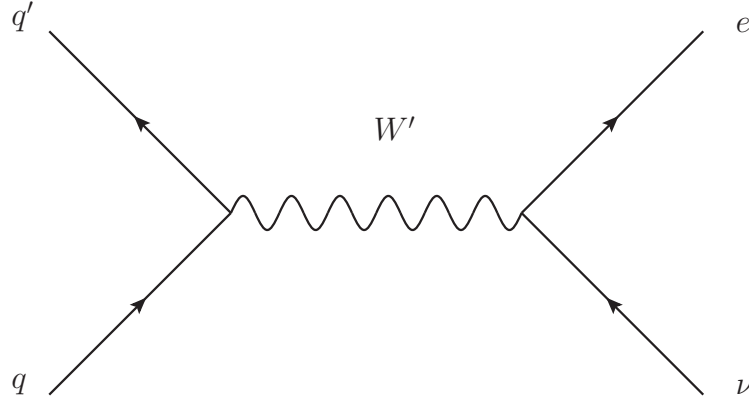

Figure 2.2.1: Feynman graph of the production and decay of a W' boson into an electron neutrino pair.

same as for the standard model W. As the mass of the new particle can be higher, the decay into a top and a bottom quark is possible. Additionally, the coupling to WZ is assumed to be zero. The decay width of the W' into a pair of fermions can be described with [27, 28]:

$$\Gamma_{W' \to \bar{f}f'} = M_{W'} \frac{g_{W'}^2 C_{\bar{f}f'}}{2 \cdot 48\pi} F(\frac{m_{\bar{f}}}{M_{W'}}, \frac{m_{f'}}{M_{W'}}) \tag{2.12}$$

$C_{\bar{f}f'}$ is the color factor, which is 1 for leptons and 3 for quarks, and $F(x_1, x_2)$ describes next-to-next-to-leading order corrections to the width. The form of the correction factor is [27, 28]:

$$F(x_1, x_2) = \left(2 - x_1^2 - x_2^2 - \left(x_1^2 - x_2^2\right)\right) \sqrt{\left(1 - (x_1 + x_2)^2\right) \cdot (1 - (x_1 - x_2)^2)} \tag{2.13}$$

Assuming that the W' mass is much higher than the fermion masses, except for the top and the bottom quark, F becomes $F(0,0) = 2$ for these fermions. This results in:

$$\Gamma_{W' \to \bar{f}f'} = M_{W'} \frac{g_{W'}^2}{2 \cdot 48\pi} (18 + 3F(\frac{M_t}{M_{W'}}, \frac{M_b}{M_{W'}})) \tag{2.14}$$

If the mass of the W' is also much higher than the mass of the top quark, the width can be expressed as:

$$\Gamma_{W'} = M_{W'} \frac{g_{W'}^2}{4 \cdot \pi} \tag{2.15}$$

Using the fact, that the coupling of the W' is set to the same value as that of the Standard Model W with $\Gamma_W = M_W \frac{3g_W^2}{16\pi}$, which follows from Equation 2.12 without

the decay into a top and a bottom quark, results in:

$$\Gamma_{W'} = \frac{4}{3}\frac{M_{W'}}{M_W}\Gamma_W \tag{2.16}$$

The branching fraction of the W′ decaying into an electron neutrino pair is about 8.5% which is smaller than the one from the SM W due to the possible top-bottom decay. The decay width for three different masses of the SSM W′ can be seen in Table 2.2.1.

Table 2.2.1: Total decay width of three different SSM W′ bosons [27].

Mass $m_{W'}$	Width Γ
1 TeV	33 GeV
5 TeV	170 GeV
6 TeV	200 GeV

As the W′ is a copy of the SM W, interference effects between these two bosons can occur. This interference can be constructive or destructive, leading to a increase or decrease of the cross section, respectively. For the cross section follows [29, 30]:

$$\frac{\sigma}{s} \propto \frac{g_W^4}{(s - M_W^2)^2 + \Gamma_W^2 M_W^2} + \frac{g_{W'}^4}{(s - M_{W'}^2)^2 + \Gamma_{W'}^2 M_{W'}^2}$$
$$\pm 2g_W^2 g_{W'}^2 \frac{s - M_W^2)(s - M_{W'}^2) + \Gamma_W \Gamma_{W'}}{((s - M_W^2)^2 + \Gamma_W^2 M_W^2)((s - M_{W'}^2)^2 + \Gamma_{W'}^2 M_{W'}^2)} \tag{2.17}$$

The first term corresponds to the SM W, the second term to the SSM W′ and the third term describes the interference between both. In the SSM, the interference is neglected.

As an extension to the pure SSM interpretation of the W′, this thesis looks into a scenario where the coupling of the new vector boson is not set to the same value as in the SM but is assumed as an free parameter. This approach impacts the width (Equation 2.15) and the cross section (Equation 2.17) of the W′.

2.2.2 Heavy Vector Triplet (Model B)

As mentioned in Subsection 2.2.1, the decay of the W′ in the SSM into bosons is forbidden. The Heavy Vector Triplet model (HVT) [31] can be used to describe the decay of a W′ into a W and a Z boson which, ultimately, can result in the same final state containing one electron and missing transverse energy as the sum of three neutrinos (see Figure 2.2.2). Additionally to the SM fields and interactions, this model
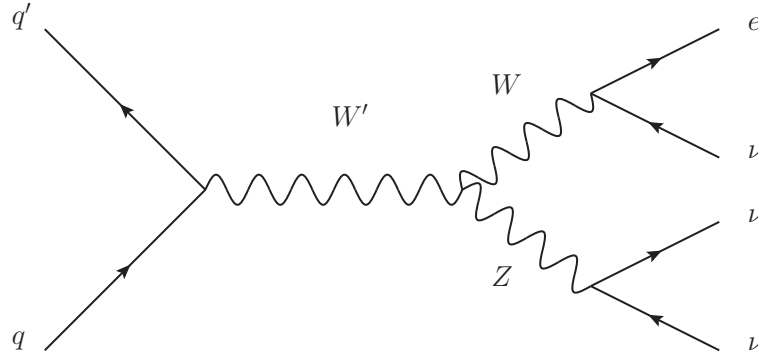
Figure 2.2.2: Feynman graph of the production and decay of a W' boson into a W and a Z boson which leads to an electron and three neutrinos in the final state.

introduces a real vector ($V_\mu^a, a = 1,2,3$), describing a charged and a neutral heavy spin-one particle:

$$V_\mu^\pm = \frac{V_\mu^1 \mp iV_\mu^2}{\sqrt{2}}, V_\mu^0 = V_\mu^3 \tag{2.18}$$

$V_\mu^\pm$ can be interpreted as a W' boson. The dynamics of this vector is described by the following Lagrangian only considering the relevant parts for the diboson decay:

$$\mathscr{L}_V = -\frac{1}{4}D_{[\mu}V_{\nu]}^a D^{[\mu}V^{\nu]a} + \frac{m_V^2}{2}V_\mu^a V^{\mu a} + ig_V c_H V_\mu^a H^\dagger \frac{\sigma^a}{2}\overset{\leftrightarrow}{D}{}^\mu H \tag{2.19}$$

The first two parts of the Lagrangian contain the kinetic and the mass term of the V. The trilinear and quadrilinear interactions with the vector bosons are described by the covariant derivatives:

$$D_{[\mu}V_{\nu]}^a = D_\mu V_\nu^a - D_\nu V_\mu^a, \quad D_\mu V_\nu^a = \partial_\mu V_\nu^a + g\epsilon^{abc}W_\mu^b V_\nu^c \tag{2.20}$$
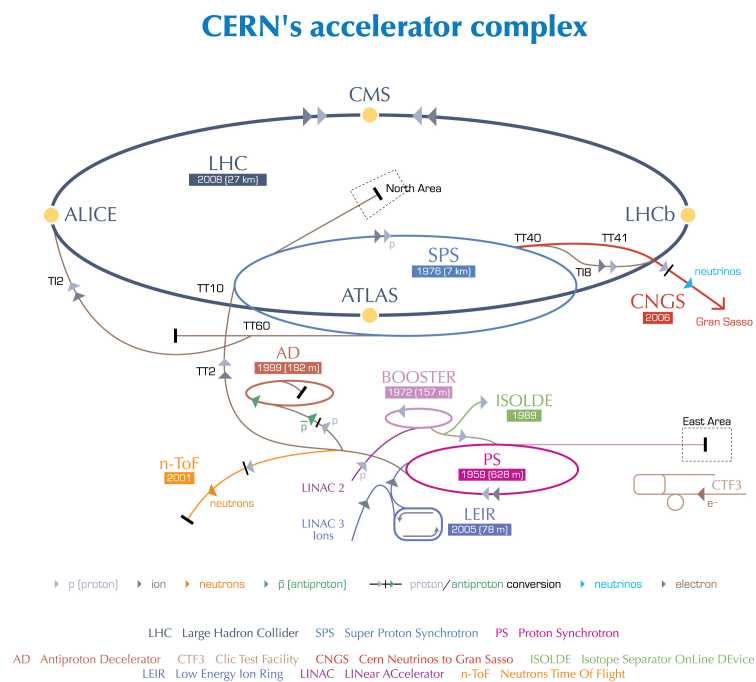
Here, g is the $SU(2)_L$ gauge coupling. The interactions of the vector with the Higgs current is described by the last part of the Lagrangian:

$$iH^\dagger \frac{\sigma^a}{2}\overset{\leftrightarrow}{D}{}^\mu H = iH^\dagger \frac{\sigma^a}{2}D^\mu H - iD^\mu H^\dagger \frac{\sigma^a}{2}H \tag{2.21}$$

This Higgs current term introduces a coupling of the new vector bosons to the physical Higgs field an three unphysical Goldstone bosons. These Goldstone bosons represent the SM vector bosons in the high energy regime [32]. Therefore, the parameter c_H controls the interaction of the V with the SM bosons W and Z resulting in a possible bosonic decay channel. The branching ratio of a decay of the W into an electron plus a neutrino and of the Z into neutrinos is 2.15% [10]. This small branching ratio leads to problems concerning the sensitivity of this final state for the search for a diboson resonance.

3 Experiment

3.1 The Large Hadron Collider

Figure 3.1.1: A schematic view of the accelerator complex at CERN showing the different accelerators and experiments [33].

In 1994, CERN [34], the European Organization for Nuclear Research, approved the plans to build a new proton-proton collider, the Large Hadron Collider (LHC) [35], inside the old tunnel of the Large Electron-Positron Collier (LEP) [36]. The tunnel lies up to 170 m below the surface near Geneva with a circumference of 26.7 km. The LHC is designed to provide proton-proton collisions with a center-of-mass energy up to 14 TeV. It is also used to produce lead ion collisions with an energy up to 2.8 TeV per nucleon. The design luminosity is $10^{34} \text{cm}^{-2}\text{s}^{-1}$ for proton-proton and $10^{27} \text{cm}^{-2}\text{s}^{-1}$

for heavy ion collisions. The luminosity can be calculated with [37]:

$$L = \frac{N_1 N_2 f N_b}{4\pi\sigma_x\sigma_y} \tag{3.1}$$

Here, N_b is the number of bunches, packages of particles, that are collided, $N_{1,2}$ is the number of protons in each bunch, f the revolution frequency and $\sigma_{x,y}$ describes the transverse size of the bunches. Often, additional correction factors are added to take care of effects like specific crossing angles or Non-Gaussian beam profiles. Integrating the luminosity over time leads to the integrated luminosity:

$$L_{int} = \int L \, dt \tag{3.2}$$

On 10 September 2008, the first beam was injected into the LHC [38].
The protons are obtained from a hydrogen bottle. The hydrogen atoms are stripped from their electrons by strong electric fields. They are first accelerated in a linear accelerator (LINAC 2) and the Booster, arriving at the Proton Synchrotron (PS) with an energy of approximately 1.4 GeV. In the PS and the following Super Proton Synchrotron (SPS), the protons are accelerated to about 450 GeV and are finally injected into the LHC [39].
Figure 3.1.1 shows a sketch of the accelerator complex at CERN with the described pre-accelerators and four of eight interaction points along the LHC ring. At each of these points, experiments are placed to measure the scattering products of deep inelastic collisions. The "A Large Ion Collider Experiment" (ALICE) [40] is designed to analyze the collision of heavy ions. The research at the "Large Hadron Collider beauty" (LHCb) [41] is specialized on the decay of B hadrons and CP violation.
The "A Toroidal LHC Apparatus" (ATLAS) [42] and the "Compact Muon Solenoid" (CMS) [43] are general-purpose detectors, designed for a wide range of physical measurements at high energies.
As this thesis uses data taken with the CMS detector, the following section will describe this experiment.

3.2   The CMS Experiment

This section is mostly based on [43]. The Compact Muon Solenoid (CMS) is located approximately 100 m under Cessy, a French village close to Lake Geneva.
The purpose of the CMS is to provide good muon reconstruction with a good momentum and dimuon mass resolution over a large range of angles and momenta. Besides muons, it is also built to reconstruct any charged particles with a good momentum resolution and efficiency and gives the possibility of τ and b-jet tagging. Additionally, a precise measurement of the electromagnetic energy deposition and the diphoton and dielectron mass is provided together with an efficient photon and lepton isolation up to high luminosities. A high quality of the measurement of jets

and missing-transverse-energy is provided as well. The LHC delivers a crossing of proton bunches at a rate of 25 ns. These bunches contain protons of the order of 10^{11}. This leads to multiple interactions at each bunch crossing, the so-called "pile-up". Therefore, a good vertex reconstruction is needed. Figure 3.2.1 shows a transverse slice through the detector. The concept of the CMS can be compared to an onion, with different detector parts built around the interaction point in the middle. A possible path of a muon starting at the interaction point passing through the outer shells is visualized by a red arrow.
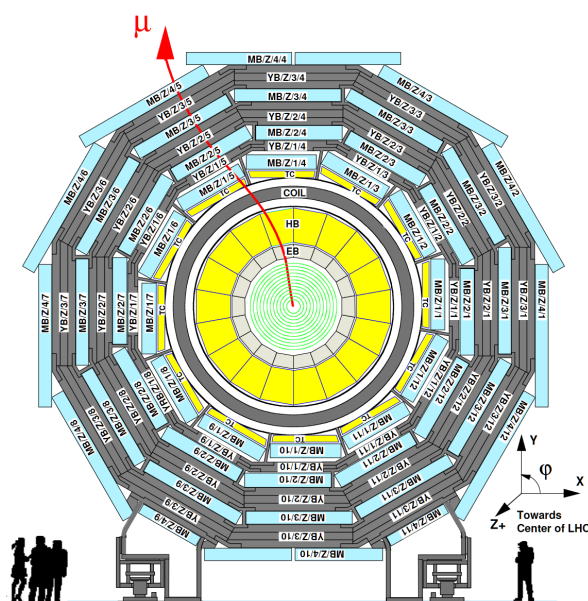

Figure 3.2.1: Sketch of the CMS detector in the transversal plane. The interaction is located in the middle with the detector components built around it. The directions of the coordinate axes are shown in the lower right corner. Taken from [43].

CMS uses a coordinate system with its origin in the center of the interaction point. The x-axis points to the middle of the LHC ring and the y-axis points upwards to the surface. The z-axis is aligned to the beam direction. The azimuthal angle ϕ is defined as the angle from the x-axis in the x-y-plane and the polar angle Θ is measured from the z-axis. The radial coordinate r is defined in the x-y-plane. With the angle Θ, one can define the pseudorapidity:

$$\eta = -\ln\left[\tan\left(\frac{\Theta}{2}\right)\right] \tag{3.3}$$

A difference in the pseudorapidity is invariant under Lorentz boosts.

One can define the spatial distance between two particles using the pseudorapidity and the angle ϕ:

$$\Delta R = \sqrt{(\Delta\eta)^2 + (\Delta\phi)^2} \qquad (3.4)$$

If the particle mass is significantly smaller than its energy, the spatial distance is invariant under a Lorentz boost. As the energy of the interacting partons is not know but their initial transverse momentum can be approximated to be zero, the values in the transverse plane (x-y-plane) p_T and E_T are often used. p_T is defined by $p_T = p_x^2 + p_y^2$.

Additionally, one can define the transverse mass M_T of two particles with negligible mass. The quantity M_T will be the main discriminant variable of this analysis as the two-body decay of the signal, that is looked for, leads to a well distinguishable Jacobian peak in this spectrum of M_T of the electron and the neutrino, which can not be measured by the detector but shows up as so-called "missing transverse energy", E_T^{miss}, in the event. The M_T of these two particles is defined by $M_T = \sqrt{2p_T^e E_T^{miss} \left(1 - \cos\left[\Delta\phi(e, E_T^{miss})\right]\right)}$.

The individual detector parts will be described in the following.

3.2.1 Tracker

The first part of the detector around the interaction point is the tracker system. Its purpose is the reconstruction of the trajectory of the measured particles and can be seen as a sketch in Figure 3.2.2. As mentioned, due to the pile-up, a good vertex reconstruction is needed. For this purpose, closest to the interaction point, is the silicon pixel detector with three layers in the barrel and two discs per endcap. It covers the pseudorapidity range of -2.5< η <2.5 and provides a spatial resolution of 15-25 μm.
Following the pixel detector, a silicon strip tracker system is built. It consists of the Tracker Inner Barrel (TIB), the Tracker Inner Disks (TID), the Tracker Outer Barrel (TOB) and the Tracker Endcaps (TEC+/-).
The inner system delivers up to 4 trajectory measurements and it is surrounded by the outer barrel system which additionally provides 6 measurements. The endcap system composed of 9 discs can provide 9 ϕ measurement points of a trajectory. Using a single muon with a high p_T of about 100 GeV as an example, the tracker system reaches a transverse momentum resolution of 1-2% in the η range around 1.6.
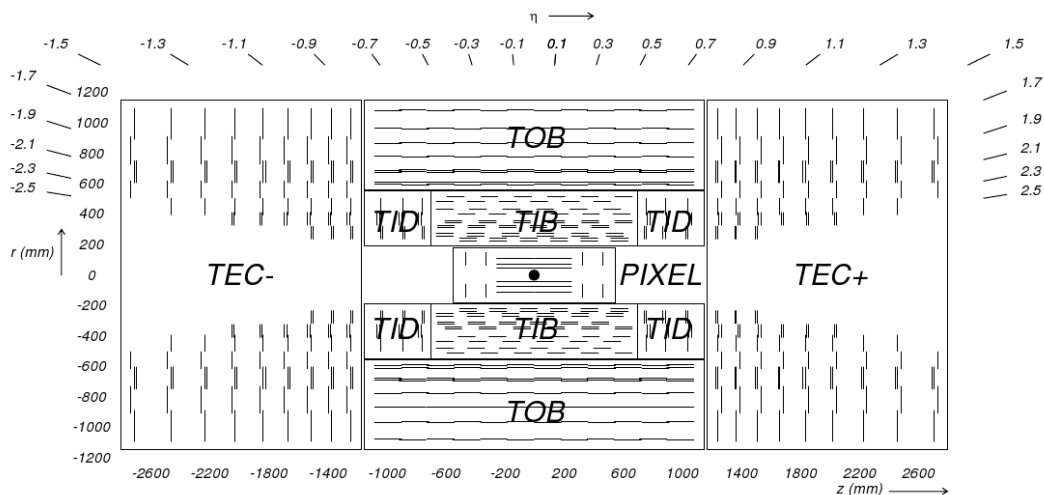

Figure 3.2.2: The tracking system surrounding the interaction point of the CMS detector in a schematic sketch. Taken from [43].

3.2.2 Calorimeters

Electromagnetic Calorimeter

Surrounding the tracker system follows the electromagnetic calorimeter (ECAL). It consists of 68500 lead-tungstate crystals that are placed in the barrel and endcap region. The usage of lead-tungstate provides the possibility of a compact detector system due to its high density, a radiation length of 0.89 cm and a small Moliére radius.
Most of the crystals (61200) are located in the barrel region of the ECAL, covering a pseudorapidity range of $|\eta| < 1.479$. The endcaps cover a pseudorapidity range of $1.479 < |\eta| < 3.0$ and consist of about 7300 crystals divided into two halves and grouped into a crystal array containing 5x5 groups of crystals, called supercrystals. Due to the fact that the number of scintillation photons and the amplification is dependent on the temperature, the system is cooled with 18°C warm water to keep the ECAL temperature stable within a window of 0.05°C.
The energy resolution delivered by the ECAL was measured to be:

$$\left(\frac{\sigma_E}{E}\right)^2 = \left(\frac{2.8\%}{\sqrt{E/\text{GeV}}}\right)^2 + \left(\frac{12\%}{E/\text{GeV}}\right)^2 + (0.30\%)^2 \tag{3.5}$$

It is dependent on the deposited energy E in the ECAL. In Equation 3.5, the first term $(\frac{2.8\%}{\sqrt{E/\text{GeV}}})^2$ describes the stochastic effect originating from different effects, e.g. event-to-event fluctuations. The second term $(\frac{12\%}{E/\text{GeV}})^2$ takes the noise of the electronics, the digitization and the pile-up into account. The last term in the energy resolution covers mostly the leakage of energy from the crystals, differences in the light collection and errors in the calibration.

Hadron Calorimeter

The hadron calorimeter (HCAL) is built to measure hadronic particles which appear in many final states. Thus, it is important for good jet energy resolution. Additionally, it is important for the measurement of the missing transverse energy due to rarely interacting particles like neutrinos or new exotic particles. It is located after the ECAL and also has a barrel and an endcap region. Figure 3.2.3 shows a sketch of the detector components, specifically the tracker system and ECAL in the left bottom corner, followed by the HCAL and the muon system. The barrel (HB) covers the pseudorapidity range of $|\eta| < 1.3$ whereas the endcap (HE) covers an additional range of $1.3 < |\eta| < 3$. It is built from flat brass absorber plates and plastic scintillators as active medium. The light of the scintillators is then collected by wavelength shifting fibers.
Due to the fact that the stopping power of the EB and HB are not sufficient enough for hadron showers in the central region, an additional HCAL part outside of the
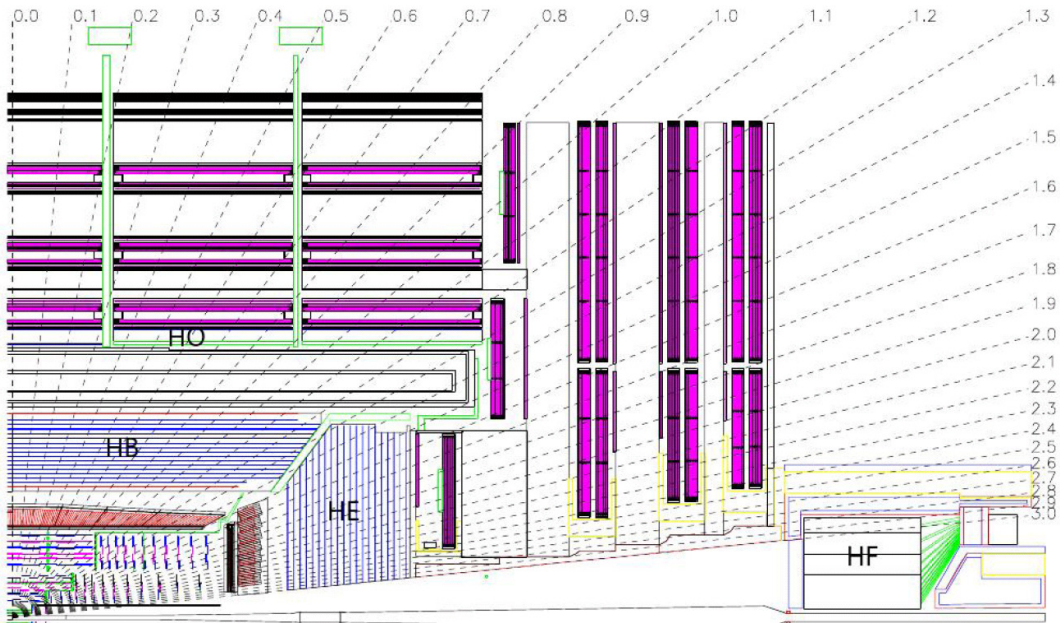
Figure 3.2.3: A longitudinal sketch showing the HCAL of the CMS detector. In the left bottom corner the tracker and the ECAL can be seen as well. Outside of the HCAL, the muon system of the CMS is visible (Taken from [43])

solenoid was built (HO), also referred to as "tail catcher". This additional HO layers increase the total depth to a minimum 11.8 hadronic interaction lengths (λ_l).

To extend the covered pseudorapidity range up to $|\eta| = 5.2$, forward hadron calorimeters (HF) are installed 11.2 m away from the interaction point. Due to the high amount of radiation and charged hadron rates, a design fitting these conditions was developed. It uses quartz fibers as the active medium to detect Cherenkov light from the incoming showers.

The energy resolution of the combination of ECAL and HCAL measured from test beam studies can be parametrized by [44]:

$$\left(\frac{\sigma_E}{E}\right)^2 = \left(\frac{100\%}{\sqrt{E/\text{GeV}}}\right)^2 + (4.5\%)^2 \tag{3.6}$$

3.2.3 Solenoid

For a precise measurement of the p_T of charged particles a strong magnetic field is needed especially at high momenta. The CMS detector contains a superconducting solenoid that provides a magnetic field of 3.8 T. The field lines are parallel to the beam and therefore bend the trajectory of the particle in the transverse plane. It surrounds the three inner detector parts, namely the tracker, ECAL and HCAL except the HO. The magnet flux from the solenoid is returned by a thick iron yoke which is the heaviest part of the detector.[45]

3.2.4 Muon System

The last and most outer part of the CMS detector is the muon system. As explained before, the measurement of the probabilities of muons was a central point in the design and found its way into the name of the detector. As the calorimeters, it is divided into a barrel and an endcap region. The barrel drift tube (DT) chambers are built into the return iron yoke and cover a pseudorapidity region of $|\eta| < 1.2$. They are again divided into 4 stations. The first 3 stations contain 8 chambers where 4 of these chambers measure the muon in the r-ϕ-plane and 4 measure in the z direction. The last stations does not contain a z direction measurement.

In the endcap region, cathode strip chambers (CSC) are used due to the high muon rate and the strong and non-uniform magnetic field. They cover a pseudorapidity range of $0.9 < |\eta| < 2.4$.

The overall reconstruction efficiency lies in between 90-95%. In transition regions of the barrel and endcaps, the efficiency drops slightly. For small η and p, the muon momentum resolution is about 9%, for high energetic muons with a momentum of around 1 TeV, the resolution can go up to about 40%, depending on η. The combination of the tracker measurement and the muon system improves the momentum resolution in the high energy region up to about 5% for a muon at the TeV-scale [46].

3.2.5 Trigger

Due to the bunch crossing of 25 ns, which corresponds to a frequency of 40 MHz, and multiple events accruing at each of these crossings, the amount of data provided from the detector systems is too large to be stored unfiltered. A trigger system has been developed to reduce the rate of events to be stored by at least a factor of 10^6. It is divided into a Level-1 (L1) hardware trigger system and High-Level Trigger (HLT), which uses software computations comparable to the offline calculations done by a specific analysis. The L1 trigger takes the information from the calorimeters as well as from the muon system. Its architecture can be seen in Figure 3.2.4. The single components deliver information about the energy and the quality of the measured object to the L1 Global Trigger that finally accepts or rejects an event based on these data. If the event is accepted by the L1, it is forwarded to the HLT. It unpacks the raw data of the event, performs reconstruction of physical objects and applies quality criteria, depending on the specific trigger path. If these criteria are fulfilled, the event is flagged as triggered in this path (e.g. SingleElectron). The HLT paths used in this analysis are described in Section 5.4.

The maximum rate of events sent to the HLT coming from the L1 is 100 kHz. The finale average HLT rate for offline event storage is 400 Hz [47].
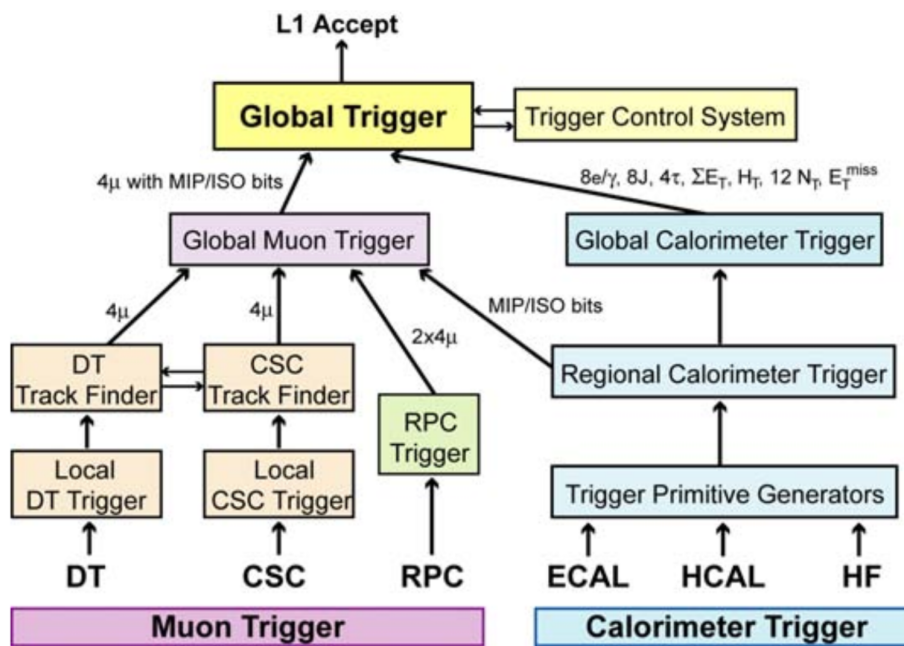
Figure 3.2.4: Architecture of the Level-1 trigger with each component of the muon system and calorimeters. Taken from [43].

4 Samples

4.1 Dataset

This analysis uses the full 2016 dataset provided by CMS containing certified runs only [48] which leads to an integrated luminosity of $35.9\,\mathrm{fb}^{-1}$. Due to the trigger strategy which will be explained in Section 5.4, the single electron as well as the single photon datasets from run B to H are used in their latest version of reconstruction. The specific run informations can be found in Table 4.1.1.

Table 4.1.1: Data taking periods in 2016 with the corresponding run periods, golden run ranges, integrated luminosity and data-set names.

Run	Run Range	Integrated Luminosity	Name of Data Set
Run B	273158-275376	$5.79\,\mathrm{fb}^{-1}$	Run2016B-23Sep2016-v3
Run C	275657-276283	$2.57\,\mathrm{fb}^{-1}$	Run2016C-23Sep2016-v1
Run D	276315-276811	$4.25\,\mathrm{fb}^{-1}$	Run2016D-23Sep2016-v1
Run E	276831-277420	$4.01\,\mathrm{fb}^{-1}$	Run2016E-23Sep2016-v1
Run F	277981-278808	$3.10\,\mathrm{fb}^{-1}$	Run2016F-23Sep2016-v1
Run G	278820-280385	$7.54\,\mathrm{fb}^{-1}$	Run2016G-23Sep2016-v1
Run H	281613-283685	$8.61\,\mathrm{fb}^{-1}$	Run2016H-PromptReco-v2,3

The corresponding dataset paths are:

- */SingleElectron/Run2016X-03Feb2017_Y/MINIAOD*

- */SinglePhoton/Run2016X-03Feb2017_Y/MINIAOD*

where X and Y denote the run and the version number.

4.2 Monte Carlo Prediction

To differentiate between a measurement of possible new physics and Standard Model processes and to describe the expected measurement of new physics, Monte

Carlo simulation is used. These simulations are produced using different Monte Carlo generators. For the purpose of making them adaptable to different integrated luminosities and high amount of statistics, which reduces the statistical uncertainty, the generated samples are normalized to an integrated luminosity of $1\,\text{pb}^{-1}$ and a cross section of $1\,\text{pb}$. Therefore, additional reweighting needs to be done to get the correct description for the used luminosity and cross section. This is done by applying the following weight factor on each event:

$$w = \frac{\sigma \cdot L}{N_{MC}} \tag{4.1}$$

Here, σ is the cross section of the specific sample, L is the integrated luminosity and N_{MC} is the total number of generated events in the sample. For some samples, an additional cross section correction factor, often called "k-factor", is available. The factor takes higher order corrections on the production cross section into account. This can either be a flat value applied on all events or dependent on a specific property, e.g. the mass of the produced W (see Subsection 4.2.2).
Some simulated samples are binned in the variable "transverse hadronic energy" or H_T. H_T is the sum of the transverse momentum of all non-leptonic particles on generator level.

4.2.1 Background Samples

The Monte Carlo samples used to describe the expected standard model background are listed below:

- Off-shell high mass W: The off-shell production of the SM $W \to l\nu$ with $l = e, \mu, \tau$ is the leading background of this analysis and hardly to reduce. This background is produced as mass-binned samples with M(W)>100 GeV up to 6000 GeV. The used generator is Pythia 8.2 [49] with the CUETP8M1 tune [50]. These samples are produced at leading order (LO). An additional W mass dependent k-factor (Subsection 4.2.2) is applied.

- W + jets $\to l\nu$: W + jets $\to l\nu$ samples are used for M(W)<100 GeV. If the H_T of is greater than 100 GeV, binned samples with H_T =100 GeV up to ∞ are used. For $H_T < 100\,\text{GeV}$ and M(W)<100 GeV the bulk sample is used. These samples are generated in MadGraph5 [51] with MLM merging [52]. Before applying a W mass dependent correction, a flat k-factor of 1.21 on the LO cross section is applied.

- $t\bar{t}$, single t: The next, subleading background processes arise from the decay of top quarks, either from $t\bar{t}$ or single top production. These processes are generated with PowHeg [53–58] except for the s-channel of the single top which is generated with MadGraph5_aMCatNLO [59].

- QCD: QCD multijet processes have the highest cross section at the LHC. These jets can create so called "fake electrons" where a jet passes all quality criteria for an electron. These samples are generated in Pythia 8.2 [49].

- Drell-Yan: The decay of the Z boson or a photon into two leptons can appear as e+E_T^{miss} if one lepton is not identified or out of acceptance and is added to the E_T^{miss} calculation. Similar to the description of the W background, mass-binned samples in the range of 10-50 GeV and 100 GeV to ∞ are produced in MadGraph5_aMCatNLO [59] with FxFx merging [60]. This leads to a cross section at NLO. Additionally, to describe the mass range of 50 GeV to 100 GeV, H_T-binned samples in the range of 100 GeV up to ∞ are used from MadGraph5 [51] with MLM merging [52] at LO. Additionally, a flat k-factor of 1.23 is applied on the H_T-binned samples.

- WW, ZZ, WZ: Diboson processes can lead to a e+E_T^{miss} final state if the bosons decay into two leptons and jets or, for the Z boson, into two neutrinos. WZ and ZZ events are generated with Pythia 8.2 [49] and WW events are generated with PowHeg [53–58].

Table 10.1.2 in the appendix (Section 10.1) shows the generator and the order of cross sections for the different background samples used.

4.2.2 W k-factor

The main background is the off-shell production of W→ *ev*. It is generated in Pythia 8.2 [49] which provides a leading order accuracy. To gain the needed precision of the description, especially at high M_T, the simulation is corrected with a factor that combines electroweak and QCD calculations at higher order following [61]. This k factor depends on the invariant mass M_{inv}:

$$k(M_{inv}) = \frac{\sigma_{(N)NLO}(M_{inv})}{\sigma_{LO}(M_{inv})} \tag{4.2}$$

$\sigma_{(N)NLO}(M_{inv})$ describes the corrected cross section. There are two approaches to combine the NLO electroweak and the NNLO QCD corrections. One can assume a additive nature of the corrections or a factorized approach where the EW corrections are assumed to be the same for all QCD orders:

$$\left[\frac{d\sigma}{dM_{inv}}\right]_{QCD \oplus EW} = \left[\frac{d\sigma}{dM_{inv}}\right]_{QCD} + \left[\frac{d\sigma}{dM_{inv}}\right]_{EW} - \left[\frac{d\sigma}{dM_{inv}}\right]_{LO} \tag{4.3}$$

$$\left[\frac{d\sigma}{dM_{inv}}\right]_{QCD \otimes EW} = \left(\frac{\left[\frac{d\sigma}{dM_{inv}}\right]_{QCD}}{\left[\frac{d\sigma}{dM_{inv}}\right]_{LO}}\right) \times \left[\frac{d\sigma}{dM_{inv}}\right]_{EW} \tag{4.4}$$

27

For the NLO calculations MCSANC [62] and for the NNLO calculation FEWZ [63] is used. Following the recommendation of the LHC working group for Run II [64], this analysis uses the additive approach (Equation 4.3). The difference to the factorized approach is used to estimate the uncertainty on this k- factor.

4.2.3 Signal

To search for new physics in the analyzed data, signal samples of the SSM W' decay (see Subsection 2.2.1) have been produced in Pythia 8.2 [49] at leading order accuracy. To account for higher order corrections (NNLO) from QCD, a mass dependent k factor is calculated using FEWZ [63, 65]. The leading order cross sections and the corresponding correction factors can be seen in Table 10.1.1 in the appendix.

In the left plot of Figure 4.2.1, one can see examples of the shape of the discriminating variable M_T for three different mass points (1.8 TeV, 3.8 TeV and 5.8 TeV) with the Jacobian peak visible at the corresponding W' mass.

The sharpness of the peak decreases for higher masses and the importance of the off-shell production becomes visible at the lower part of the M_T spectrum for the highest mass sample. As explained in Subsection 2.2.1, one can set the ratio of the coupling strength $\frac{g_{W'}}{g_W}$ as a free parameter which affects not only the cross section but the width of the Jacobian peak as well (see Subsection 2.2.1). To investigate the coupling strength, samples with varying $g_{W'}$ have been produced by the authors of [66] at leading order in Madgraph 5 [51]. The ratio of the samples with varying coupling strength to the one with $\frac{g_{W'}}{g_W}$ at generator level is used to reweight the reconstructed shape of the produced W' samples from Pythia, leading to samples with varying coupling strength and sufficient statistics. Figure 4.2.1 (right) shows an example of the reweighted shape for the 2 TeV W' signal sample. For coupling ratios with $\frac{g_{W'}}{g_W} < 1$, the peak gets narrower whereas for $\frac{g_{W'}}{g_W} > 1$ the peak broadens.

Additionally to the SSM, signals using the Heavy Vector Triplets interpretation (Subsection 2.2.2) have been produced by Youngdo Oh with Madgraph 5 [51]. They are simulated in a mass range from 1 TeV up to 2.25 TeV in steps of 250 GeV and an additional 3 TeV mass point at leading order accuracy. Three signal examples for 1 TeV, 2 TeV and 3 TeV at generator level can be seen in Figure 4.2.2. The shape does not show a clear Jacobian peak but a broad curve with a falling tail at the W' mass value. This is due to the fact that it is not a two-body decay of a W' as in the SSM but two boosted bosons decaying into two particles each. The final state contains not one electron and one neutrino but three neutrinos with two in opposite direction. This smears out the Jacobian peak resulting in the broad curve. The production cross section at LO for each mass point can be found in the appendix (Table 10.1.3).
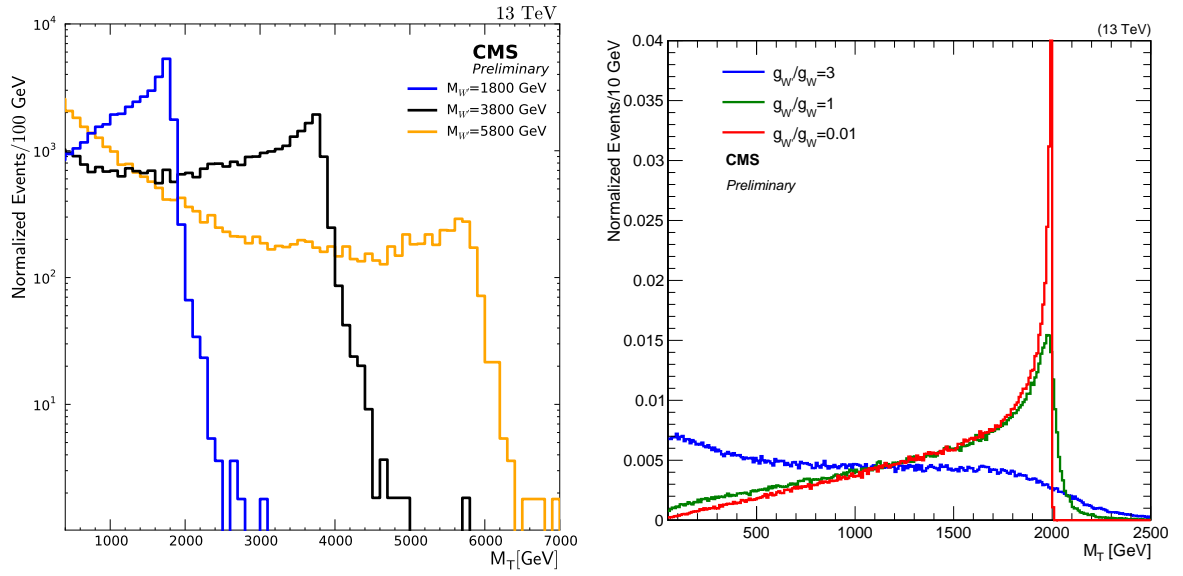
Figure 4.2.1: M_T distribution of the SSM W' for three different masses 1.8 TeV, 3.8 TeV and 5.8 TeV (left) and three different coupling ratios 0.01, 1 and 3 (right) for a mass of 2 TeV. The shape shows a Jacobian peak at the mass of the W' and the off-shell production increases with $M_{W'}$ at the low M_T regime. The Jacobian peak becomes narrower for lower couplings and broader for higher couplings. The events are normalized to a cross section of 1 pb.
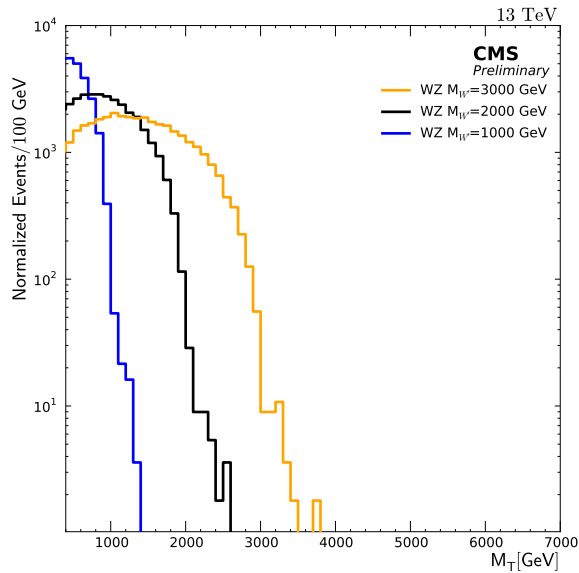

Figure 4.2.2: The M_T distribution of the signal points of 1 TeV, 2 TeV and 3 TeV for the decay into WZ is shown. The shape differs to the one in the SSM as it shows no Jacobian peak but a broad curvature. The events are normalized to a cross section of 1 pb.

29

5 General Selection

This chapter describes the basic criteria and selection to secure a needed quality and precision in the properties of the physical objects that are looked for in this analysis. At first, the reconstruction of the particles is explained followed by the identification and the trigger strategy.

5.1 Object Reconstruction

5.1.1 Particle Flow Algorithm

The particle flow algorithm (PF) [67] is an efficient way to provide a consistent reconstruction of objects in the CMS detector. The PF uses information from the track measurement in the tracker, the energy deposition in the calorimeters and the hits in the muon chambers to reconstruct electrons, muons, photons as well as neutral and charged hadrons. These results are also used to calculate the missing transverse energy. Due to the high energy of the electrons in this analysis and the resulting Bremsstrahlung, only using the particle flow algorithm is not sufficient to reconstruct electrons in the needed quality. Therefore a different approach for the electron reconstruction is used additionally to the PF.

5.1.2 Electron

The first object in the two body final state of the W′ decay is the electron. The reconstruction contains mostly two parts of the detector [68]. The track measured in the silicon detector and the deposition of energy in the ECAL are combined to reconstruct the physical properties of the particle.
As described in Subsubsection 3.2.2, the ECAL contains several crystals. The energy deposition of the electron usually activates more than one of these crystals, as the spread depends on the amount of the energy lost by Bremsstrahlung. Due to the bending of the electron path in the magnetic field the energy of the radiated photons is mainly distributed in the ϕ direction. For the clustering of the crystals, also called superclusters (SC), different approaches for the barrel and the endcap region are used to ensure that the energy deposition is coming from the electron candidate.

To create the final global SC in the barrel, the crystal with the highest energy deposit above a threshold is chosen as the starting point. Around this seed crystal, arrays of crystals with an energy deposition above a minimum value E_{array}^{min} are grouped together. Groups that contain at least one seed array with an energy above a threshold $E_{seed-array}^{min}$ are then taken into account for the SC creation.

Due to a different geometry in the endcaps, the crystals with the local maximum energy deposition compared to their four direct neighbors are the seed for the SC calculation. The transverse energy deposition in this seed needs to be above a threshold $E_{T,EEseed}^{min}$. After finding these seed crystals, surrounding clusters of 5x5 crystals are collected, ordered in E_T. If the total E_T of these clusters is above $E_{T,cluster}^{min}$ and within a range of $\pm\eta^{range}$ and $\pm\phi^{range}$, they are grouped into an SC.

Additionally, so called PF clusters are reconstructed as a part of the PF algorithm. In contrast to the SC method, all crystals around a seed with an energy deposition greater than two standard deviations above the noise are combined.

After constructing the SC, two different seeding processes can be used to find the corresponding first hits in the tracker system. At first, the ECAL driven method uses the position and energy information from the SC to estimate the electron trajectory in the first tracker layers. Additionally, pairs or triplets of tracker hits are combined with the vertices to create a tracker seed. Those are then compared to the estimation from the SC to find the matching tracker seed.

The second method is the Tracker-based seeding. It is part of the PF algorithm and starts with the Kalman filter (KF) track reconstruction, that is accurate for all charged particles if bremsstrahlung is negligible. The track is then matched to the closest PF cluster. If bremsstahlung becomes significant, the KF algorithm fails, resulting in a small number of hits in the tracker. The Gaussian sum filter (GSF)[69] is then used to refit the track. It takes radiation of bremsstrahling into account by approximating the energy loss by Gaussian mixtures using the Bethe-Heitler model [70].

The two methods are then combined to create the final electron seeds for the track reconstruction which starts with the building of the electron track by collecting the matching tracker hits to the seeds using the KF algorithm. The GSF is then used to fit the track parameters after all hits are collected. Finally, the reconstructed track is connected to the corresponding ECAL cluster. For ECAL seeded electrons this is done by finding the SC that led to the tracker seed. On the other hand, tracker seeded electrons are associated to the closest PF cluster.

The electron reconstruction can behave differently in the simulation and the measured data. To address this, one can derive so called scale factors by comparing Monte Carlo and data which are then applied to the simulation. For the reconstruction, scale factors are provided by the e/gamma POG [71].

5.1.3 Missing Transverse Energy

The second object in the final state is the electron neutrino. Due to its small interaction probability, the neutrino mostly leaves the CMS undetected. As the initial transverse momentum of the proton-proton collision, in a good approximation, is zero, the missing particle leads to a negative contribution in the vectorial sum of transverse momentum of all reconstructed particles due to the conservation of momentum, called "missing transverse energy" (MET,E_T^{miss}):

$$\vec{E}_T^{miss} = -\sum \vec{p}_T \tag{5.1}$$

For the reconstruction of the E_T^{miss}, the particle flow algorithm is used. This analysis uses so called "Type-I" corrected E_T^{miss} [72]. This correction propagates the correction of the jet energy (JEC)[73] into the calculation of the E_T^{miss}. It divides the uncorrected (raw) vectorial sum of the p_T into unclustered (uncl) and clustered (jets) particles:

$$\vec{E}_{T,raw}^{miss} = -\sum_{i\in jets} \vec{p}_{Ti} - \sum_{i\in uncl} \vec{p}_{Ti} \tag{5.2}$$

The difference between the uncorrected and corrected jet energy leads to the correction vector:

$$\vec{C}_T^{Type-I} = \sum_{i\in jets} \vec{p}_{Ti} - \sum_{i\in jets} \vec{p}_{Ti}^{JEC} \tag{5.3}$$

Therefore, the final corrected (corr) E_T^{miss} is:

$$\vec{E}_{T,corr}^{miss} = \vec{E}_{T,raw}^{miss} + \vec{C}_T^{Type-I} = \vec{E}_{T,raw}^{miss} + \sum_{i\in jets} \vec{p}_{Ti} - \sum_{i\in jets} \vec{p}_{Ti}^{JEC} \tag{5.4}$$

5.1.4 Gain Switch Problem

In December 2016, a problem with the "multi-fit" algorithm [74] to reconstruct the electron energy was discovered[75, 76]. To ensure the ideal distribution of the measured energy to the channels of the read-out electronics, the gain needs to be adjusted according to the amout of the deposited energy. A non-linearity at the end of the gain range of the ECAL barrel electronics leads to a distorted shape if the gain was switched during a pulse. This leads to a reduced reconstructed energy. This problem was fixed by switching to a weights method that has already been used in Run I of the LHC [77]. As this non-linearity has only been seen in the barrel, electrons measured in the endcaps are not effected by this "gain switch" problem.

5.1.5 Mismatch of Electron Tracks

An issue with the extrapolation of the track to the vertex was found in August 2017 [78]. The extrapolation of the vertex is used for the calculation of the position in η and ϕ of the electron as well as it provides the momentum to the tracker to combine the information with the ECAL energy measurement. A failure in this extrapolation can leads to a mismatch between the track reconstructed by the particle flow algorithm and the one using the GSF. This leads to electrons that appear in the barrel region even though they are measured in one of the endcaps. These miscalculated values for η and ϕ result in an overestimation of the p_T and E_T of the electron.

The information of one event with such a mismatch can be seen in Table 5.1.1 compared to an earlier reconstruction run where this specific event did not show the described problem. Additional to the table, the event display showing the reconstructed tracks and energy deposits of the electron in the CMS detector can be seen(Figure 5.1.1). The figure shows the difference in the matching between the ECAL energy deposition (red cone) used by the particle flow and the reconstructed electron vertex from GSF.

Table 5.1.1: Comparison of two different reconstructions of the same event. A problem with the track in the latest reconstruction (left) leads to a miscalculation of the particle flow angles (PF η(e) and PF ϕ(e)) which propagates to the p_T of the electron and the E_T^{miss} of the event.

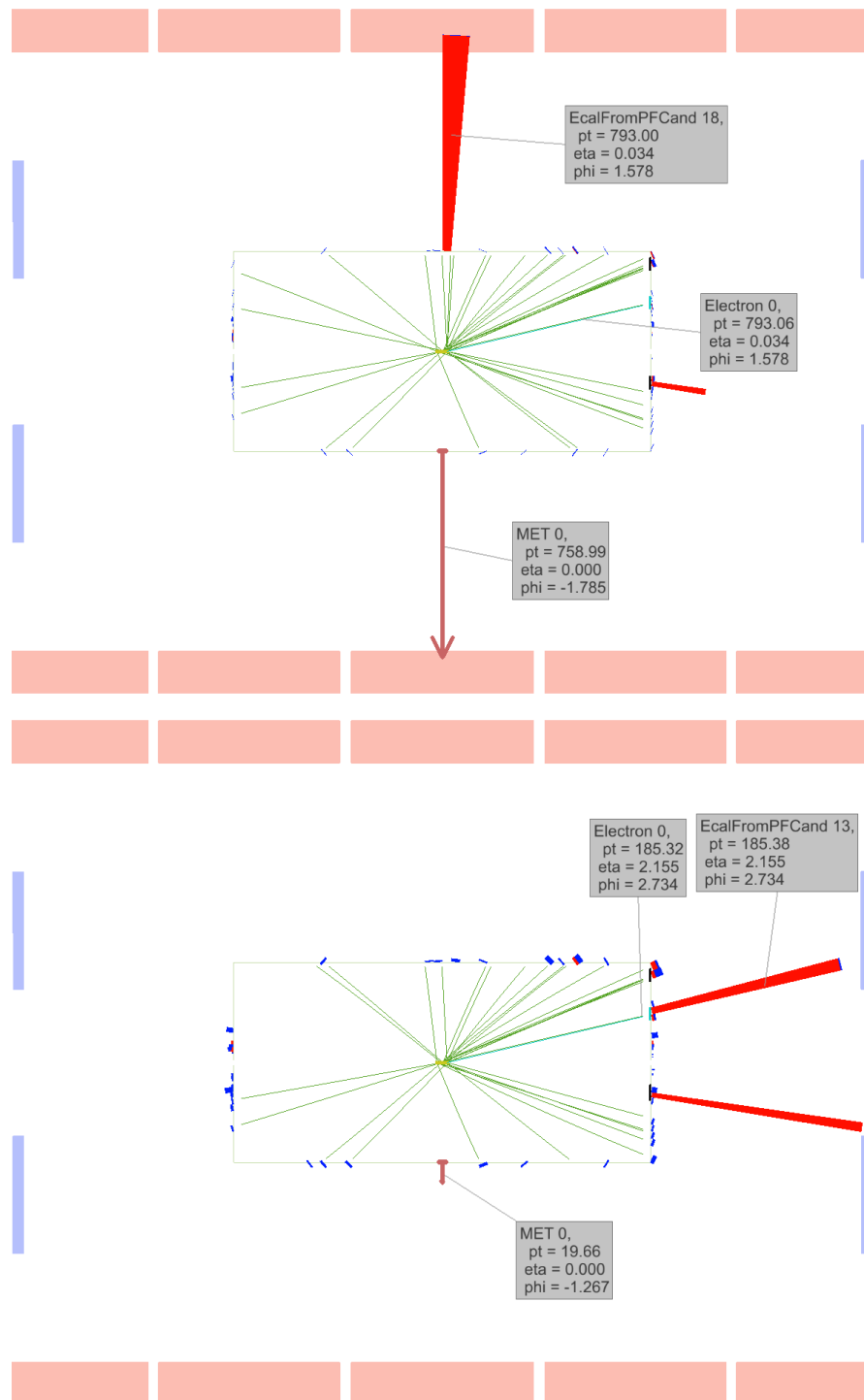|	February 2017	July 2016
p_T	793.1 GeV	185.3 GeV
PF η(e)	0.034	2.155
PF ϕ(e)	1.578	2.734
GSF η(e)	2.154	2.155
GSF ϕ(e)	2.736	2.732
SC η(e)	2.172	2.173
SC ϕ(e)	2.730	2.731
SC E(e)	793.524 GeV	809.945 GeV
E_T^{miss}	759 GeV	19.7 GeV

Figure 5.1.1: Event display of one event where electron track mismatching appears (reconstruction with a problem in the particle flow algorithm from February 2017 on the top and the correct track matching reconstruction from July 2016 on the bottom). The arrow on the bottom indicates the calculated E_T^{miss}, the red cones show the deposition in the ECAL and the light blue line shows the vertex track connected to the reconstructed GSF electron.

5.2 MET Filter

Different effects of the detector electronics or the reconstruction algorithm can lead to issues in the reconstructed events. To address these issues, so called MET-Filters [79, 80] have been developed. If an event shows one of these issues described below, it is not further used in the analysis:

- **Primary vertex filter:** If a deposit in the calorimeter is lacking in the number of tracks, the event is rejected. This can happen if the tracking algorithm fails due to very high number of clusters or if the hard collision happens not in the center of the detector [79].

- **Beam halo filter:** Machine induced particles produced through interactions of the beam with gas or the pipe can lead to a halo of particles that can interact with the calorimeters. These events are filtered by the beam halo filter [81].

- **HBHE noise filter:** Multichannel hybrid photodiodes (HPD) are used to convert the optical output of the HCAL detector parts into an electrical signal. The HBHE scintillator tiles in the HCAL can produce sporadic anomalous signals that affect either one or a few HPD pixels (Ion Feedback Noise), most of the pixels in a HPD (HPD Noise) or nearly all 72 channels in a given read-out box (RBX Noise). The HBHE noise filter uses the number of occupied HPD pixels and the pulse shape information to reject noise events [82].

- **HBHEiso noise filter:** Additional to the already explained HBHE noise filter, the Isolation-based noise filter uses potential noise clusters in the HCAL and close-by activity in the ECAL, HCAL and tracker to filter out HBHE noise [82].

- **ECAL TP filter:** The ECAL has crystals, that are masked in reconstruction due to single noise. Additionally, there are masked crystals in the very front end or front end without a data link. Those crystals without a data link can produce fake MET due to a loss of energy in that region. The trigger primitive (TP) filter rejects events where the masked cells saturate at a TP E_T of 63.75 GeV [83, 84].

- **Bad PF Muon Filter:** This filter rejects events in which the overall quality of the muon is not sufficient, combined with a large p_T, but was still categorized as a particle flow muon[85].

- **Bad Charged Hadron Filter:** If a muon does not fulfill the quality criteria to become a particle flow muon it can still become a part of the MET calculation as a charged hadron candidate. The Bad Charged Hadron filter rejects these events by checking the p_T and the segment compatibility of the muon and compares it to the possible charged hadron candidate [85].

- **badSC noise filter:** There are crystal regions in the ECAL endcap that produce energies with an anomalously high amount which leads to high amplitudes in several channels. This filter rejects events with this anomalous high energies [79].

  These filters are applied on data as well as on the Monte Carlo. Only the "badSC noise filter" is applied on data only, following the recommendation [80].

5.3 Electron Identification

To identify electrons, a dedicated electron identification for high p_T (High Energy Electron Positron - HEEP) in its latest version 7 is used [86]. Its discriminating variables are summarized in Table 5.3.1.

Table 5.3.1: Definitions of the selection cuts for the HEEP ID.

Variable	Barrel cut	Endcap cut
E_T	$>35\,\text{GeV}$	$>35\,\text{GeV}$
η range	$|\eta_{SC}| < 1.4442$	$1.566< |\eta_{SC}| < 2.5$
isEcalDriven	$=1$	$=1$
$|\Delta\eta_{in}^{seed}|$	< 0.004	< 0.006
$|\Delta\phi_{in}|$	< 0.06	< 0.06
H/E	$< 1\,\text{GeV}/E + 0.05$	$< 5\,\text{GeV}/E + 0.05$
full 5x5 $\sigma_{i\eta i\eta}$	n/a	< 0.03
full 5x5 E^{2x5}/E^{5x5}	> 0.94 OR $E^{1x5}/E^{5x5} > 0.83$	$<$ n/a
EM + Had Depth 1 Isolation	$< 2\,\text{GeV}+0.03{\cdot}E_T +0.28{\cdot}\rho$	$< 2.5 + 0.28 \cdot \rho$ for $E_T < 50\,\text{GeV}$
		else $< 2.5\,\text{GeV} + 0.03 \cdot (E_T - 50\,\text{GeV}) + 0.28 \cdot \rho$
Track Isol p_T	$<5\,\text{GeV}$	$<5\,\text{GeV}$
Inner Layer Lost Hits	$\leqslant 1$	$\leqslant 1$
$|dxy|$	$<0.02\,\text{mm}$	$<0.05\,\text{mm}$

The identification uses mostly geometry and isolation criteria[87]:

- **E_T:** The transverse energy deposited in the ECAL has to be higher than $35\,\text{GeV}$.

- **isEcalDriven:** The electron reconstruction has to be seeded by the ECAL (see Subsection 5.1.2)

- **$|\Delta\eta_{in}^{seed}|$, $|\Delta\phi_{in}|$:** The distance between the ECAL measurement and the reconstructed track in η and ϕ has to be small to make sure that the track is associated with an electron and not wrongly connected to a neutral particle.

- **H/E:** A requirement to the hadronic energy deposition H compared to the supercluster energy is applied ($H/E < 1\,\text{GeV}/E + 0.05$) because the expected amount of deposition from the electron is assumed to be small.

- **full 5x5 $\sigma_{i\eta i\eta}$, full 5x5 E^{2x5}/E^{5x5}:** The spread of the energy around the seed crystal has to fulfill requirements in the barrel (full 5x5 $E^{2x5}/E^{5x5} > 0.94$ OR $E^{1x5}/E^{5x5} > 0.83$) and endcaps (full 5x5 $\sigma_{i\eta i\eta} < 0.03$) to distinguish between electromagnetic and hadronic showers. E^{2x5} and E^{5x5} describe the energy deposition in an array of 2×5 and 5×5 crystals around the seed crystal in the barrel of the ECAL. 5x5 $\sigma_{i\eta i\eta}$ describes the width of the shower around an array of 5×5 crystals around the reconstructed seed crystal in the endcaps (see Subsubsection 3.2.2).

- **EM + Had Depth 1 Isolation:** The electron has to be isolated of ECAL transverse energy hits with $E_T > 0.08\,\text{GeV}$ ($E_T > 0.1\,\text{GeV}$) in the barrel (endcaps) around a cone with a radius of 0.3 excluding an inner cone of a radius of 3 crystals at the electron's position. Additionally, it has to be isolated from HCAL energy depositions in a cone with a radius of 0.3 excluding an inner cone with a radius of 0.15. These two isolations are combined and compared to the E_T of the electron and the mean energy density per unit area ρ to suppress jets that are identified as electrons.

- **Track Isol p_T:** The sum of the p_T in a cone with a radius of 0.3 excluding an inner cone with a radius of 0.04 has to be smaller than $5\,\text{GeV}$ to suppress jets as well.

- **Inner Layer Lost Hits:** The number of lost hits where a tracker sensor in the inner layer part did not fire in the reconstructed trajectory has to be small to suppress electrons originating from pair production.

- **$|dxy|$:** The reconstructed track has to be close to the primary vertex.

As in the electron reconstruction, the identification can behave differently in the simulation and the measured data. The scale factors corresponding to the HEEP ID are provided by the Z' group [88] and are $0.972 \pm 0.006(syst.)$ (barrel) and $0.983 \pm 0.007(syst.)$ (endcap). The statistical errors on the scale factors are negligible.

5.4 Trigger Strategy

The main trigger for this analysis is a single electron trigger with a threshold of 115 GeV. During the analysis of the dataset, a deficit for high E_T electrons in data compared to simulation has been found. After excluding all other possible causes for this deficit, for example issues with the normalization of the Monte Carlo, a trigger study on an orthogonal muon data set has been performed. This was done by the developer of this specific trigger path, Jeongeun Lee, and showed that, for high E_T, the efficiency of the trigger drops significantly (see Figure 5.4.1). To compensate this effect, an additional single photon trigger has been added. As shown in Figure 5.4.1 adding this trigger as an OR recovers most of the efficiency loss of the single electron trigger at high E_T. This overall recovers about 2% of data that did not trigger the single electron but the single photon trigger. For electrons with a p_T greater than 500 GeV, a gain of about 16% in events is achieved by this trigger combination.
To avoid turn-on effects from the triggers, a fit in the low E_T has been performed and a 99% efficiency point has been calculated (see Figure 5.4.2). This leads to a sufficient threshold value on the electron E_T of 130 GeV. Additionally, the effect of the triggers to MC and data has been compared and used to derive scale factors to match the behavior of the simulation to the data. For electrons with a p_T up to 800 GeV, the measured data and the MC simulation show similar behavior, resulting in scale factors between 0.97 and 1.01 with an uncertainty of less then 1% up to 1.5% in the barrel. For high energetic electrons with a p_T of 800 GeV or higher, the inefficiency in the data leads to a scale factor of 0.86 with an uncertainty of about 8%. In the endcaps, the behavior of the measured data and the Monte Carlo is in good agreement resulting in scale factors between 0.98 and 1. All calculated scale factors can be found in appendix (Table 10.2.1).

To avoid double counting of events by using two datasets that both contain the single electron trigger, a cleaning of the datasets has been performed. This means, if either only the single electron trigger or both triggers have fired, the single electron dataset is used. Otherwise, if only the single photon trigger has fired, the single photon dataset is used.
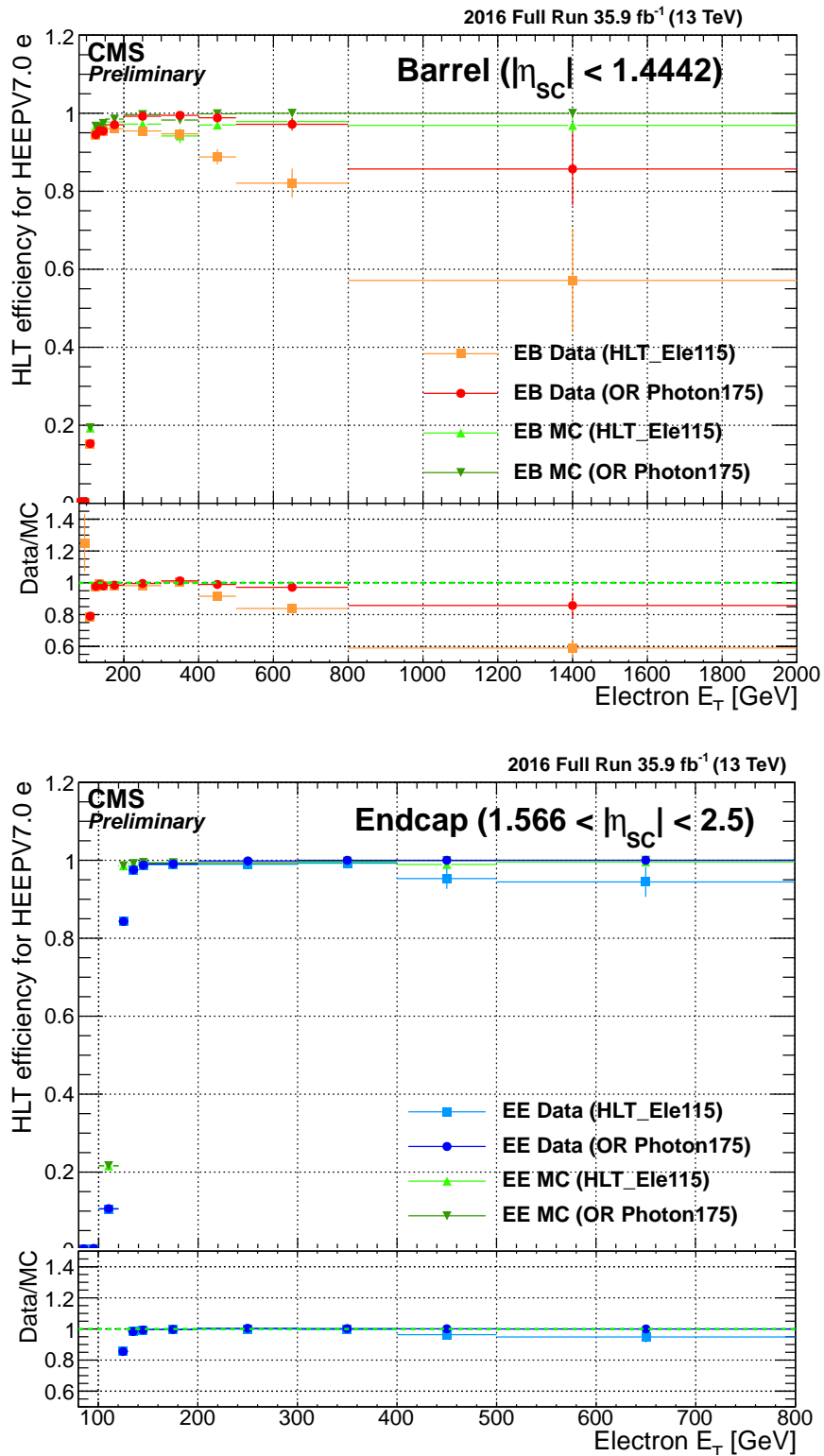
Figure 5.4.1: Efficiency of the single electron trigger and the combination of the single electron and single photon trigger in the barrel (top) and endcap (bottom) for data and Monte Carlo. (By Jeongeun Lee, taken from [66])
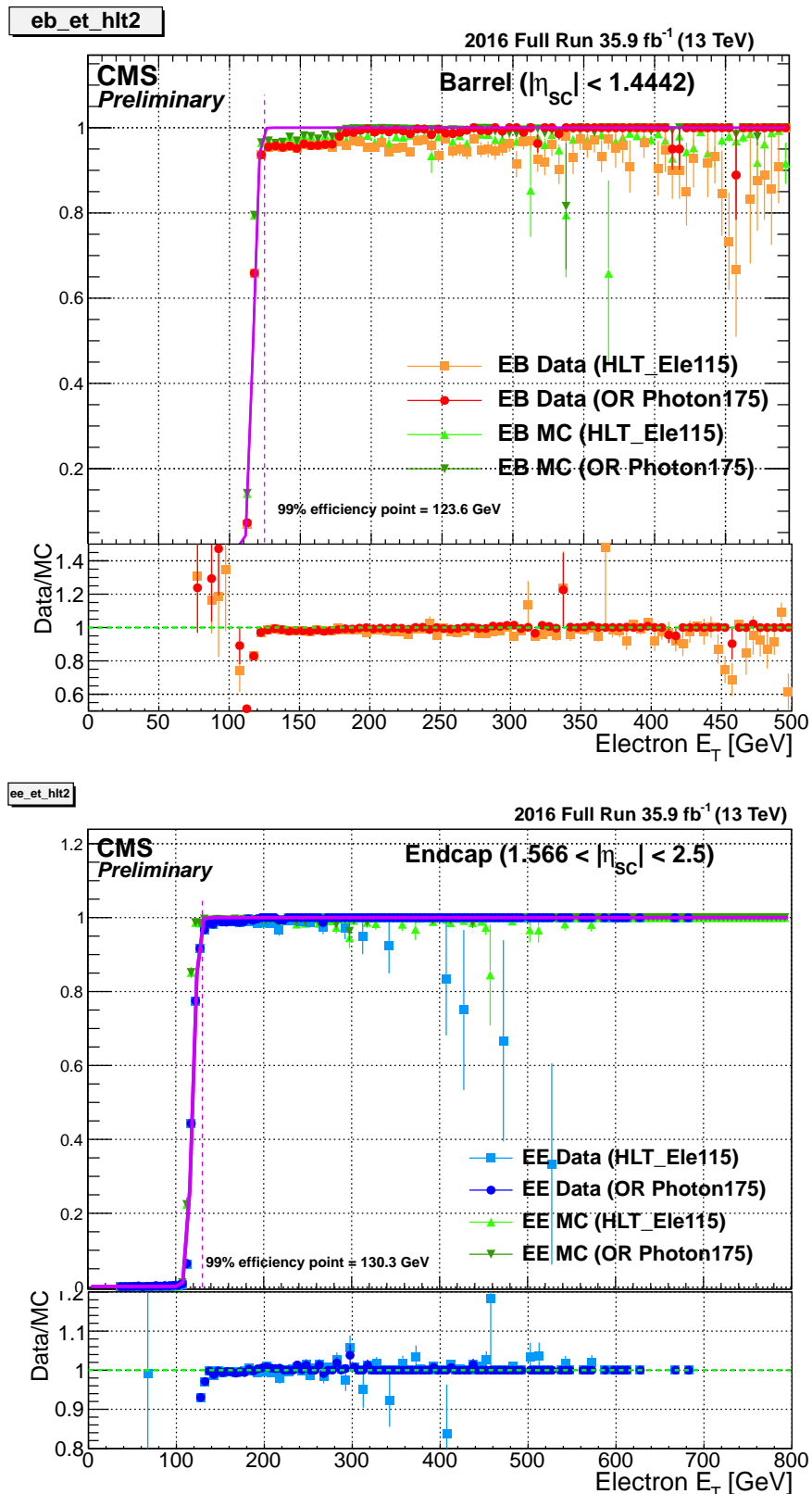
Figure 5.4.2: Turn on effect of the triggers shown in the lower E_T regime for the barrel (top) and the endcap (bottom). The fit is used to evaluate the threshold on the electron E_T. (By Jeongeun Lee, taken from [66])

6 Analysis

6.1 Setup

This analysis uses the framework developed by the Aachen workgroup called "Three A Physics Analysis Software" or "TAPAS" [89]. It is built upon the official CMS framework, the CMS software named CMSSW [90]. The data format provided by the CMS collaboration is the "MiniAOD" where "AOD" stands for "Analysis Object Data" and "Mini" indicates a smaller file size. It contains reconstructed objects that already have some high level corrections applied. Additionally, only the most basic quantities like the 4-vector or the Particle Data Group ID [10] are provided to save storage space and computing time.

For even higher efficiency and analysis speed, this data is again reduced by the skimming process using the "PxlSkimmer" provided by the TAPAS framework using the PXL library [91].

The final analysis is then carried out on the Aachen grid system which is part of a world wide CMS computing grid [92].

6.2 Pile-Up Reweighting

As in the LHC not single particles but bunches of protons are collided, at each bunch crossing not one but many interactions happen. These additional total inelastic interactions lead to an increased amount of primary vertices in the event. This effect is called pile-up. The pile-up is described by the number of primary vertices per event, and those depend on the luminosity and the beam conditions.

To handle these additional interactions in simulations, so-called minimum bias events are added. To address the luminosity dependence, a luminosity-based approach has been chosen in CMS. The instantaneous luminosity is measured and multiplied by an approximation of the total inelastic cross section, called minimum bias cross section, which provides the expected number of primary vertices when taking the vertex reconstruction efficiency of about 70% into account. This measured distribution of number of vertices is used to calculate an event based factor to correct the simulation to the specific pile-up conditions:

$$w_{pile-up} = \frac{N_{vertices}^{data}}{N_{vertices}^{mc}} \tag{6.1}$$

Here, $N_{vertices}^{data}$ is the number of primary vertices in the measured data and $N_{vertices}^{mc}$ describes the same number for the simulation. The recommended value of the minimum bias cross section is $\sigma = 69.2\,\text{mb}$, coming from a "best-fit" approach [93]. Figure 6.2.1 shows the number of primary vertices in data and Monte Carlo after all requirements and after applying the pile-up reweighting. The data and Monte Carlo simulations as described in Chapter 4 are used. The different background contributions are split and shown in different colors as a stacked bar histogram. The measured data is visible as black dots with uncertainty bars. Additionally, two signal samples ($M_{W'} = 1.8\,\text{TeV}$ and $3.8\,\text{TeV}$) are shown as a black and dark green solid line. Under the histogram, the ratio of the data and the MC is plotted. The number of primary vertices can be seen on the x-axis and the number of events is shown on the y-axis in a logarithmic scale.

A shift of the Monte Carlo distribution to higher numbers of primary vertices compared to the measured data is visible which indicates some issues with the reweight process and the "best-fit" approach.
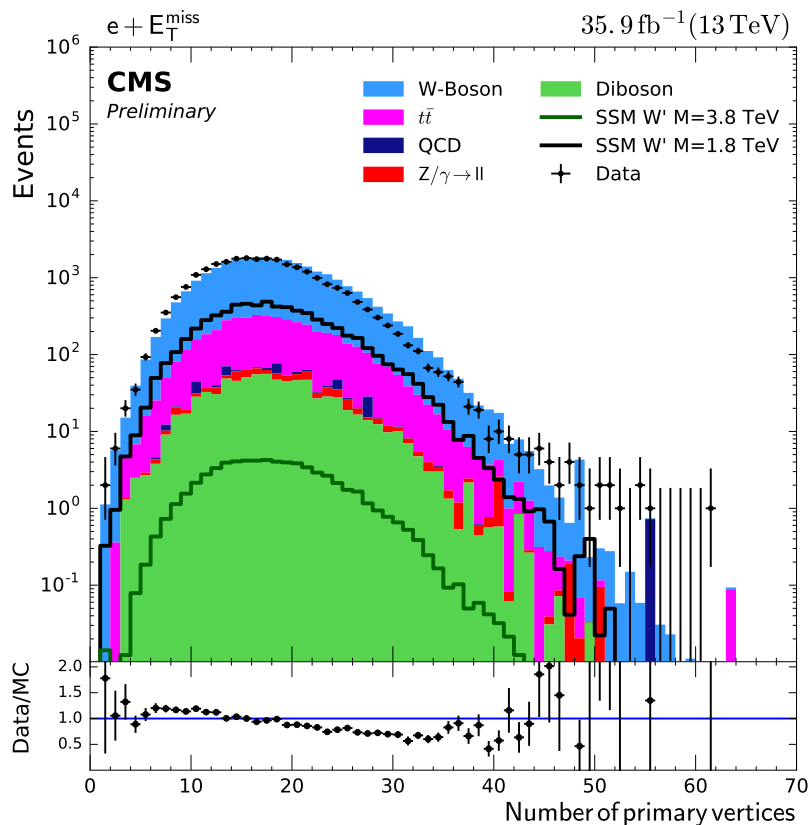

Figure 6.2.1: The number of primary vertices showing the effect of pile-up. The distribution shows a slight shift of the Monte Carlo to higher numbers of vertices.

6.3 Validation of the QCD Monte Carlo using a Data Driven Approach

6.3.1 Data Driven Method

The description of the background contribution originating from QCD processes can be done in two ways. Firstly, it can be taken from Monte Carlo simulations and secondly can be calculated using a data driven method which has been done in earlier versions of this analysis. This section explains the so-called "ABCD-Method" to obtain the multijet contribution from data which is then used to validate the Monte Carlo simulation for the QCD events.
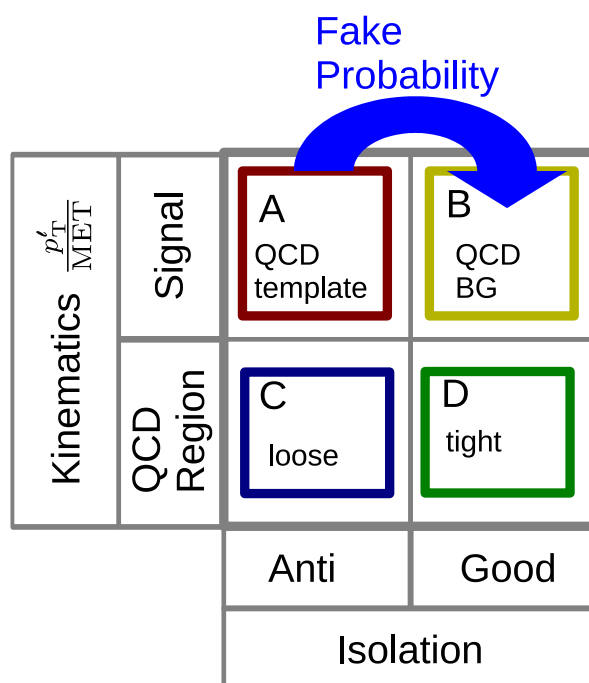A visualization of this method can be seen in Figure 6.3.1.

Figure 6.3.1: Visualization of the ABCD method, dividing the whole dataset into a signal and QCD region with inverted isolation requirements ("Anti") and fulfilling all quality criteria ("Good"). Taken from [66].

As one can see in Figure 6.3.1, one defines a QCD region, where the contribution from multijet processes is expected to be dominant and a signal region, which is the region where the analysis is mainly focusing on. For this analysis, the QCD region is defined by the kinematic selection on the ratio of p_T and E_T^{miss} (see Section 6.5). The QCD enriched region is defined to have a $p_T/E_T^{miss} > 1.5$, whereas the signal region is defined to have $p_T/E_T^{miss} < 1.5$. Additionally, these regions are divided into a "Good" (B,D) and an "Anti" region (A,C). The "Anti" region has inverted isolation

requirements, meaning it contains electrons which only fulfill a looser isolation requirement as explained in Section 5.3 whereas the "Good" region contains only electrons fulfilling all quality criteria. To derive the amount of jets from the "Anti" region being misidentified as a good electron one takes the measured data in region C and D and subtracts the amount, that is described by the electroweak background. Then, region D is divided by region C to obtain the misidentification factor, or "tight-to-loose" ratio. The ratio of D and C is expected to be equal to the ratio of the signal regions B and A, since the two chosen variables are uncorrelated. Therefore, this ratio can then be applied to the QCD template A which yields the final QCD contribution by misidentified jets in the isolated electron region.

6.3.2 Validation of the QCD Monte Carlo Simulation

As this method showed good performance and was approved in earlier analysis, it is used to validate the simulation of the QCD event contribution from Monte Carlo simulation. The explained method is performed but instead of using measured data, the electroweak background together with the QCD events from MC take its place. The final outcome of the multijet description is compared to the Monte Carlo simulation. Figure 6.3.2 shows the contribution derived from data together with the Monte Carlo simulation of QCD for the electron p_T and E_T^{miss}. Both methods agree well and show comparable statistics. The problem of lacking statistics in the MC was therefore solved in newer generations of Monte Carlo production. The deviation between MC simulation and the contribution derived from the data driven method is used as a systematic uncertainty on the QCD contribution and was estimated to be 40%.

As the validation of the QCD simulation shows similar statistics between Monte Carlo and the contribution derived from the data driven method and a comparable description of the shape, this analysis uses QCD from Monte Carlo simulations. Additionally, this prevents the introduction of possible bias due to the data driven method.
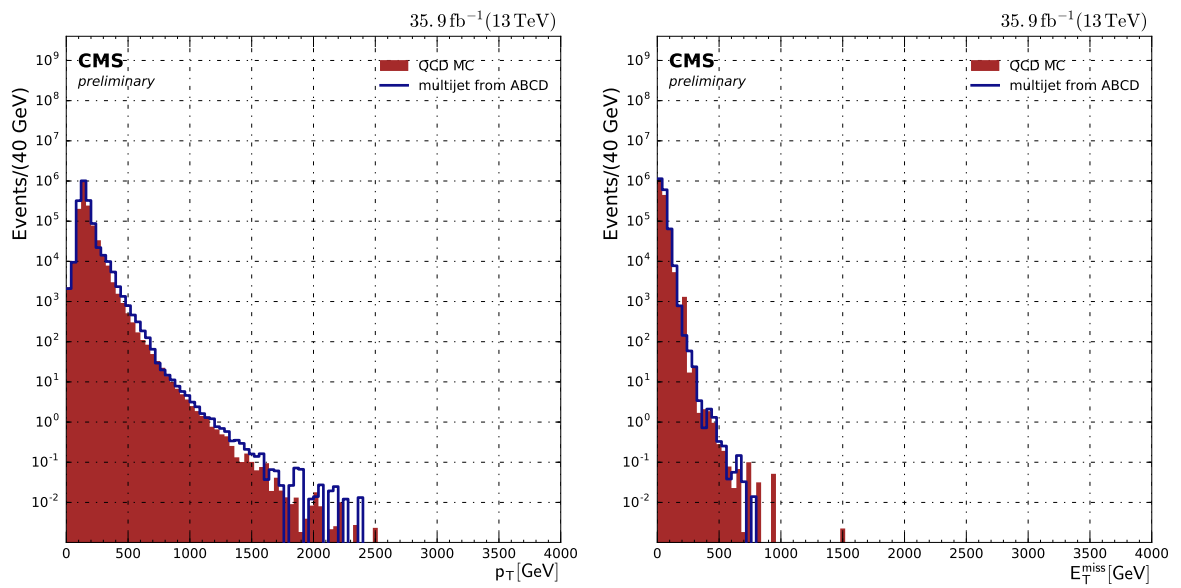
Figure 6.3.2: Distributions of the electron p_T (left) and E_T^{miss} (right) coming from QCD MC (red bars) and the data driven approach (blue line). The closure test indicates, that the method is working properly. Both approaches show similar behavior and comparable statistic.

6.4 Evaluation of Systematic Uncertainties

The outcome of an experiment is influenced by systematic uncertainties which have to be taken into account in the prediction of the measurement. These uncertainties effect either the shape of the M_T distribution, e.g. an uncertainty on the electron energy scale, or the normalization, e.g. arising from the luminosity uncertainty. This section describes all systematic uncertainties considered for the final distribution in M_T. They are evaluated by repeating the analysis where the uncertainty specific values are shifted in both ways, according to the official recommendations. They are also important as an input for the statistical interpretation (see Subsection 8.1.1). The considered uncertainties in this analysis are:

- Luminosity: Following the official recommendation from the 2016 luminosity measurement [94], the uncertainty on the luminosity is set to 2.5%.

- PDF: As the accelerated protons are not elementary particles, one is interested in the description of the constituents kinematics. The Parton Distribution Function (PDF) [95] describes how the momentum of the proton is carried out to these partons. Following the recommendation for LHC Run-II of the PDF4LHC group [96], three different PDF sets are combined and the change to the background prediction is evaluated on bin by bin basis and used as the systematic uncertainty. This results in an uncertainty on the theoretical cross section and on the acceptance. The uncertainty on the acceptance, originating from the choice of the PDF set, was evaluated to be less than 1%. The uncertainty on the cross section leads to an uncertainty on the normalization of the background contribution. In contrast to the background, the uncertainty on the theoretical signal cross section is not propagated to the normalization as the signal cross section will be the parameter of interest in the statistical interpretation (see Subsection 8.1.2).

- Pile-Up: Following the recommendation of the LUMI POG [97], the uncertainty on the minimum bias cross section is 4.6%. The value of 69.2 mb is shifted by this uncertainty and a new reweighting distribution is generated. This is then used to evaluate the impact on the shape of the distribution.

- k-factor on W- background: As explained in Subsection 4.2.2, there are two different approaches to combine QCD and electroweak corrections. The difference between the additive and the multiplicative approach is taken as an uncertainty and was evaluated to be around 5%.

- Electron Scale Factors: As explained in Chapter 5, the reconstruction and identification as well as the chosen trigger combination need scale factors to address different behavior in simulation and data. These factors have systematic uncertainties attached to them which are taken into account by shifting the specific factor by its uncertainty. The dominant scale factor uncertainty is

coming from the trigger scale factors. It is about 2% for low p_T electrons and rises up to 8%.

- Electron Energy Scale: The systematic uncertainty on the electron energy scale was determined by comparing simulation and data in the Z peak region [98]. Its uncertainty was measured to be 0.4% in the barrel and 0.8% in the endcap region.

- Jet Energy Scale: The jet energy scale is corrected following the recommended Jet Energy Correction (JEC) [99]. The uncertainty is applied by shifting the jet energy following the latest numbers depending on the p_T and η can be found in [100]. This uncertainty is important for the E_T^{miss} uncertainty calculation.

- Jet Energy Resolution: Not only the jet energy scale but the resolution is corrected as well [101]. The uncertainty of the resolution depends on the p_T and η of the jet. The energy is varied by using a Gaussian distribution with the nominal energy value as the mean component and the initial resolution $\pm$ its uncertainty as the standard deviation. This leads to new values of the energy components of the jet. This jet energy smearing effects the calculation of the the uncertainty on the E_T^{miss}.

- E_T^{miss} Scale: As the calculation of E_T^{miss} depends on the values from all objects, the uncertainty on E_T^{miss} is evaluated by shifting each contributing object (e.g. electrons, jets, ...) in its energy values, as explained before, individually. The resulting difference in the E_T^{miss} is used as the uncertainty. Additionally, as explained in Subsection 5.1.3, the energy not connected to a reconstructed object, is used for the E_T^{miss} calculation. The uncertainty on this unclustered energy is set to 10%.

The relative uncertainties as a function of M_T can be seen in Figure 6.4.1. For lower M_T regions, the uncertainty on the electron energy scale dominates with the constant 5% uncertainty on the k-factor being the subleading one. At about 1.5 TeV, the trigger scale factor uncertainty becomes more important with an uncertainty of about 8% for electrons in the barrel. For a M_T greater than 3 TeV, the PDF uncertainty becomes the most important one with a value of about 60% at 4 TeV in M_T.
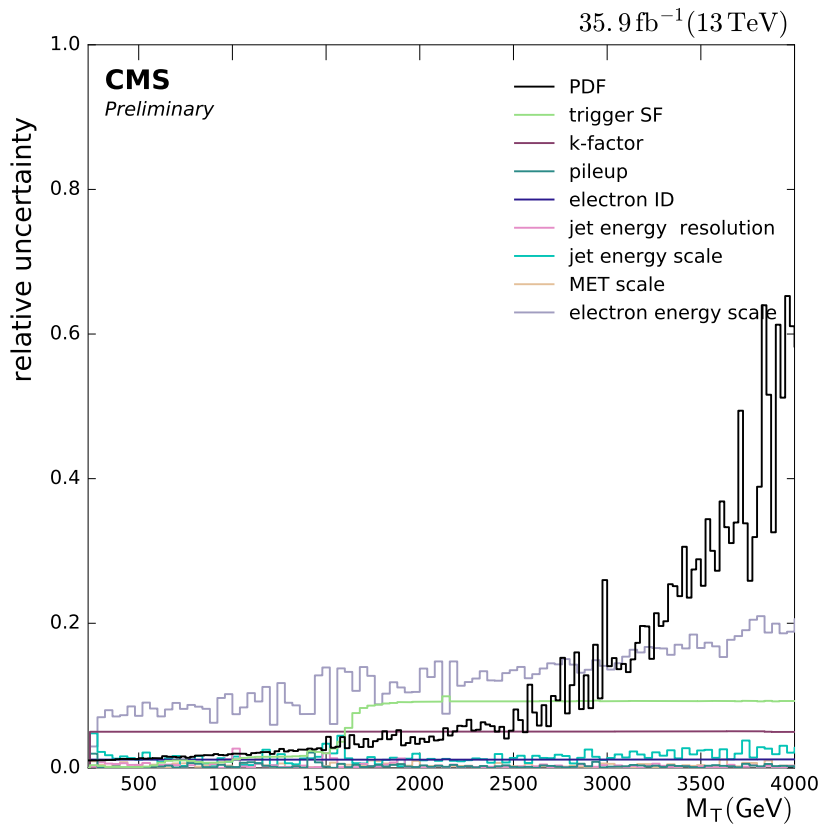
Figure 6.4.1: Visualisation of the systematic uncertainties. The electron energy scale is the dominant uncertainty until the PDF uncertainty rises above 20% for high M_T values.

6.5 Analysis Specific Selection Criteria

Additionally to the general selection (Chapter 5), the events have to fulfill analysis specific requirements. A second lepton veto is applied so that events containing an additional electron, muon or tau with a $p_T > 25$ GeV are rejected. As it is shown in Figure 6.5.1, the simulation of the E_T^{miss} seems to have some problems in the lower region of the spectrum. This can be due to jets that recoil from a Z or a W boson which can lead to "fake-E_T^{miss}" and is hard to simulate. To avoid this mismodeled low E_T^{miss} region, an additional $E_T^{miss} > 150$ GeV requirement has been applied. This requirement also suppresses the background contribution originating from Z/γ decays while leaving the signal contribution mostly untouched. Additionally to these basic selection steps, the kinematics of the decay is taken into account. Due to the fact that the W′ is assumed to decay at approximately zero momentum via a two body decay, the electron and the neutrino are expected to have nearly the same momentum. These back-to-back kinematics in the laboratory frame also lead to an angle between both particles of around π.
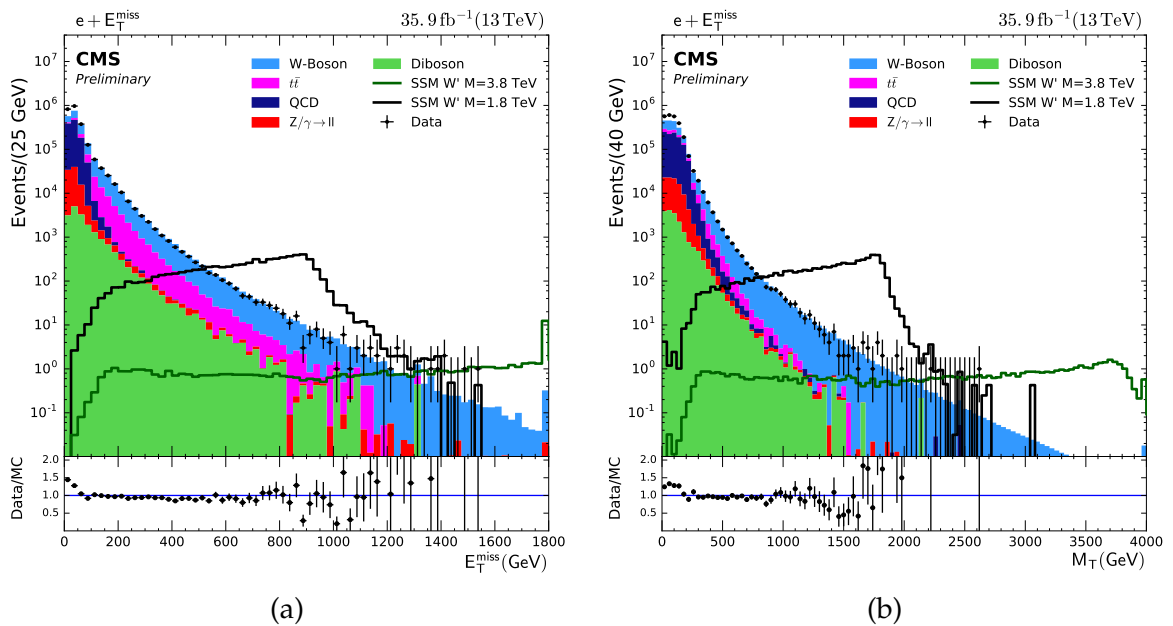

(a)   (b)

Figure 6.5.1: Distributions of the E_T^{miss} (a) and M_T (b) without kinematic requirements applied. Some mismodeling in the lower E_T^{miss} regions can be seen which propagates to the M_T distribution.

Figure 6.5.2 shows the distributions of the angle between the electron and the E_T^{miss}, $\Delta\phi(e, E_T^{miss})$, and the ratio p_T/E_T^{miss} before and after applying the other kinematic selection (p_T/E_T^{miss} criterion on the $\Delta\phi$ and the $\Delta\phi$ criterion on the p_T/E_T^{miss}). The arrows indicate the values of $\Delta\phi(e, E_T^{miss}) > 2.5$ and $0.4 < p_T/E_T^{miss} < 1.5$. As one can

see, the signal contribution lies manly in these regions, therefore they are called "signal regions". These kinematic requirements have already been used and optimized in earlier publications of this analysis [4–7].

The description of the QCD contribution seems to deliver sufficient statistics before and after applying the kinematic cuts, as expected after performing the test with the data driven method (see Section 6.3). The distribution of the p_T/E_T^{miss} after demanding $\Delta\phi > 2.5$ show some disagreement between simulation and measured data for higher values which indicates missing statistics especially in the description of the diboson background as this background shows some empty bins in the spectrum. This might be treated in newer productions of the diboson Monte Carlo simulation with a bigger number of simulated events. As this region lies outside of the "signal region", it does not effect the final distribution.
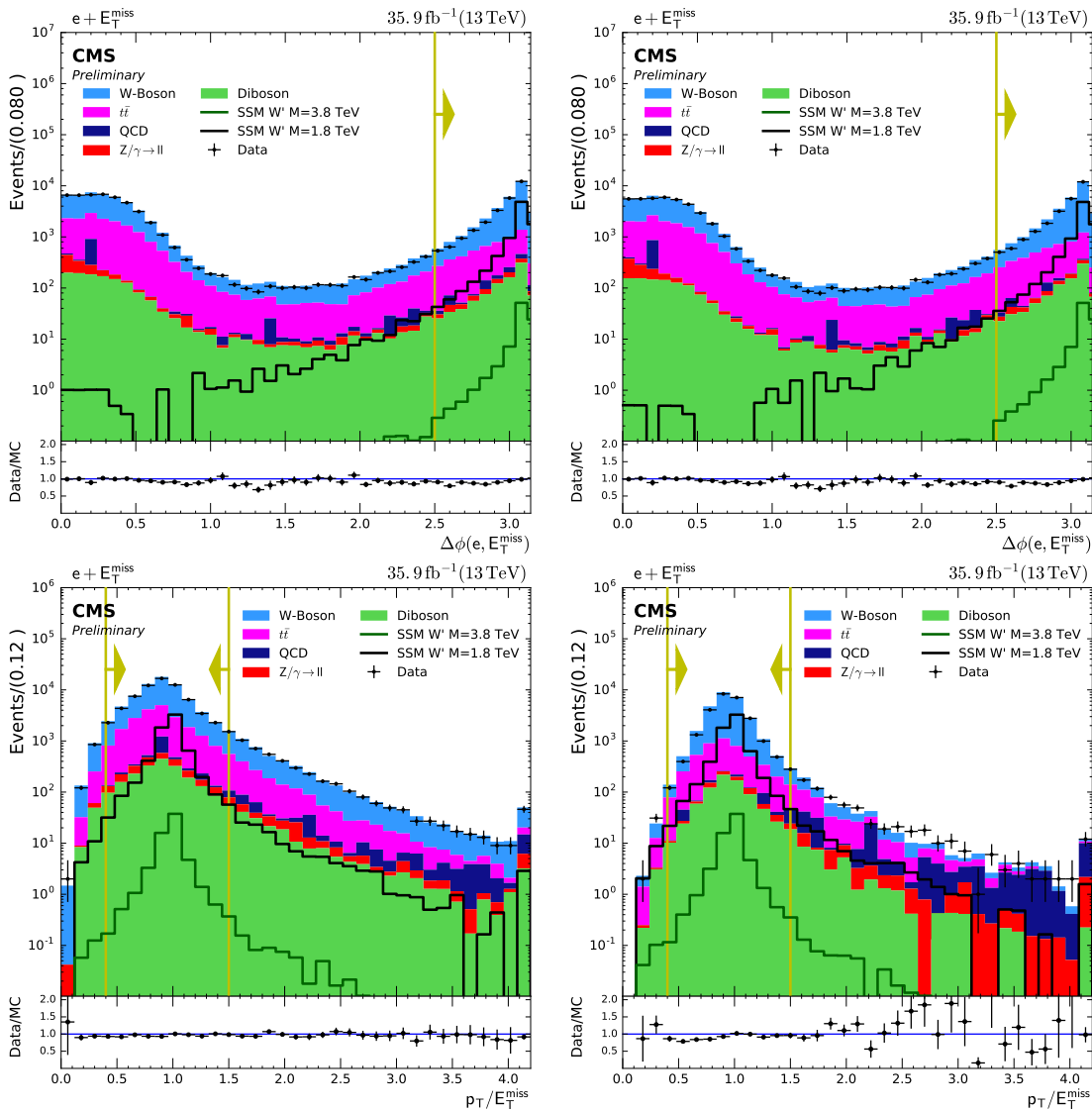

Figure 6.5.2: Distributions of the $\Delta\phi$ between the electron and E_T^{miss} (top) and the ratio of the p_T and the E_T^{miss} (bottom) before (left) and after (right) applying the other kinematic selection.

6.6 Full Background Prediction

Applying all the explained quality criteria and analysis specific cuts, the following section compares the distributions containing the full background prediction with the measured data.

To show the impact of each quality requirement and additional cuts, Figure 6.6.1 shows the number of events in data and simulation after each cut. Additionally, Table 6.6.1 shows the relative number of events after each applied selection cut with respect to the number of events before the selection. The requirement of one single electron fulfilling the identification criteria has the biggest impact on the event yield. The following E_T^{miss} requirement of 150 GeV reduces the number of events in the low E_T^{miss} region of the data and the background simulation, but has only a small impact on the signal contribution. The kinematic selection reduces the background by about 50% but leaves the signal nearly untouched. After all requirements are applied, the number of events in data stay in agreement to the predicted amount from simulation.

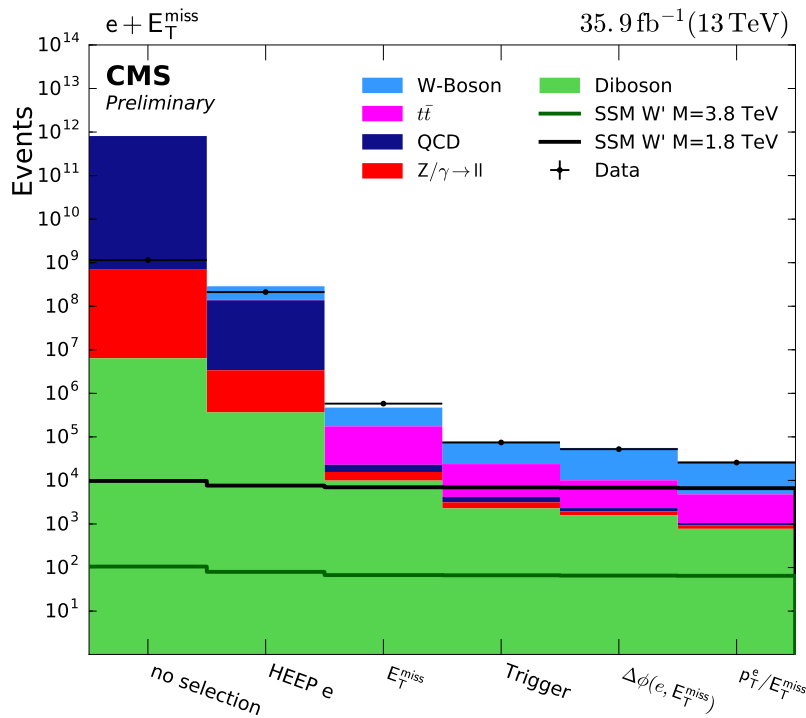Figure 6.6.1: Visualization of the impact of each requirement applied in this analysis.

Figure 6.6.2 shows the distribution of the fundamental variables η and ϕ of the electron. In η, the overlap region of barrel and endcaps can be seen at around $\eta = \pm 1.4$. This lower event yield is expected due to the geometry of the detector. The simulation shows small differences to the measured behavior which indicates a

Table 6.6.1: Relative number of events after the different selections with respect to selection before, where "HEEP e" is an HEEP electron with $p_T > 35\,\mathrm{GeV}$ followed by the $E_T^{miss} > 150\,\mathrm{GeV}$ requirement. The trigger selection requires the electron to have a $p_T > 130\,\mathrm{GeV}$.

	No selection	HEEP e	E_T^{miss}	Trigger	kinematic selection
Data	1.0000	0.1859	0.0018	0.1426	0.4768
SM Background	1.0000	0.0512	0.0018	0.1824	0.4848
SSM W' M=1.8 TeV	1.0000	0.7982	0.9675	0.9945	0.9594
SSM W' M=3.8 TeV	1.0000	0.7646	0.9273	0.9908	0.9734

difficulty to simulate this region properly. At high positive values of η, a deficit in data is observed. The asymmetry could indicate an inefficiency in this region of the detector, as this effect does not show up in the opposite sign of η.

In ϕ, a slight modulation can be seen, resulting in a minimal deficit in data at around $\phi = 0$. Until this point, no reasonable explanation besides statistical fluctuations for this effect could be found.

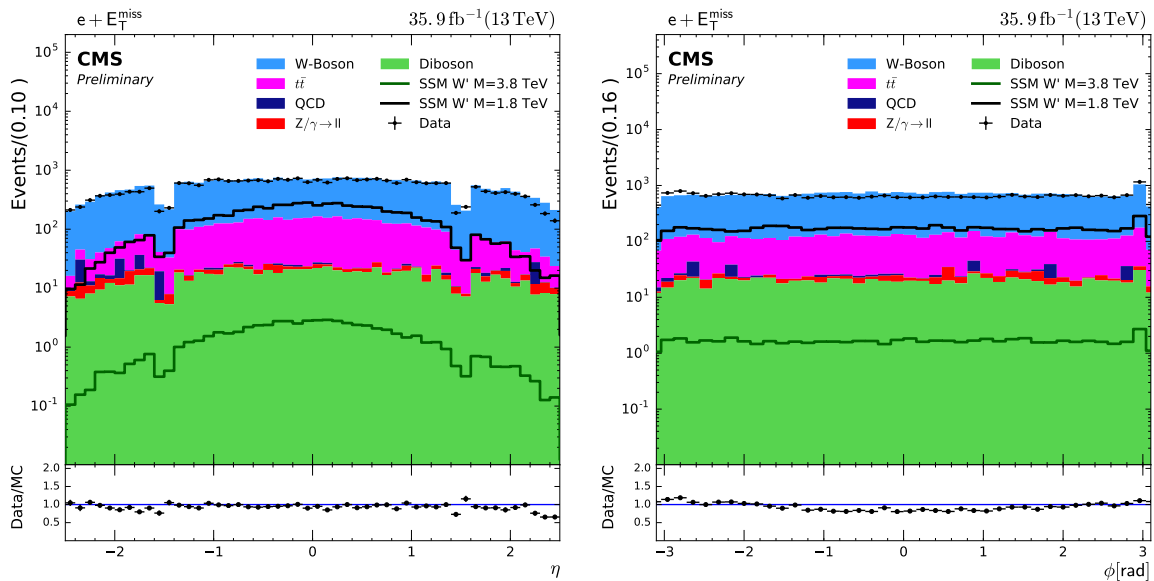Figure 6.6.2: Distributions of η (left) and ϕ (right) of the electron show good agreement between simulation and measurement.

The distributions of the kinematic variable p_T can be seen in Figure 6.6.3. Additionally to the visualization of the full η range, the barrel and endcap regions are displayed. The grey band visualizes the systematic uncertainties. The overall agreement between

data and monte carlo in the full η range is good. At a p_T of about 525 GeV, a slight fluctuation is observed, which can be explained by a statistical effect. Additionally, a drop in the measured data at around a p_T of 700 GeV up to about 780 GeV can be seen with a data to Monte Carlo ratio of about 17% at 725 GeV. The number of expected events in this bin is about 6 whereas the number of measured data events is 1. Performing a significance test as described in [102], considering the uncertainty on the background prediction of 13.5% on this bin, shows a deviation of 1.9 σ and therefore can be explained by a statistical effect as well.
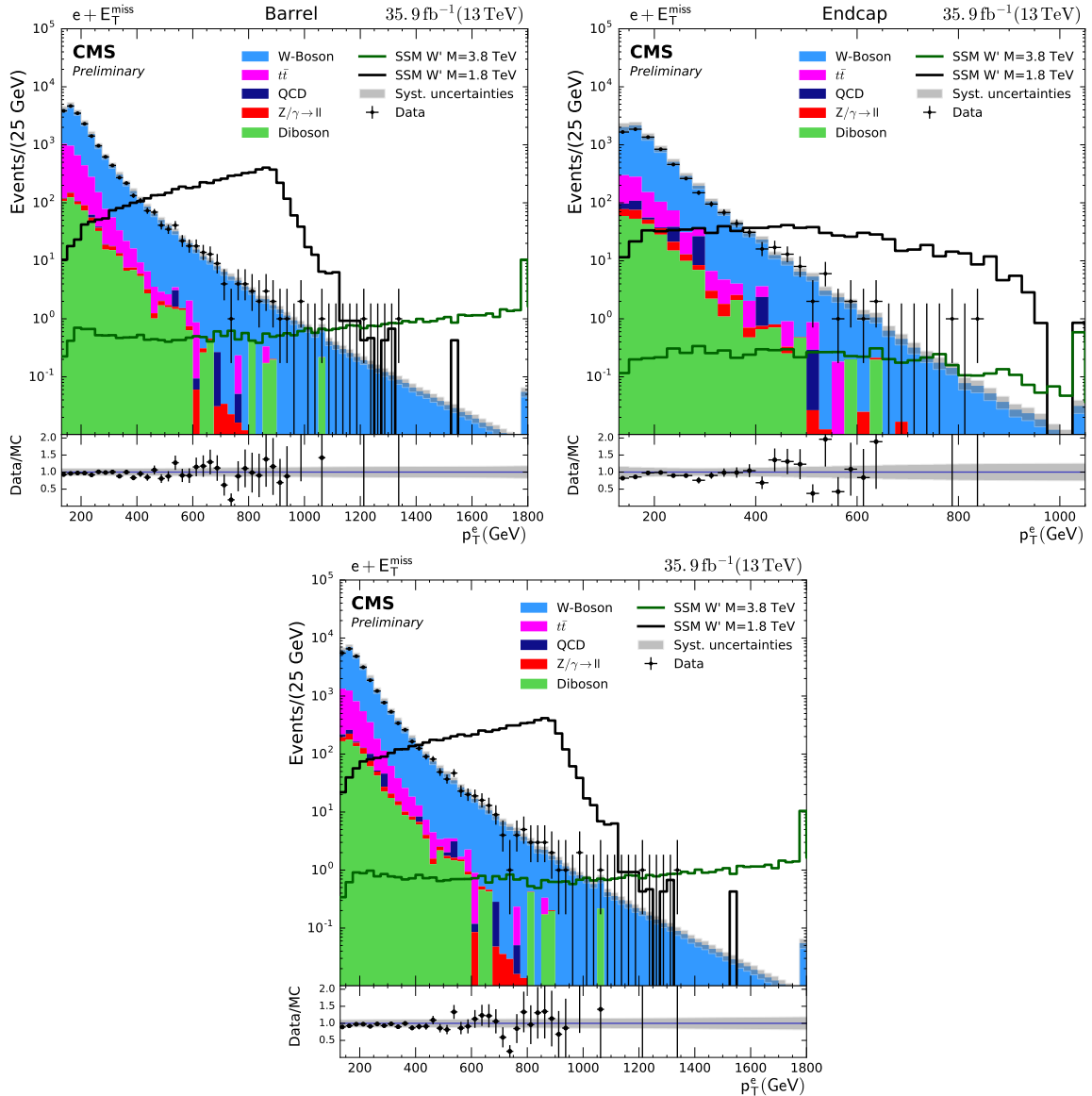

Figure 6.6.3: Distribution of the electron p_T in the barrel (top left), endcap (top right) and full eta range (bottom). Each region shows good agreement between data and Monte Carlo with slight features that are consistent with statistical fluctuations.

Figure 6.6.4 shows the distributions of the E_T^{miss}, also split into the barrel and the endcap region. The features that where observed in the p_T distributions can be seen in the E_T^{miss} as well. They appear at about the same E_T^{miss} values, as the back-to-back kinematic leads to nearly the same electron p_T and E_T^{miss} in an event. Therefore, the statistical explanation holds as well.
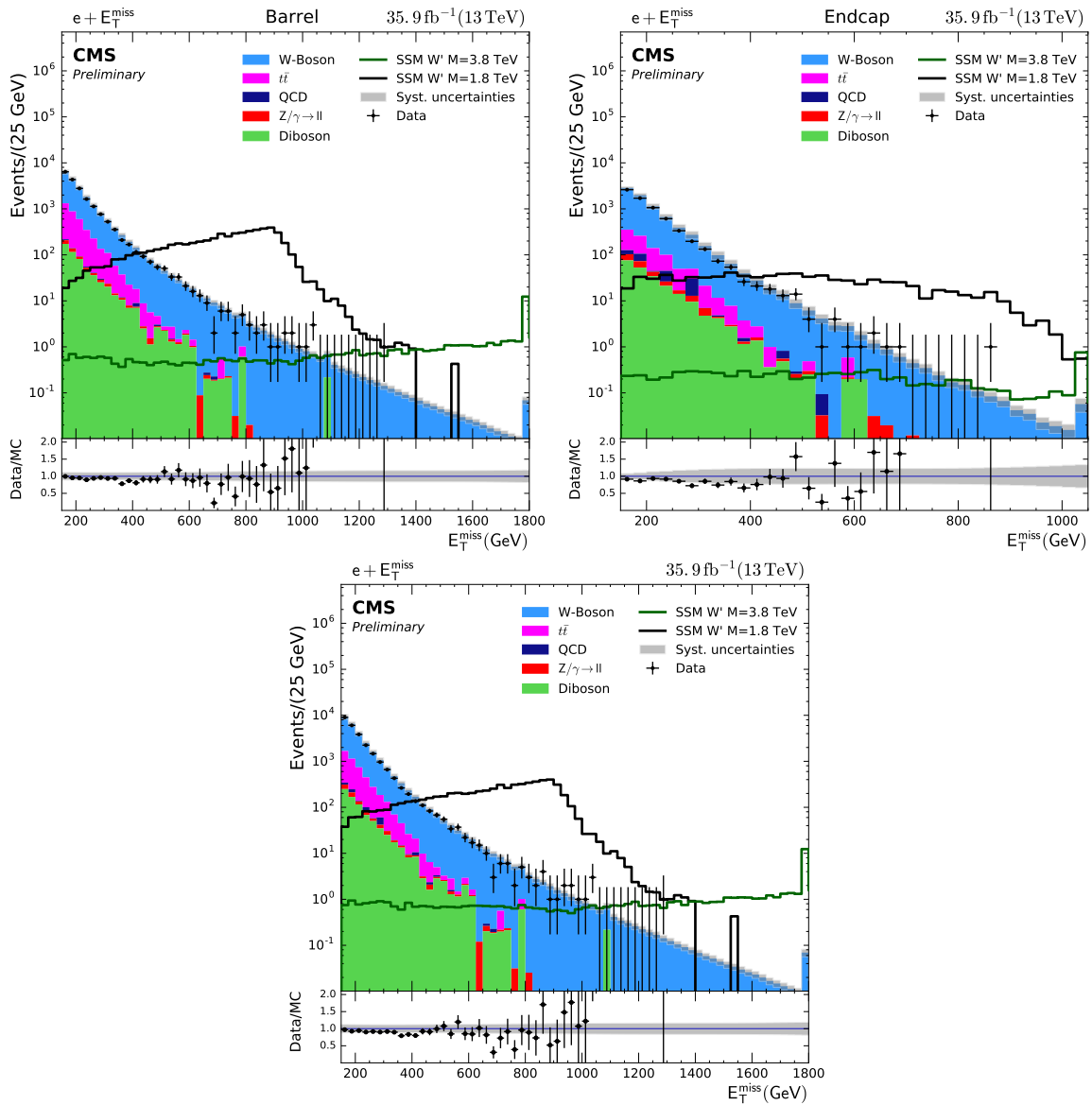

Figure 6.6.4: Distribution of the E_T^{miss} in the barrel (top left), endcap (top right) and full eta range (bottom). Each region shows good agreement between data and Monte Carlo with slight features that are consistent with statistical fluctuations.

7 Results

7.1 Final Distributions

After describing all steps required for the analysis and showing the important fundamental variables, the final distribution of the discriminating variable M_T is shown in Figure 7.1.1. All selection requirements are applied. The grey band indicates again the systematic uncertainties. Additionally, a cummulative plot is shown where the bins indicate the sum of number of events above the specific M_T value. The first bin of the M_T distribution starts at 230 GeV. The highest M_T event has a p_T of 1338 ± 13 GeV and a E_T^{miss} of 1288 ± 13 GeV, which leads to a final M_T of 2620 ± 20 GeV. This is about 600 GeV higher than the highest M_T event for this specific search from 2015 [7] with 2 TeV.
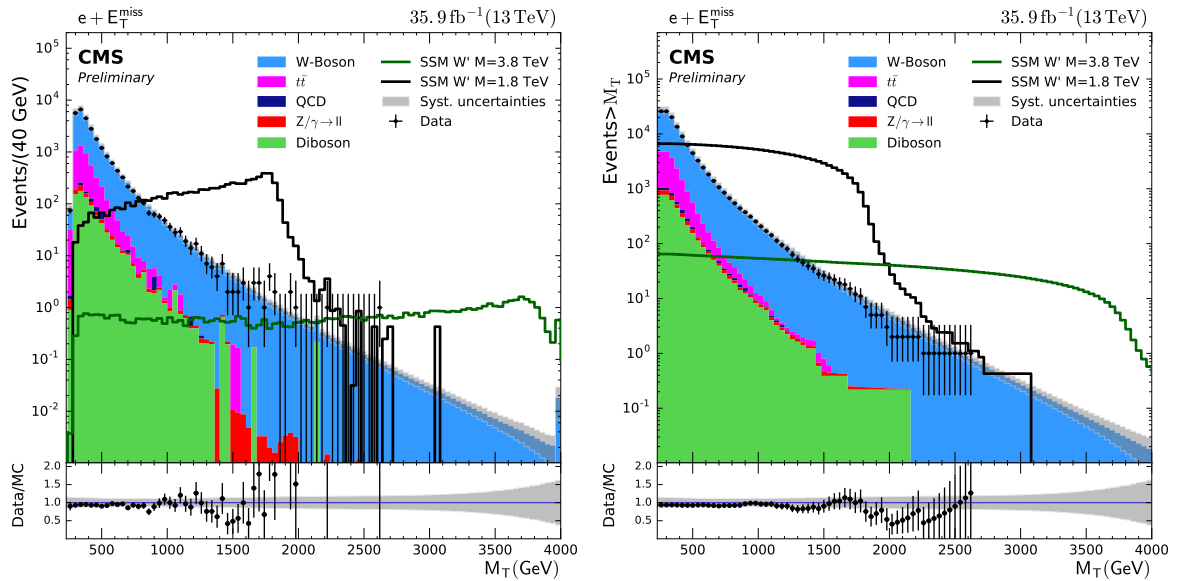

Figure 7.1.1: Final distribution of the discriminating variable M_T (left) and its cumulative version (right). No significant deviation from the predicted SM background has been found.

The features seen in the p_T and E_T^{miss} spectra propagate into the M_T spectrum as well and, as described in Section 6.6, can be explained by statistical effects. Table 7.1.1 shows the number of events in data, in the SM background and for two signal mass points for different M_T thresholds. For $M_T >1.8$ TeV a slight deficit in data compared to the standard model background prediction is observed. Due to the small number of events in data and in the SM prediction this deficit can explained by a statistical fluctuation. As for the deficit in p_T, a significance test has been performed and delivered a deviation of 1.2 σ. Over all, considering the systematic uncertainties, the predicted standard model background and the observed data are in good agreement.

Table 7.1.1: Number of events in data, background and for two signal examples above a specific M_T threshold with their absolute uncertainty. The deficit at around 2 TeV lies in a window of 1.2 standard deviations.

	$M_T >1000$ GeV	$M_T >2000$ GeV	$M_T >3000$ GeV
Data	210	2	0
SM Background	214 ± 27	4.94 ± 0.95	0.258 ± 0.089
SSM W' M=1.8 TeV	5120 ± 730	27.3 ± 5.9	0.43 ± 0.44
SSM W' M=3.8 TeV	54 ± 14	40 ± 12	24.3 ± 8.6

An event display of the highest M_T events with an M_T of 2620 ± 20 GeV can be seen in Figure 7.1.2. This event was measured in run G of 2016 and has the event number 2137541573 with the luminosity section number of 1155 and run number of 278820. Around the interaction point, the high amount of primary vertex tracks due to pile-up can be seen. The reconstructed electron track corresponding to the ECAL measurement is colored in red. Its deposition of energy in the ECAL is visualized by the following red cone. Additionally, the violet arrow indicates E_T^{miss} and its direction. The length of the arrow indicates the amount of the reconstructed E_T^{miss} in this event. The electron and the E_T^{miss} are nearly perfectly back-to-back with a $\Delta\phi$ of 3.137 and the expected p_T/E_T^{miss} signature of 1.03. One needs to keep in mind that the E_T^{miss} value in the event display is before applying the correction explained in Subsection 5.1.3. The corrected value is 1288 ± 13 GeV.

As no excess in data has been found, the final M_T distribution is used to set exclusion limits. The used approach and its results will be described in the next chapter.
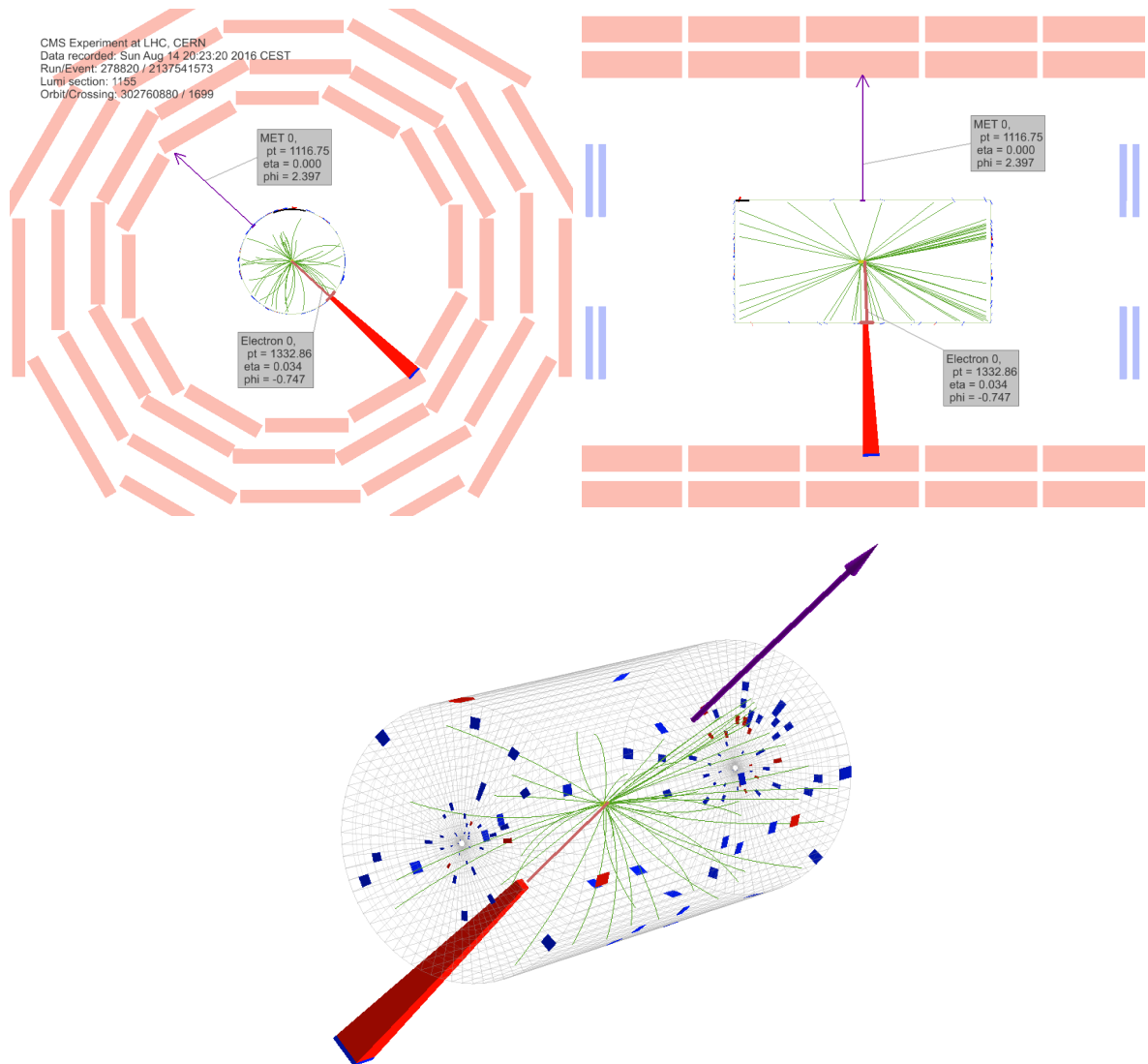
CMS Experiment at LHC, CERN
Data recorded: Sun Aug 14 20:23:20 2016 CEST
Run/Event: 278820 / 2137541573
Lumi section: 1155
Orbit/Crossing: 302760880 / 1699

MET 0,
pt = 1116.75
eta = 0.000
phi = 2.397

Electron 0,
pt = 1332.86
eta = 0.034
phi = -0.747

Figure 7.1.2: Event display of the highest M_T event of $2620 \pm 20\,\text{GeV}$ after all selection requirements are applied. The top left shows the transversal x-y-plane. At the top right, the side viewpoint on the y-z-plane is shown. On the bottom, a three dimensional view can be seen. The green lines indicate the reconstructed paths in the tracker system with the electron track pointed out in red. The red cone indicates the ECAL energy deposition of the electron and the purple arrow corresponds to the calculated E_T^{miss}.

8 Statistical Interpretation

8.1 Limit Setting

8.1.1 Bayesian Approach

In particle physics, two different statistical approaches are used. Firstly, the frequentist statistics approach interprets the probability as the frequency of the result of an experiment. The second approach is the Bayesian interpretation where the probability describes a degree of belief in the hypothesis to be true. It requires a prior probability function of the parameter of interest as an input.
Both methods are used in particle physics, ATLAS and CMS agreed on the Bayesian approach for the investigation of the SSM W' result.
The fundamental basis of this interpretation is Bayes' theorem. It connects the probabilities of two subsets A and B from a set S to describe the probability of A being true assuming that B is true:

$$P(A|B) = \frac{P(B|A)P(A)}{P(A)} \tag{8.1}$$

Applying this theorem on particle physics, one can describe the probability of the hypothesis H being true while observing a set of data $P(H|data)$ with the probability to measure this data assuming H is true $P(data|H)$, the prior degree in belief in H $\pi(H)$ and the overall probability to observe this set of data $P(data)$. $P(data)$ can be written as the integral over all possible hypothesis which leads to :

$$P(H|data) = \frac{P(data|H)\pi(H)}{\int P(data|H')\pi(H')dH'} \tag{8.2}$$

As models often depend on a set of parameters θ, it is common to set a limit on these model parameters. Limits are described conventionally in the parameter region that is excluded with a probability of 0.95, also called confidence level (CL). This means that the limit on the model parameter of H can be set with $0.95 = \int_0^{\theta_{0.95}} d\theta\, P(data|\theta)\pi(\theta)$. Usually, a Poisson function is used to describe the likelihood instead of the probability to observe a set of data under assuming the hypothesis H:

$$0.95 = \int_0^{\theta_{0.95}} d\theta\, L'(data|\theta)\, \pi(\theta) \tag{8.3}$$

with

$$L'(data|\theta) = \int d\vec{v} L_{Poisson}(data|\theta,\vec{v})\pi(\vec{v}) \tag{8.4}$$

and

$$L_{Poisson}(data|\theta,\vec{v}) = \frac{\epsilon(\theta,\vec{v})^n}{n!} e^{-\epsilon(\theta,\vec{v})} \tag{8.5}$$

Equation 8.4 introduces the nuisance parameters $\vec{v}$ that model the systematic uncertainties assuming they are log-normal distributed.

In Equation 8.5, $L_{Poisson}$ is defined by the counts of signal events n and the expected number of events from signal and background ϵ which is a function of model and nuisance parameters θ and $\vec{v}$.
Further description of the statistical method used in this analysis can be found in [27]. The calculation of the limits was carried out using the "Higgs combine tool" [103][104] which is a statistical tool based on the RooStats package [105].

8.1.2 SSM

For the exclusion limit in the SSM interpretation (Subsection 2.2.1), a multi-bin approach is used. As an input, the final M_T distribution is used with all selection criteria explained in Section 6.5 are applied. For each single bin, the likelihood function is evaluated and in the end all bins are combined, therefore the shape of the distribution is taken into account. Equation 8.4 together with Equation 8.5 becomes:

$$L'(data|\theta) = \int d\vec{v} \prod_{i \in bins} \frac{\epsilon_i(\theta, \vec{v})^{n_i}}{n_i!} e^{-\epsilon_i(\theta, \vec{v})} \times \pi(\vec{v}) \tag{8.6}$$

The parameter of interest is the cross section of the signal as a function of M_T. To translate the number of events into a limit on the cross section times branching fraction, the luminosity times acceptance times efficiency, $L \times A \times \epsilon$, is needed. The acceptance takes detector geometry effects into account whereas the signal efficiency indicates how many events pass the general and analysis specific selections described in Chapter 5 and Section 6.5. The acceptance times the signal efficiency is shown in Figure 8.1.1. It rises for higher M_T, reaching its top value at around 2.2 TeV in W′ mass. For higher masses, the it decreases again due to the rising impact of the off-shell production of the W′ (see Figure 4.2.1 in Subsection 4.2.3). The final exclusion limit

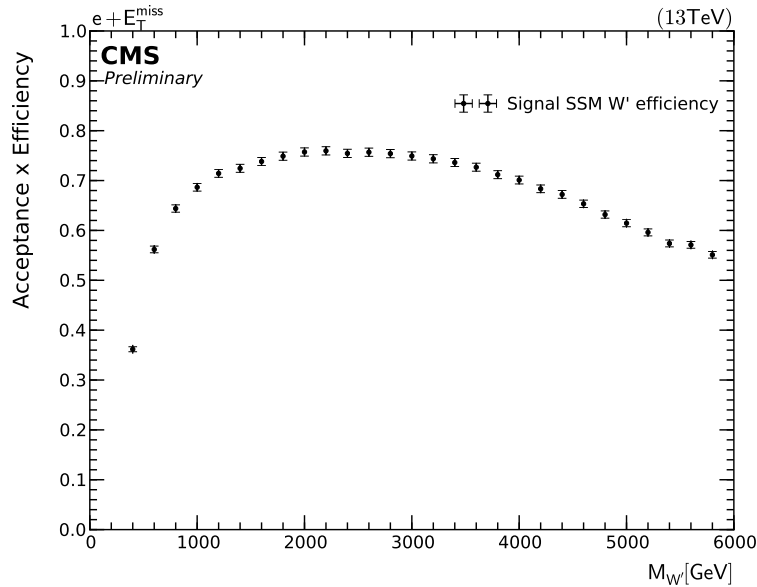Figure 8.1.1: The acceptance times signal efficiency as a function of the W′ mass.

on the cross section times branching ratio can be seen in Figure 8.1.2. It is shown as a function on the W′ mass. The dashed black line indicates the expected limit from the background simulation only, whereas the solid black line shows the observed limit taking the measured data into account. Around these lines are the green and

yellow bands that correspond to the 1 and 2 standard deviations of the expected limit respectively. Additionally, the theoretical signal cross sections are shown at NNLO with a grey band around it indicating the PDF uncertainty on the signal. To calculate the mass of the W' to which the SSM can be excluded, one needs to take the cross point between the limit and the cross section. Therefore, the observed exclusion limit for the 13 TeV data from 2016 is at 4.9 TeV. Compared to the published limit from 2015 of 3.6 TeV [7] which uses an integrated luminosity of 2.3 fb^{-1}, this is an improvement of 1.3 TeV in the W' mass.

As the limit is set in a region where no contribution from the background is expected and no event has been measured, the impact of the systematic uncertainties on the limit are small. Assuming a perfect measurement with negligible uncertainties would lead to slightly smaller values for the cross section times branching ratio limit and smaller bands around it. The change in the final exclusion limit would be negligible. The systematic uncertainties becomes important, when a discrepancy between the data and the simulation is observed. The description of the systematic uncertainties influences the calculation of the significance of a possible excess or deficit.

In [106], the exclusion limit, using the data driven method described in Section 6.3 instead of simulation, was also evaluated to be at 4.9 TeV. This shows that there is no significant difference between the usage of the data driven multijet approach or the description via Monte Carlo simulation when calculating the limit in this channel. This is an additional indicator, that QCD contribution from simulation is sufficient for this analysis.

In addition to the electron and neutrino final state, the decay into a muon or a tau lepton and a neutrino is also possible. The muonic decay channel was investigated by the authors of [106] and shows similar sensitivity with an exclusion limit of 4.9 TeV at a 95% confidence level. A combination of the muon and the electron channel provides an improved exclusion limit of 5.2 TeV.

A similar search for a new heavy vector boson has been performed by the ATLAS collaboration [107]. The exclusion limit was set at 5.2 TeV for the electron channel, 4.5 TeV for the muon channel and at 5.2 TeV for the combination of both channels. The slightly better exclusion limit for the decay into an electron and a neutrino can be due to the problems that occurred during the reconstruction of the CMS data (see Chapter 5) which can effect the sensitivity. As one of the main goals of the CMS detector is the good muon measurement performance, the exclusion limit of the muon channel is better compared to the limit provided by the ATLAS collaboration, which results in the same exclusion limit when combining both channels. The dedicated search for the decay of the W' into a tau and a neutrino provides an exclusion limit of 4.3 TeV [108]. As only the decay products of the tau lepton are measured in the detector, the reconstruction of the final state becomes more complicated which leads to a lower sensitivity compared to the other leptonic decay channels.
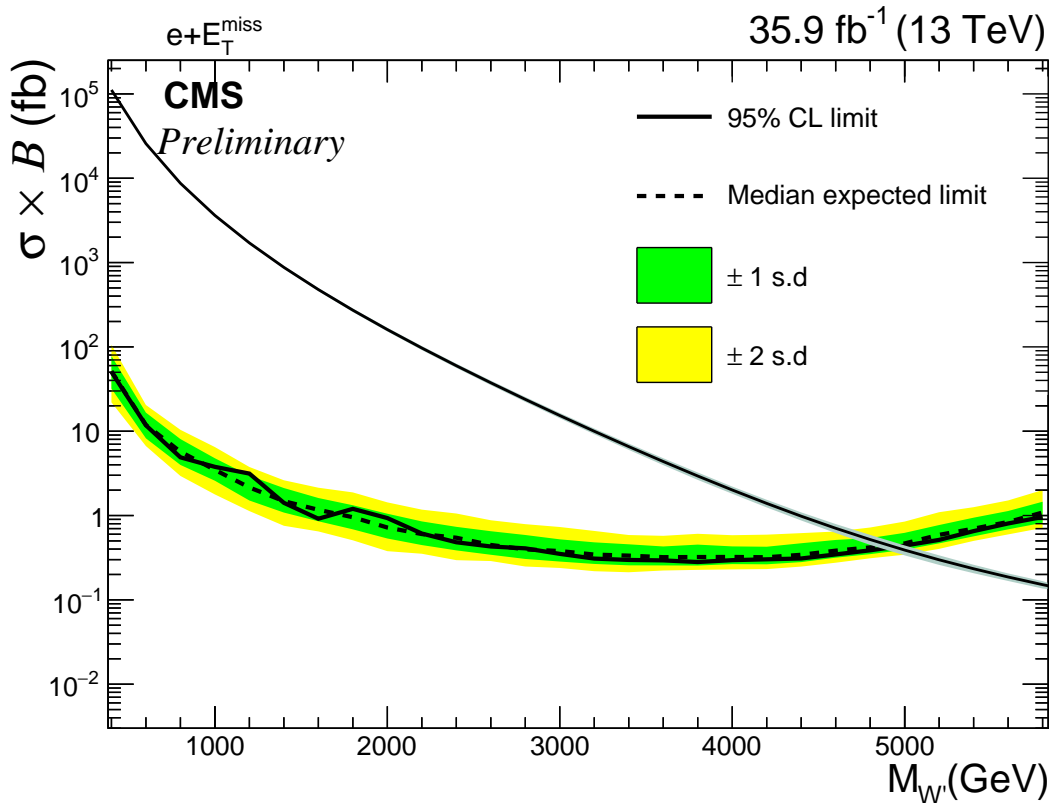
Figure 8.1.2: Calculated limit on the cross section times branching ratio as a function of the W' mass. The crossing point of the NLO cross section with the observed limit indicates the excluded mass range.

To determine the effect of the planned higher luminosity at LHC and the impact on the sensitivity, a study has been performed on simulation for integrated luminosities of 150 fb^{-1}, which is expected to be reached in 2018 at the end of Run II, and the final luminosity of 300 fb^{-1} before the upgrade to the high luminosity LHC starts when Run III ends in 2022 [109]. These predictions can be seen in Figure 8.1.3.

For the end of Run II, the expected limit on the cross section times branching ratio is 5.5 TeV which would be an improvement of 600 GeV. Compared to the increasing of 1.3 TeV from 2.3 fb^{-1} to 35.9 fb^{-1}, this shows that the exclusion limit is not expected to improve much at this big scale for higher luminosities.

Before the long shutdown 3, the expected limit is above 5.8 TeV. Therefor, more signal points with higher W' mass must be produced to be sure to cover this expected region. The systematic uncertainties are assumed to stay unchanged but it is expected that, with updating the detector, they will grow smaller. Therefore, the final measured limits on the W' mass may be even higher .
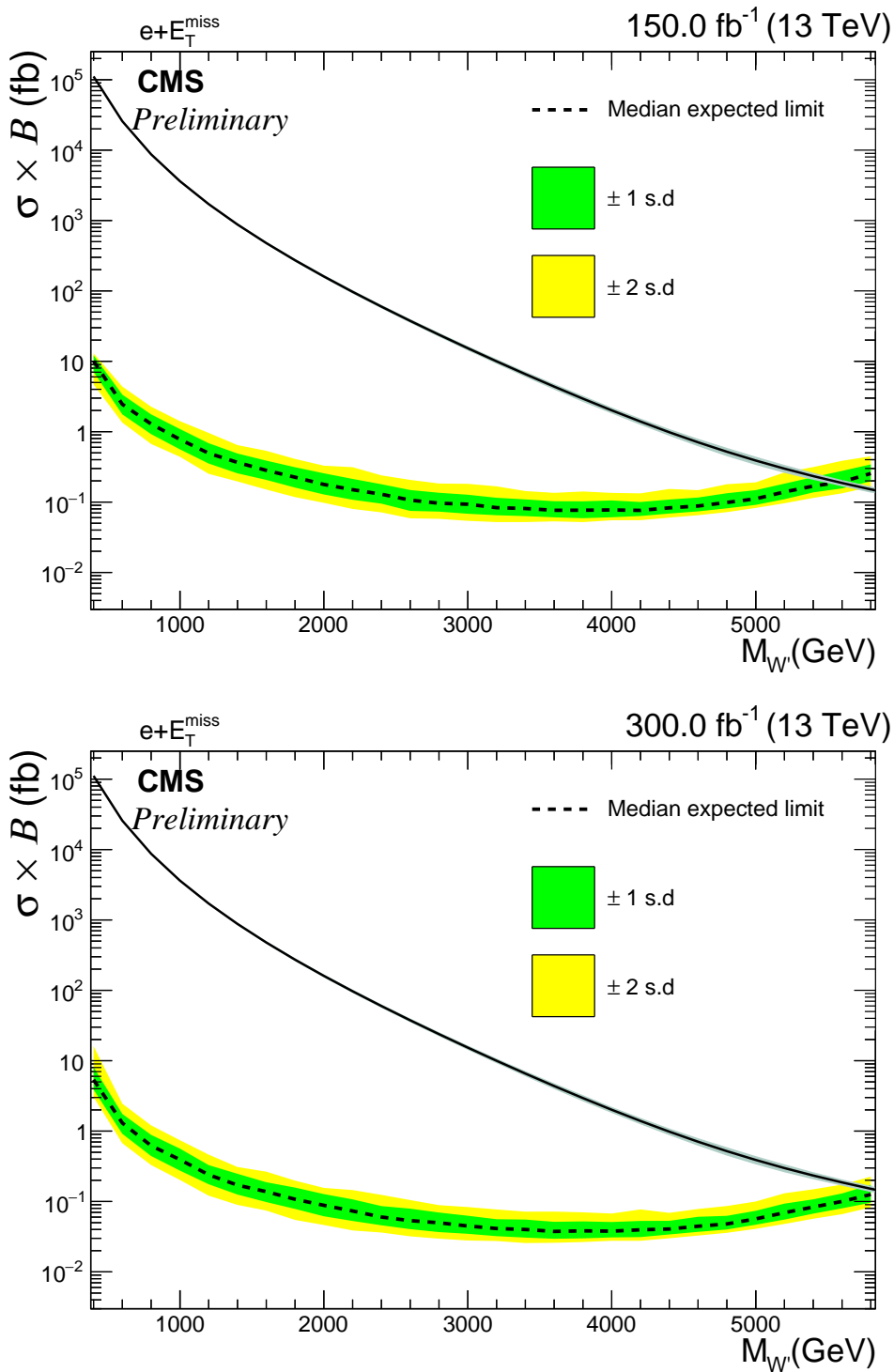
Figure 8.1.3: Expected cross section limit with L=150 fb^{-1} (top) and 300 fb^{-1} (bottom). W' masses up to 5.5 TeV are expected to be excluded when reaching the end of Run II. W' masses above 5.8 TeV are expected to be excluded when reaching the end of Run III. The relative systematic uncertainties where assumed to stay unchanged.

8.1.3 Generalized Couplings

As explained in Subsection 2.2.1, the coupling $g_{W'}$ of the W' can be set as a free parameter. Therefore, a limit on the cross section as a function of the coupling ratio can be calculated. Coupling ratios of 0.0001, 0.001, 0.01, 0.1, 1, 2, 3 and 5 have been evaluated for each produced mass point. For the first time, this analysis investigates the coupling at a mass range lower than 1 TeV with a center-of-mass energy of 13 TeV. Additionally, the fitting procedure to evaluate the crossing point of the theoretical cross section and the calculated limit has been optimized. As an example, the cross section times branching ratio limit as a function of $g_{W'}/g_W$ can be seen in Figure 8.1.4. The dashed black line indicates the expected limit from the simulation, the solid black line shows the observed limit and the green and yellow bands represent the 1 and 2 standard deviations. The blue line shows the LO theory cross section for different coupling strengths. All cross sections above the one at the crossing point with the experimental limit can be excluded. If one takes the intersection point
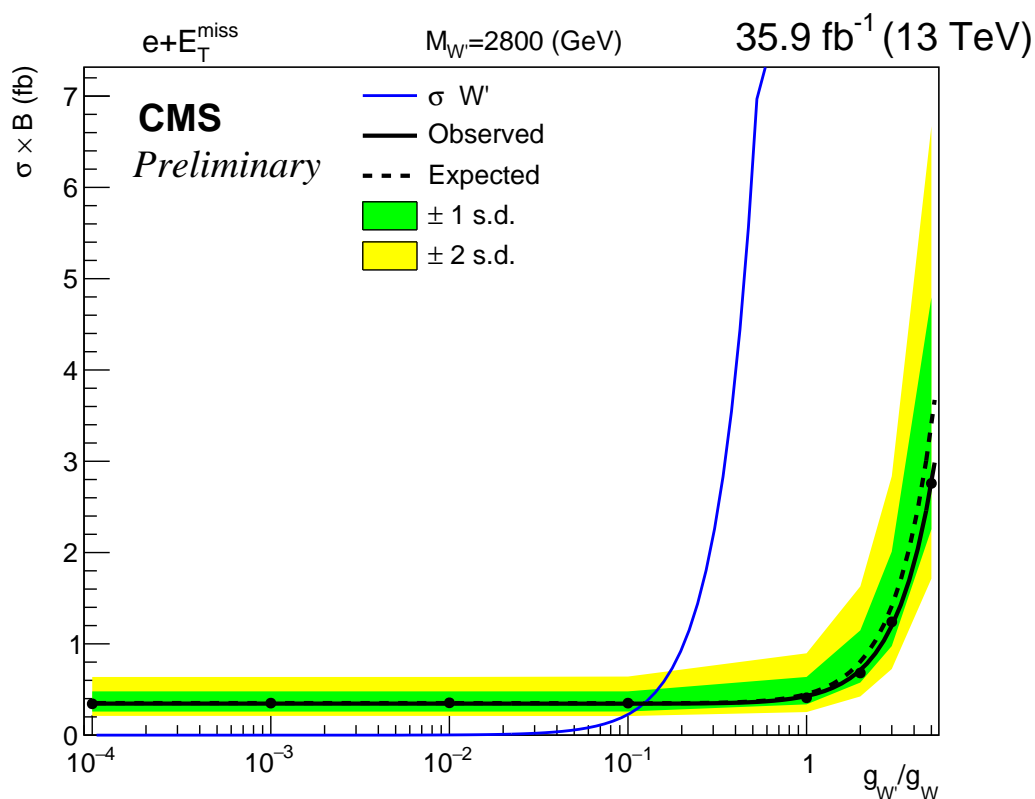

Figure 8.1.4: The limit on the cross section times branching ratio as a function of $g_{W'}/g_W$. The crossing point of the LO cross section (blue) and the observed limit (solid black) indicate the excluded cross section.

of the cross section and the limit, one can also derive the exclusion limit in the

coupling ratio-mass plane as shown in Figure 8.1.5. The style stays the same but the dot-dashed line indicates the coupling ratio of 1 which corresponds to limit on the SSM limit at LO set in Subsection 8.1.2. For each mass point in the plane, the corresponding coupling value indicates the maximal coupling strength that is not excluded. The range reaches down to the order of 10^{-2} for low masses and up to about 2 for high masses.
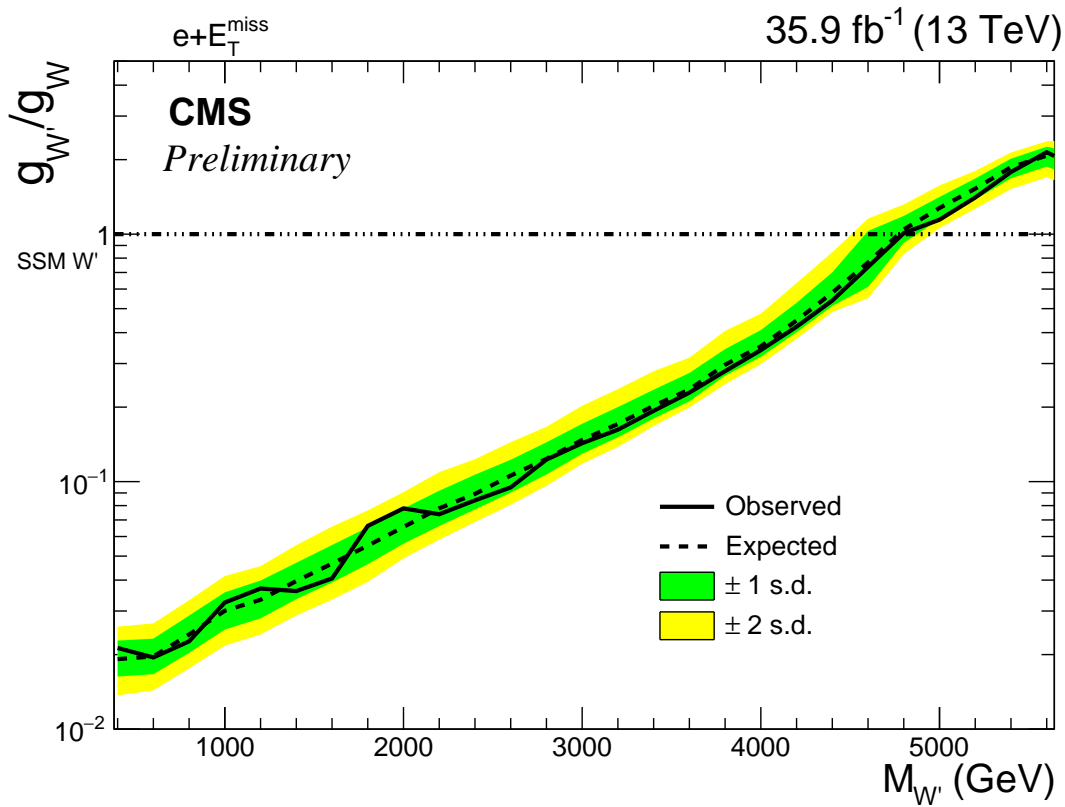

Figure 8.1.5: Coupling ratio $g_{W'}/g_W$-W' mass plane

8.1.4 Diboson Decay

Additionally to the SSM interpretation and the variation of the coupling strength, a limit on the interpretation in terms of the Heavy Vector Triplet model (Subsection 2.2.2) has been done. The procedure is the same as for the SSM with a mass range from 1 TeV up to 3 TeV in steps of 250 MeV. The acceptance times signal efficiency for the produced signal points can be seen in Figure 8.1.6. It behaves comparably to the signal efficiency of the SSM. The value starts at around 50% for 1 TeV and rises up to 75% for the W' mass of 3 TeV.
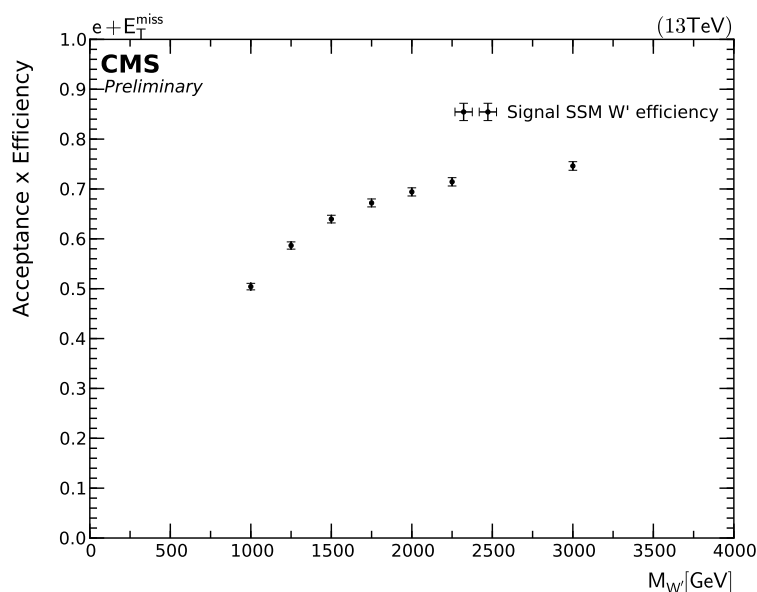

Figure 8.1.6: The acceptance times signal efficiency as a function of the W' mass for the HVT model.

The calculated limit can be seen in Figure 8.1.7. As one can see, at $\sqrt{s} = 13\,\text{TeV}$ and a luminosity of $35.9\,\text{fb}^{-1}$, this analysis is not sensitive to the investigated mass range. A study for luminosities of $150\,\text{fb}^{-1}$ and $300\,\text{fb}^{-1}$ has been carried out as it is was done for the SSM. When the end of Run II is reached, the analysis is expected to be sensitive and the expected exclusion limit lies at about $1.85\,\text{TeV}$ for $150\,\text{fb}^{-1}$. The calculated limits can be seen in Figure 8.1.8. The expected limit before the upgrade to the high-luminosity LHC begins was calculated to be at $2.35\,\text{TeV}$. This would be an improvement of $500\,\text{GeV}$ compared to double amount of collected integrated luminosity with a value of $300\,\text{fb}^{-1}$. This indicates, that the improvement coming from higher luminosity becomes less, as it was observed for the SSM limit.

There are different analyses investigating the diboson resonance [110–112]. For example, the dedicated search for massive diboson resonances [110] derived a limit

on the decay of a new heavy vector boson W′ into diboson pair with a dijet final state. The observed limit was evaluated to be at a W′ mass of 3.6 TeV. Therefore, this analysis with a final state of an electron and E_T^{miss} is not expected to deliver a comparable sensitivity as these dedicated searches.
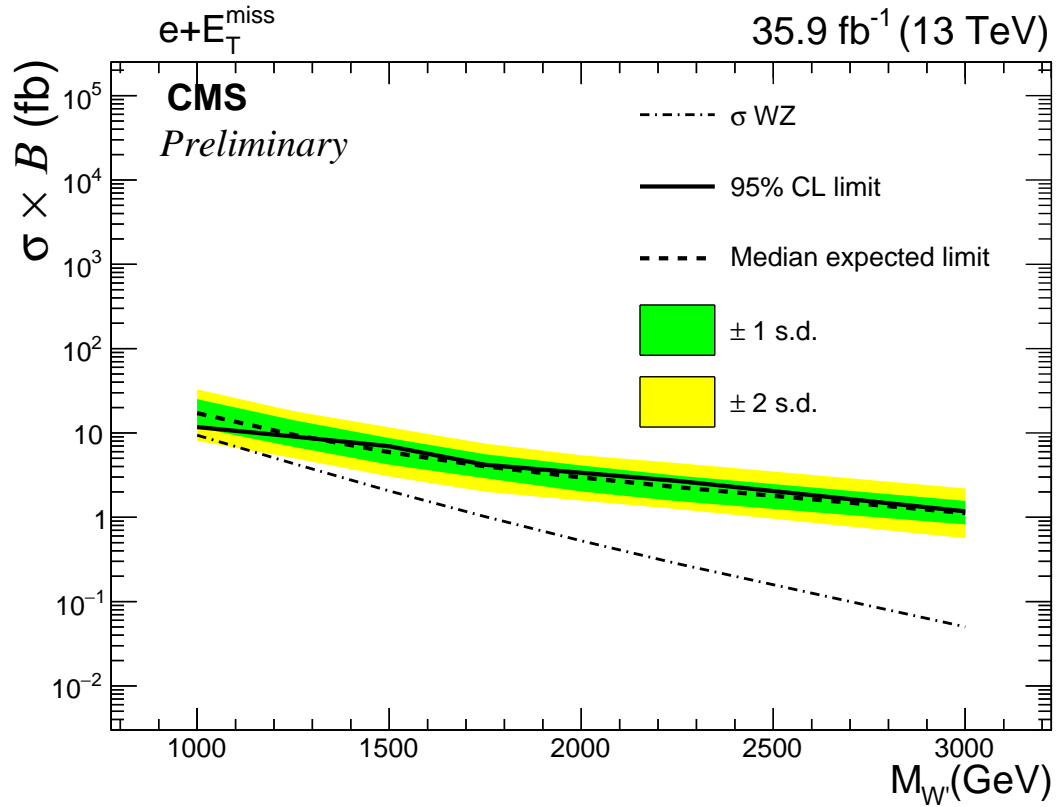
Figure 8.1.7: Calculated limit on the cross section times branching ratio as a function of the W′ mass. As the cross section does not intersect with the observed limit, this analysis is not sensitive to this decay channel in the investigated mass range.
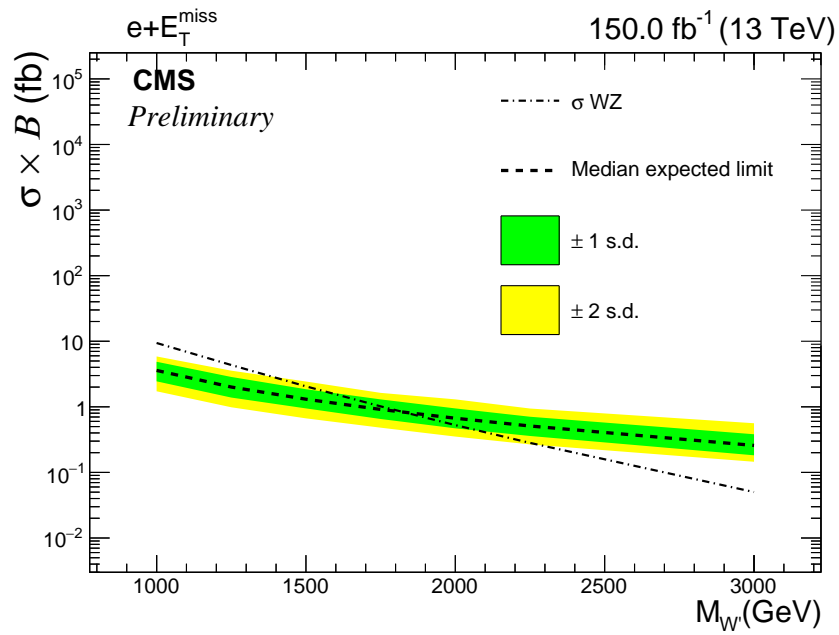
(a) Expected cross section limit with L=150 fb^{-1}. W′ masses up to 1.85 TeV are expected to be excluded when reaching the end of Run II.
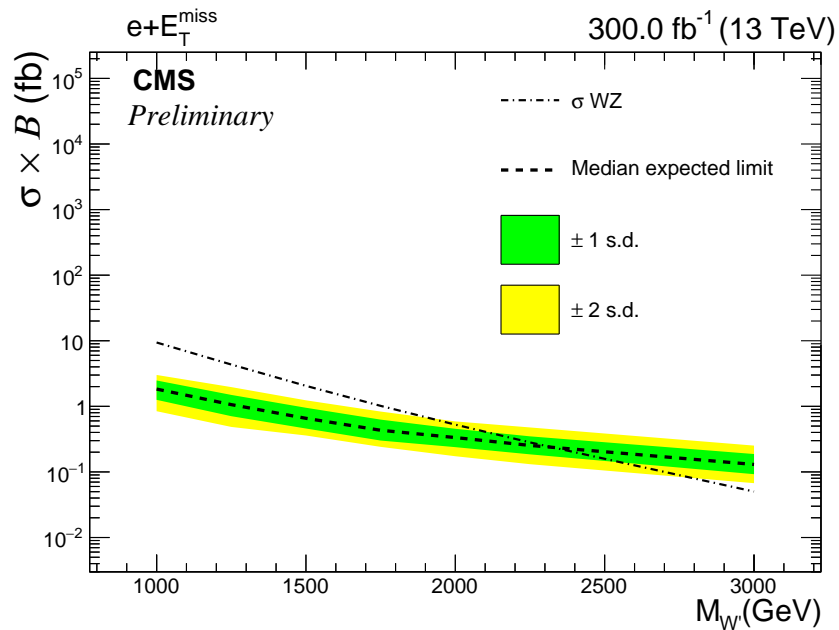
(b) Expected cross section limit with L=300 fb^{-1}. W′ masses above 2.35 TeV are expected to be excluded when reaching the end of Run III.

Figure 8.1.8: Expected cross section times branching ratio limit performed on simulation for two different integrated luminosities. The systematic uncertainties where assumed to stay unchanged.

8.1.5 Model Independent Limit

Additionally to exclusion limits using specific model interpretations, a model independent limit was calculated. It can be used to estimate the limit for theories that use similar back-to-back kinematics as in the SSM. For this purpose, a single-bin approach instead of the multibin counting is used. In this approach, the number of events is summed up into one single bin for the background estimation and the measured data for different thresholds in M_T. From this bin, a limit is calculated on the cross section times branching ratio times acceptance times efficiency ($\sigma \times \mathrm{BR} \times A \times \epsilon$) and can be seen in Figure 8.1.9. To interpret this limit in terms of a new model, one needs the acceptance times signal efficiency $A \times \epsilon$ of that model for the specific M_T threshold:

$$A \times \epsilon(M_{T,min}) = \frac{N_{M_T > M_{T,min}}}{N_{total}} \tag{8.7}$$

$N_{M_T > M_{T,min}}$ is the number of all signal events above the threshold $M_{T,min}$ and N_{total} is the number of all events. Applying this signal efficiency, the excluded cross section can be evaluated to:

$$\sigma_{model}\left(M_T > M_{T,min}\right) = \sigma_{total} \cdot A \times \epsilon(M_{T,min}) > \sigma_{MI}(M_{T,min}) \tag{8.8}$$

Steps in the derived limit are directly connected to the number of data events above the specific M_T threshold. As seen in Section 7.1, the highest M_T event is at 2.6 TeV, where the model independent limit becomes flat at 0.13 fb. Table 8.1.1 shows the calculated numbers of the model independent limit. The upper and lower case values indicate the one sigma band. As a sanity test, one can use the efficiency of the $W' = 3800$ GeV signal sample above the M_T threshold of 2 TeV, which is $\epsilon \approx 0.624$. Using the value from Table 8.1.1 for 2 TeV of $0.28^{+0.38}_{-0.19}$ fb with Equation 8.8 the expected limit for a W' boson with the mass of 3.8 TeV is $0.45^{+0.61}_{-0.30}$ fb. The expected limit for this mass point calculated in Subsection 8.1.2 is $0.32^{+0.45}_{-0.26}$ fb. Considering, that the limit calculated from the model independent limit does not have the specific information about the signal, e.g. shape and actual event rates, and taking the sigma bands into account, the values are in good agreement.
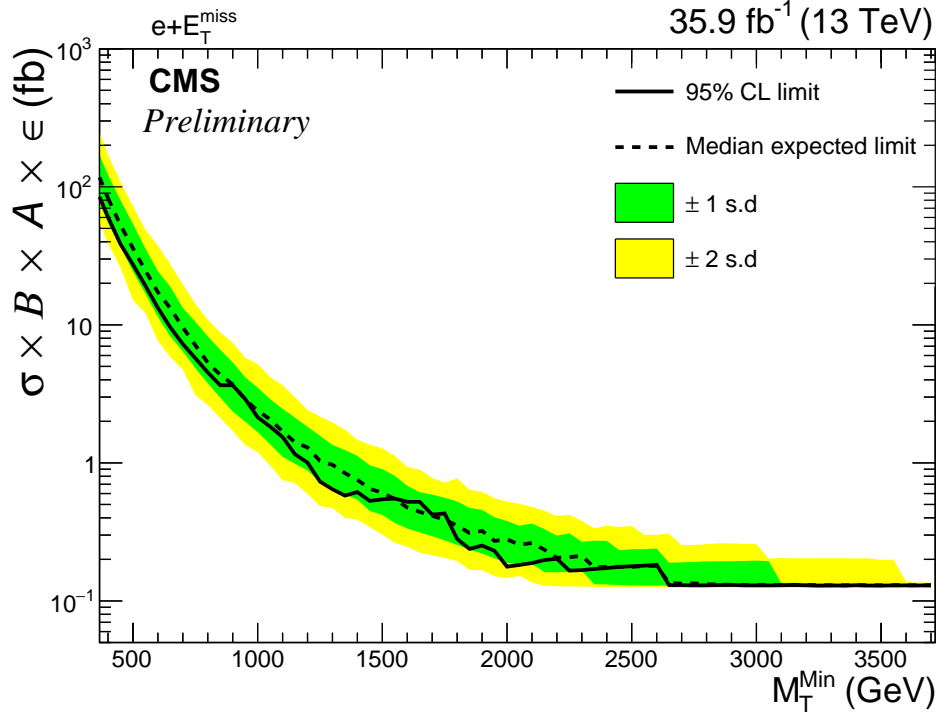
Figure 8.1.9: The acceptance times signal efficiency as a function of the W′ mass.

Table 8.1.1: Number of the calculated model independent expected (Exp.) and observed (Obs.) limit for different M_T thresholds. The upper and lower case numbers indicate the standard deviation of the expected limit.

M_T^{min} (GeV)		300	400	500	600	700	800
Exp.	(fb)	211^{+118}_{-72}	$82.7^{+39.3}_{-28.2}$	$35.9^{+18.0}_{-11.6}$	$17.2^{+7.24}_{-5.82}$	$9.59^{+3.72}_{-3.15}$	$5.33^{+2.94}_{-1.56}$
Obs.	(fb)	158.5	60.55	27.36	13.28	7.26	4.53
M_T^{min} (GeV)		900	1000	1100	1200	1300	1400
Exp.	(fb)	$3.70^{+1.66}_{-1.35}$	$2.39^{+1.13}_{-0.72}$	$1.69^{+0.78}_{-0.58}$	$1.29^{+0.54}_{-0.41}$	$0.97^{+0.38}_{-0.30}$	$0.75^{+0.37}_{-0.21}$
Obs.	(fb)	3.65	2.14	1.54	1.01	0.64	0.61
M_T^{min} (GeV)		1500	1600	1700	1800	1900	2000
Exp.	(fb)	$0.61^{+0.29}_{-0.19}$	$0.47^{+0.21}_{-0.14}$	$0.41^{+0.18}_{-0.12}$	$0.35^{+0.18}_{-0.10}$	$0.32^{+0.13}_{-0.10}$	$0.28^{+0.10}_{-0.09}$
Obs.	(fb)	0.54	0.52	0.42	0.28	0.25	0.18
M_T^{min} (GeV)		2100	2200	2300	2400	2500	2600
Exp.	(fb)	$0.26^{+0.10}_{-0.08}$	$0.21^{+0.09}_{-0.04}$	$0.21^{+0.06}_{-0.05}$	$0.18^{+0.10}_{-0.05}$	$0.18^{+0.06}_{-0.05}$	$0.18^{+0.06}_{-0.05}$
Obs.	(fb)	0.19	0.20	0.17	0.17	0.18	0.18
M_T^{min} (GeV)		2700	2800	2900	3000	3100	3200
Exp.	(fb)	$0.14^{+0.06}_{-0.01}$	$0.13^{+0.06}_{-0.01}$	$0.13^{+0.06}_{-0.01}$	$0.13^{+0.07}_{-0.01}$	$0.131^{+0.005}_{-0.003}$	$0.130^{+0.004}_{-0.003}$
Obs.	(fb)	0.13	0.13	0.13	0.13	0.13	0.13

9 Conclusion and Outlook

A search for new physics in the e + E_T^{miss} final state has been performed. The dataset from 2016 provided by the CMS delivered an integrated luminosity of $35.9\,\text{fb}^{-1}$, which is the biggest dataset that has ever been taken to date. A validation of the QCD description by Monte Carlo simulation has been carried out using a data-driven method. As the Monte Carlo delivers a comparable shape and statistics the MC simulation based contribution from QCD has been chosen.

As no significant deviation from the SM prediction has been observed, exclusion limits have been set. In the matter of a SSM W', masses up to $4.9\,\text{TeV}$ can be excluded in a confidence level of 95%. Compared to the 2015 result of $3.6\,\text{TeV}$, this is an improvement of $1.3\,\text{TeV}$. A comparison to the limit derived using the data-driven approach [106] shows no difference in the final value which supports the outcome of the QCD MC validation.

As an extension, the coupling $g_{W'}$ of the W' was used as a free parameter and limits on the generalized coupling ratio $\frac{g_{W'}}{g_W}$ have been derived. The range of the excluded coupling ratio reaches from 10^{-2} for low masses up to about 2 for high masses of the W'. Additionally, the interpretation of the Heavy Vector Triplets model as an W' decaying into WZ has been investigated and no sensitivity in the mass range of $1\,\text{TeV}$ to $3\,\text{TeV}$ for this integrated luminosity have been found.

The final state of an electron and E_T^{miss} has also been used to derive model independent limits which can be applied on models that show similar back-to-back kinematics. The range of the MI limit reaches from 238 to $0.13\,\text{fb}$. The cross check with the SSM limit shows good agreement of the calculated values. To get an idea what can be expected in future runs of the LHC, an extrapolation to the luminosities of $150\,\text{fb}^{-1}$ and $300\,\text{fb}^{-1}$ has been performed. These luminosities correspond to the expected statistics taken at the end of Run II in 2018 and before starting the upgrade to the High-Luminosity LHC in 2022. The expected exclusion limit for the SSM W' at $150\,\text{fb}^{-1}$ is $M_{W'} = 5.5\,\text{TeV}$ which would be an improvement to 2016 of $600\,\text{GeV}$. The expected exclusion limit for the diboson interpretation lies at about $M_{W'} = 1.85\,\text{TeV}$ for the end of Run II and at $M_{W'} = 2.35\,\text{TeV}$ after Run III. For the SSM W', the mass range is expected to be not sufficient anymore and additional signal samples with mass points greater than $5.8\,\text{TeV}$ need to be produced.

This thesis reached nearly the maximum sensitivity of the SSM interpretation for the electron plus E_T^{miss} final state for the LHC at $\sqrt{s} = 13\,\text{TeV}$. Further investigations in terms of the SSM with higher statistics will not improve the exclusion limit significantly. Nevertheless, the investigation of this final state is still important to understand object properties and to find possible misconstruction effects. Additionally,

other interpretations like the production of dark matter [113] might provide improving sensitivity for higher luminosity and should be considered in new iterations of this analysis.

10 Appendix

10.1 Cross Section Tables

Table 10.1.1: Signal production cross sections (at LO and NNLO) times branching fraction, as well as the k-factor, for SSM W′ bosons decaying to electron plus neutrino, at $\sqrt{s} = 13\,\text{TeV}$.

$W'mass\,[TeV]$	$\sigma_{\text{LO}}x\mathcal{B}$ (fb)	$\sigma_{\text{NNLO}}x\mathcal{B}$ (fb)	k-factor
0.4	84153	111394	1.324
0.6	19225	25718	1.338
0.8	6494	8717	1.342
1.0	2699.0	3623.5	1.343
1.2	1275.8	1708.9	1.340
1.4	657.28	877.23	1.335
1.6	360.15	478.18	1.328
1.8	206.47	272.38	1.319
2.0	122.55	160.43	1.309
2.2	74.726	96.957	1.298
2.4	46.584	59.813	1.284
2.6	29.560	37.510	1.269
2.8	19.035	23.852	1.253
3.0	12.412	15.348	1.237
3.2	8.1952	9.9844	1.218
3.4	5.4675	6.5682	1.201
3.6	3.6865	4.3708	1.186
3.8	2.5158	2.9432	1.170
4.0	1.7337	2.0092	1.159
4.2	1.2108	1.3926	1.150
4.4	8.5649×10^{-1}	9.8188×10^{-1}	1.146
4.6	6.1476×10^{-1}	7.0621×10^{-1}	1.149
4.8	4.4871×10^{-1}	5.1886×10^{-1}	1.156
5.0	3.3227×10^{-1}	3.8928×10^{-1}	1.172
5.2	2.5146×10^{-1}	2.9832×10^{-1}	1.186
5.4	1.9300×10^{-1}	2.3371×10^{-1}	1.211
5.6	1.5128×10^{-1}	1.8659×10^{-1}	1.233
5.8	1.2029×10^{-1}	1.5148×10^{-1}	1.259

Table 10.1.2: Analyzed simulated samples for several background processes (L=e, μ, τ), generator used and the order of cross sections times branching fractions.

	Background	Generator	Order of σ (pb)	σ (pb)
W	WJetsToLNu	Madgraph	NNLO	61526.7
	WJetsToLNu HT-100To200	Madgraph	NLO	1627.45
	WJetsToLNu HT-200To400	Madgraph	NLO	435.237
	WJetsToLNu HT-400To600	Madgraph	NLO	59.1811
	WJetsToLNu HT-600To800	Madgraph	NLO	14.5805
	WJetsToLNu HT-800To1200	Madgraph	NLO	6.65621
	WJetsToLNu HT-1200To2500	Madgraph	NLO	1.60809
	WJetsToLNu HT-2500ToInf	Madgraph	NLO	0.0389136
W off-shell	WToLNu M-100 13TeV	Pythia 8	LO	163.15
	WToLNu M-200	Pythia 8	LO	6.236
	WToLNu M-500	Pythia 8	LO	0.2138
	WToLNu M-1000	Pythia 8	LO	0.01281
	WToLNu M-2000	Pythia 8	LO	5.56e-04
	WToLNu M-3000	Pythia 8	LO	2.904e-05
	WToLNu M-4000	Pythia 8	LO	3.31e-06
	WToLNu M-5000	Pythia 8	LO	2.7e-07
	WToLNu M-6000	Pythia 8	LO	1.5e-08
$t\bar{t}$	single top s-channel 4f leptonDecays	aMC@NLO	NLO	3.36
	single top tW antitop 5f inclusiveDecays	PowHeg	NNLO	35.85
	single top tW top 5f inclusiveDecays	PowHeg	NNLO	35.85
	TTbar	PowHeg	NNLO	831.76
Drell Yan	DYJetsToLL M-10to50	aMC@NLO	NLO	18610
	DYJetsToLL M-50_HT-100to200	Madgraph	NLO	181.30
	DYJetsToLL M-50_HT-200to400	Madgraph	NLO	50.42
	DYJetsToLL M-50_HT-400to600	Madgraph	NLO	6.984
	DYJetsToLL M-50_HT-600to800	Madgraph	NLO	1.681
	DYJetsToLL M-50_HT-800to1200	Madgraph	NLO	0.7754
	DYJetsToLL M-50_HT-1200to2500	Madgraph	NLO	0.1862
	DYJetsToLL M-50_HT-2500toInf	Madgraph	NLO	0.0044
	DYJetsToLL M-100to200	aMC@NLO	NLO	226
	DYJetsToLL M-200to400	aMC@NLO	NLO	7.67
	DYJetsToLL M-400to500	aMC@NLO	NLO	0.423
	DYJetsToLL M-500to700	aMC@NLO	NLO	0.24
	DYJetsToLL M-700to800	aMC@NLO	NLO	0.035
	DYJetsToLL M-800to1000	aMC@NLO	NLO	0.03
	DYJetsToLL M-1000to1500	aMC@NLO	NLO	0.016
	DYJetsToLL M-1500to2000	aMC@NLO	NLO	0.002
	DYJetsToLL M-2000to3000	aMC@NLO	NLO	0.00054
QCD	QCD_Pt_50to80	Pythia 8	LO	19204300
	QCD_Pt_80to120	Pythia 8	LO	2762530
	QCD_Pt_120to170	Pythia 8	LO	471100
	QCD_Pt_170to300	Pythia 8	LO	117276
	QCD_Pt_300to470	Pythia 8	LO	7823
	QCD_Pt_470to600	Pythia 8	LO	648.2
	QCD_Pt_600to800	Pythia 8	LO	186.9
	QCD_Pt_800to1000	Pythia 8	LO	32.293
	QCD_Pt_1000to1400	Pythia 8	LO	9.4183
	QCD_Pt_1400to1800	Pythia 8	LO	0.84265
	QCD_Pt_1800to2400	Pythia 8	LO	0.11494
	QCD_Pt_2400to3200	Pythia 8	LO	0.00683
Diboson	WWToLNuQQ	Powheg	NNLO	49.997
	WWTo4Q	Powheg	NNLO	51.723
	WWTo2L2Nu	Powheg	NNLO	12.178
	WZ 13TeV	Pythia 8	NLO	47.13
	ZZ 13TeV	Pythia 8	NLO	23.23

Table 10.1.3: Signal production cross sections (at LO) times branching fraction for the Heavy Vector Triplets interpretation.

$M'_W[TeV]$	$\sigma_{LO}x\mathcal{B}$ (fb)
1.0	9407.0
1.25	4341.0
1.5	2053.0
1.75	1017.0
2.0	526.4
2.25	282.0
3.0	50.19

10.2   Trigger Scale Factors

Table 10.2.1: Trigger Scale Factors for the single electron trigger only (Type1) and the combination of the single electron and single photon trigger (Type2) with their uncertainties. They are divided into the barrel (EB) and the endcap (EE) regions. ϵ indicates the trigger efficiency. (Taken from [66])

electron p_T (GeV)	η	HLT Type	MC ϵ	Data ϵ	SF(Data/MC)
130 − 140	EB	Type1	0.965 ± 0.0046	0.956 ± 0.0025	0.991 ± 0.0040
130 − 140	EB	Type2	0.965 ± 0.0046	0.956 ± 0.0025	0.991 ± 0.0040
140 − 150	EB	Type1	0.974 ± 0.0039	0.954 ± 0.0029	0.980 ± 0.0027
140 − 150	EB	Type2	0.974 ± 0.0039	0.955 ± 0.0029	0.980 ± 0.0027
150 − 200	EB	Type1	0.978 ± 0.0018	0.960 ± 0.0017	0.983 ± 0.0006
150 − 200	EB	Type2	0.985 ± 0.0012	0.971 ± 0.0014	0.985 ± 0.0008
200 − 300	EB	Type1	0.972 ± 0.0036	0.955 ± 0.0027	0.982 ± 0.0024
200 − 300	EB	Type2	0.997 ± 0.0004	0.992 ± 0.0011	0.996 ± 0.0011
300 − 400	EB	Type1	0.942 ± 0.0187	0.947 ± 0.0073	1.006 ± 0.0184
300 − 400	EB	Type2	0.983 ± 0.0119	0.995 ± 0.0024	1.012 ± 0.0121
400 − 500	EB	Type1	0.970 ± 0.0048	0.888 ± 0.0196	0.916 ± 0.0179
400 − 500	EB	Type2	0.999 ± 0.0008	0.988 ± 0.0066	0.990 ± 0.0065
500 − 800	EB	Type1	0.979 ± 0.0048	0.821 ± 0.0373	0.839 ± 0.0310
500 − 800	EB	Type2	1.000 ± 0.0007	0.972 ± 0.0161	0.972 ± 0.0156
800 − 2000	EB	Type1	0.969 ± 0.0199	0.571 ± 0.1323	0.590 ± 0.0566
800 − 2000	EB	Type2	1.000 ± 0.0002	0.857 ± 0.0935	0.857 ± 0.0791
electron p_T (GeV)	η	HLT Type	MC ϵ	Data ϵ	SF(Data/MC)
130 − 140	EE	Type1	0.992 ± 0.0048	0.975 ± 0.0035	0.984 ± 0.0032
130 − 140	EE	Type2	0.992 ± 0.0048	0.975 ± 0.0035	0.984 ± 0.0032
140 − 150	EE	Type1	0.995 ± 0.0010	0.987 ± 0.0028	0.993 ± 0.0026
140 − 150	EE	Type2	0.995 ± 0.0010	0.988 ± 0.0028	0.993 ± 0.0026
150 − 200	EE	Type1	0.993 ± 0.0008	0.989 ± 0.0017	0.996 ± 0.0015
150 − 200	EE	Type2	0.994 ± 0.0007	0.991 ± 0.0015	0.997 ± 0.0014
200 − 300	EE	Type1	0.990 ± 0.0015	0.990 ± 0.0023	1.000 ± 0.0018
200 − 300	EE	Type2	0.994 ± 0.0013	0.998 ± 0.0009	1.004 ± 0.0009
300 − 400	EE	Type1	0.996 ± 0.0019	0.993 ± 0.0053	0.997 ± 0.0049
300 − 400	EE	Type2	0.998 ± 0.0016	1.000 ± 0.0008	1.002 ± 0.0016
400 − 500	EE	Type1	0.989 ± 0.0061	0.953 ± 0.0264	0.963 ± 0.0250
400 − 500	EE	Type2	0.999 ± 0.0007	1.000 ± 0.0008	1.001 ± 0.0007
500 − 800	EE	Type1	0.996 ± 0.0026	0.944 ± 0.0382	0.949 ± 0.0362
500 − 800	EE	Type2	1.000 ± 0.0012	1.000 ± 0.0008	1.000 ± 0.0014

Bibliography

[1] Thomson, J. Cathode Rays. *Philosophical Magazine* 90, sup1 (2010), 25–29. DOI: 10.1080/14786431003659214. URL: https://doi.org/10.1080/14786431003659214.

[2] Planck, M. Ueber das Gesetz der Energieverteilung im Normalspectrum. *Annalen der Physik* 309, 3 (1901), 553–563. ISSN: 1521-3889. DOI: 10.1002/andp.19013090310. URL: http://dx.doi.org/10.1002/andp.19013090310.

[3] *Discovery Potential of $W' \to ev$ at CMS*. Tech. rep. CMS-PAS-EXO-08-004. Geneva: CERN, July 2008. URL: https://cds.cern.ch/record/1152571.

[4] Chatrchyan, S., ET AL. Search for leptonic decays of W' bosons in pp collisions at $\sqrt{s} = 7$ TeV. *JHEP* 08 (2012), 023. DOI: 10.1007/JHEP08(2012)023. arXiv: 1204.4764 [hep-ex].

[5] Khachatryan, V., ET AL. Search for physics beyond the standard model in final states with a lepton and missing transverse energy in proton-proton collisions at sqrt(s) = 8 TeV. *Phys. Rev.* D91, 9 (2015), 092005. DOI: 10.1103/PhysRevD.91.092005. arXiv: 1408.2745 [hep-ex].

[6] Khachatryan, V., ET AL. Search for a heavy gauge boson W' in the final state with an electron and large missing transverse energy in pp collisions at $\sqrt{s} = 7$ TeV. *Phys. Lett.* B698 (2011), 21–39. DOI: 10.1016/j.physletb.2011.02.048. arXiv: 1012.5945 [hep-ex].

[7] Search for heavy gauge W' bosons in events with an energetic lepton and large missing transverse momentum at $\sqrt{s} = 13$ TeV. *Physics Letters B* 770 (2017), 278–301. ISSN: 0370-2693. DOI: https://doi.org/10.1016/j.physletb.2017.04.043. URL: http://www.sciencedirect.com/science/article/pii/S0370269317303179.

[8] Griffiths, D. J. *Introduction to elementary particles*. 2., rev. ed., 5. reprint. Physics textbook. OCLC: 711866653. Wiley-VCH, Weinheim, 2011. 454 pp. ISBN: 978-3-527-40601-2.

[9] Fließbach, T. *Allgemeine Relativitätstheorie*. 6. Aufl. OCLC: 810253278. Springer Spektrum, Berlin, 2012. 381 pp. ISBN: 978-3-8274-3032-8 978-3-8274-3031-1.

[10] Patrignani, C., ET AL. Review of Particle Physics. *Chin. Phys.* C40, 10 (2016), 100001. DOI: 10.1088/1674-1137/40/10/100001.

[11]   The CMS collaboration Observation of a new boson at a mass of 125 GeV with the CMS experiment at the LHC. *Physics Letters B* 716, 1 (Sept. 2012), 30–61. ISSN: 03702693. DOI: `10.1016/j.physletb.2012.08.021`. URL: `http://linkinghub.elsevier.com/retrieve/pii/S0370269312008581` (visited on 01/15/2018).

[12]   The ATLAS collaboration Observation of a new particle in the search for the Standard Model Higgs boson with the ATLAS detector at the LHC. *Physics Letters B* 716, 1 (2012), 1–29. ISSN: 0370-2693. DOI: `https://doi.org/10.1016/j.physletb.2012.08.020`. URL: `http://www.sciencedirect.com/science/article/pii/S037026931200857X`.

[13]   The ATLAS collaboration and CMS collaboration Measurements of the Higgs boson production and decay rates and constraints on its couplings from a combined ATLAS and CMS analysis of the LHC pp collision data at *sqrts =7* and 8 TeV. *Journal of High Energy Physics* 2016, 8 (Aug. 2016). ISSN: 1029-8479. DOI: `10.1007/JHEP08(2016)045`. URL: `http://link.springer.com/10.1007/JHEP08(2016)045` (visited on 01/15/2018).

[14]   Aaij, R., ET AL. Observation of J / Ψ p Resonances Consistent with Pentaquark States in Λ b 0 → J / Ψ K - p Decays. *Physical Review Letters* 115, 7 (Aug. 12, 2015). ISSN: 0031-9007, 1079-7114. DOI: `10.1103/PhysRevLett.115.072001`. URL: `http://link.aps.org/doi/10.1103/PhysRevLett.115.072001`.

[15]   Glashow, S. L. The renormalizability of vector meson interactions. *Nuclear Physics* 10 (1959), 107–117. ISSN: 0029-5582. DOI: `https://doi.org/10.1016/0029-5582(59)90196-8`. URL: `http://www.sciencedirect.com/science/article/pii/0029558259901968`.

[16]   Weinberg, S. A Model of Leptons. *Phys. Rev. Lett.* 19 (21 Nov. 1967), 1264–1266. DOI: `10.1103/PhysRevLett.19.1264`. URL: `https://link.aps.org/doi/10.1103/PhysRevLett.19.1264`.

[17]   Salam, A., AND Ward, J. C. Weak and electromagnetic interactions. *Il Nuovo Cimento (1955-1965)* 11, 4 (Feb. 1959), 568–577. ISSN: 1827-6121. DOI: `10.1007/BF02726525`. URL: `https://doi.org/10.1007/BF02726525`.

[18]   Englert, F., AND Brout, R. Broken Symmetry and the Mass of Gauge Vector Mesons. *Phys. Rev. Lett.* 13 (9 Aug. 1964), 321–323. DOI: `10.1103/PhysRevLett.13.321`. URL: `https://link.aps.org/doi/10.1103/PhysRevLett.13.321`.

[19]   Higgs, P. W. Broken Symmetries and the Masses of Gauge Bosons. *Phys. Rev. Lett.* 13 (16 Oct. 1964), 508–509. DOI: `10.1103/PhysRevLett.13.508`. URL: `https://link.aps.org/doi/10.1103/PhysRevLett.13.508`.

[20]   Guralnik, G. S., ET AL. Global Conservation Laws and Massless Particles. *Phys. Rev. Lett.* 13 (20 Nov. 1964), 585–587. DOI: `10.1103/PhysRevLett.13.585`. URL: `https://link.aps.org/doi/10.1103/PhysRevLett.13.585`.

[21] *The 2013 Nobel Prize in Physics - Press Release.* URL: `https://www.nobelp rize.org/nobel_prizes/physics/laureates/2013/press.html` (visited on 01/16/2018).

[22] Fukuda, Y., ET AL. Evidence for Oscillation of Atmospheric Neutrinos. *Phys. Rev. Lett.* 81 (8 Aug. 1998), 1562–1567. DOI: `10.1103/PhysRevLett.81. 1562`. URL: `https://link.aps.org/doi/10.1103/PhysRevLett.81. 1562`.

[23] Fukuda, S., ET AL. Tau Neutrinos Favored over Sterile Neutrinos in Atmospheric Muon Neutrino Oscillations. *Physical Review Letters* 85 (Nov. 2000), 3999–4003. DOI: `10.1103/PhysRevLett.85.3999`. eprint: `hep-ex/ 0009001`.

[24] Bertone, G., ET AL. Particle dark matter: evidence, candidates and constraints. *Physics Reports* 405, 5 (Jan. 2005), 279–390. ISSN: 03701573. DOI: `10.1016/ j.physrep.2004.08.031`. URL: `http://linkinghub.elsevier.com/ retrieve/pii/S0370157304003515` (visited on 10/17/2015).

[25] Martin, S. P. A Supersymmetry primer (2011). arXiv: `hep-ph/9709356 [hep-ph]`.

[26] Altarelli, G., ET AL. Searching for new heavy vector bosons in $p\bar{p}$ colliders. *Zeitschrift für Physik C Particles and Fields* 47, 4 (Dec. 1, 1990), 676–676. ISSN: 0170-9739, 1431-5858. DOI: `10.1007/BF01552335`. URL: `https://link. springer.com/article/10.1007/BF01552335`.

[27] Olschewski, M. Search for new physics in proton-proton collision events with a lepton and missing transverse energy. Veröffentlicht auf dem Publikationsserver der RWTH Aachen University. Dissertation. RWTH Aachen University, 2016. URL: `http://publications.rwth-aachen.de/record/572409`.

[28] Sullivan, Z. Fully differential W' production and decay at next-to-leading order in QCD. *Phys. Rev.* D66 (2002), 075011. DOI: `10.1103/PhysRevD.66. 075011`. arXiv: `hep-ph/0207290 [hep-ph]`.

[29] Boos, E., ET AL. Interference between W' and W in single-top quark production processes. *Phys. Lett.* B655 (2007), 245–250. DOI: `10.1016/j.physletb. 2007.03.064`. arXiv: `hep-ph/0610080 [hep-ph]`.

[30] Accomando, E., ET AL. Interference effects in heavy W'-boson searches at the LHC. *Phys. Rev.* D85 (2012), 115017. DOI: `10.1103/PhysRevD.85.115017`. arXiv: `1110.0713 [hep-ph]`.

[31] Pappadopulo, D., ET AL. Heavy vector triplets: bridging theory and data. *Journal of High Energy Physics* 2014, 9 (Sept. 2014). ISSN: 1029-8479. DOI: `10.1007/JHEP09(2014)060`. URL: `http://link.springer.com/ 10.1007/JHEP09(2014)060` (visited on 07/14/2017).

[32] Chanowitz, M. S., AND Gaillard, M. K. The TeV physics of strongly interacting Ws and Zs. *Nucl. Phys.* B 261, 3 (1985), 379–431. URL: `http://cds.cern. ch/record/423907`.

[33] Lefèvre, C. The CERN accelerator complex. Complexe des accélérateurs du CERN. Dec. 2008. URL: https://cds.cern.ch/record/1260465.

[34] *CERN | Accelerating science.* URL: https://home.cern/ (visited on 11/25/2017).

[35] Evans, L., AND Bryant, P. LHC Machine. *JINST* 3 (2008), S08001. DOI: 10.1088/1748-0221/3/08/S08001.

[36] Myers, S., AND Picasso, E. The design, construction and commissioning of the CERN large Electron–Positron collider. *Contemporary Physics* 31, 6 (1990), 387–403. DOI: 10.1080/00107519008213789. eprint: https://doi.org/10.1080/00107519008213789. URL: https://doi.org/10.1080/00107519008213789.

[37] Herr, W., AND Muratori, B. Concept of luminosity (2006). URL: https://cds.cern.ch/record/941318.

[38] *The Large Hadron Collider | CERN.* URL: https://home.cern/topics/large-hadron-collider (visited on 11/25/2017).

[39] LHC Guide. Mar. 2017. URL: https://cds.cern.ch/record/2255762.

[40] Collaboration, T. A., ET AL. The ALICE experiment at the CERN LHC. *Journal of Instrumentation* 3, 08 (2008), S08002. URL: http://stacks.iop.org/1748-0221/3/i=08/a=S08002.

[41] Collaboration, T. L., ET AL. The LHCb Detector at the LHC. *Journal of Instrumentation* 3, 08 (2008), S08005. URL: http://stacks.iop.org/1748-0221/3/i=08/a=S08005.

[42] The ATLAS Collaboration The ATLAS Experiment at the CERN Large Hadron Collider. *Journal of Instrumentation* 3, 08 (2008), S08003. URL: http://stacks.iop.org/1748-0221/3/i=08/a=S08003.

[43] The CMS Collaboration The CMS experiment at the CERN LHC. *Journal of Instrumentation* 3, 08 (2008), S08004. URL: http://stacks.iop.org/1748-0221/3/i=08/a=S08004.

[44] *The CMS hadron calorimeter project: Technical Design Report.* Technical Design Report CMS. CERN, Geneva, 1997. URL: http://cds.cern.ch/record/357153.

[45] *The CMS magnet project: Technical Design Report.* Technical Design Report CMS. CERN, Geneva, 1997. URL: https://cds.cern.ch/record/331056.

[46] Chatrchyan, S., ET AL. The performance of the CMS muon detector in proton-proton collisions at $\sqrt{s}$ = 7 TeV at the LHC. *JINST* 8, CMS-MUO-11-001. CMS-MUO-11-001. CERN-PH-EP-2013-072 (June 2013). Comments: Submitted to JINST, P11002. 101 p. URL: http://cds.cern.ch/record/1558674.

[47] Khachatryan, V., ET AL. The CMS trigger system. *JINST* 12, 01 (2017), P01020. DOI: 10.1088/1748-0221/12/01/P01020. arXiv: 1609.02366.

[48] The CMS Collaboration *Good Luminosity Section Files from CMS*. URL: `https://cms-service-dqm.web.cern.ch/cms-service-dqm/CAF/certification/Collisions16/13TeV/` (visited on 02/02/2018).

[49] Sjöstrand, T., ET AL. An Introduction to PYTHIA 8.2. *Comput. Phys. Commun.* 191 (2015), 159–177. DOI: `10.1016/j.cpc.2015.01.024`. arXiv: `1410.3012 [hep-ph]`.

[50] Khachatryan, V., ET AL. Event generator tunes obtained from underlying event and multiparton scattering measurements. *Eur. Phys. J.* C76, 3 (2016), 155. DOI: `10.1140/epjc/s10052-016-3988-x`. arXiv: `1512.00815 [hep-ex]`.

[51] Alwall, J., ET AL. MadGraph 5 : Going Beyond. *JHEP* 06 (2011), 128. DOI: `10.1007/JHEP06(2011)128`. arXiv: `1106.0522 [hep-ph]`.

[52] Alwall, J., ET AL. Comparative study of various algorithms for the merging of parton showers and matrix elements in hadronic collisions. *Eur. Phys. J.* C53 (2008), 473–500. DOI: `10.1140/epjc/s10052-007-0490-5`. arXiv: `0706.2569 [hep-ph]`.

[53] Nason, P. A New method for combining NLO QCD with shower Monte Carlo algorithms. *JHEP* 11 (2004), 040. DOI: `10.1088/1126-6708/2004/11/040`. arXiv: `hep-ph/0409146 [hep-ph]`.

[54] Frixione, S., ET AL. Matching NLO QCD computations with Parton Shower simulations: the POWHEG method. *JHEP* 11 (2007), 070. DOI: `10.1088/1126-6708/2007/11/070`. arXiv: `0709.2092 [hep-ph]`.

[55] Alioli, S., ET AL. A general framework for implementing NLO calculations in shower Monte Carlo programs: the POWHEG BOX. *JHEP* 06 (2010), 043. DOI: `10.1007/JHEP06(2010)043`. arXiv: `1002.2581 [hep-ph]`.

[56] Alioli, S., ET AL. NLO single-top production matched with shower in POWHEG: s- and t-channel contributions. *JHEP* 09 (2009), 111. DOI: `10.1007/JHEP02(2010)011,10.1088/1126-6708/2009/09/111`. arXiv: `0907.4076 [hep-ph]`.

[57] Re, E. Single-top Wt-channel production matched with parton showers using the POWHEG method. *Eur. Phys. J.* C71 (2011), 1547. DOI: `10.1140/epjc/s10052-011-1547-z`. arXiv: `1009.2450 [hep-ph]`.

[58] Campbell, J. M., ET AL. Top-Pair Production and Decay at NLO Matched with Parton Showers. *JHEP* 04 (2015), 114. DOI: `10.1007/JHEP04(2015)114`. arXiv: `1412.1828 [hep-ph]`.

[59] Alwall, J., ET AL. The automated computation of tree-level and next-to-leading order differential cross sections, and their matching to parton shower simulations. *JHEP* 07 (2014), 079. DOI: `10.1007/JHEP07(2014)079`. arXiv: `1405.0301 [hep-ph]`.

[60] Frederix, R., AND Frixione, S. Merging meets matching in MC@NLO. *JHEP* 12 (2012), 061. DOI: `10.1007/JHEP12(2012)061`. arXiv: `1209.6215 [hep-ph]`.

[61] CMS Collaboration Cross section calculation for leptonically decaying W at NNLO QCD and NLO electroweak. CMS Internal CMS-AN-2014/263. 2014.

[62] Bondarenko, S. G., AND Sapronov, A. A. NLO EW and QCD proton–proton cross section calculations with mcsanc-v1.01. *Computer Physics Communications* 184, 10 (2013), 2343–2350. ISSN: 0010-4655. DOI: https://doi.org/10.1016/j.cpc.2013.05.010. URL: http://www.sciencedirect.com/science/article/pii/S0010465513001707.

[63] Quackenbush, S., ET AL. W physics at the LHC with FEWZ 2.1. *Computer Physics Communications* 184, 1 (2013), 209–214. ISSN: 0010-4655. DOI: https://doi.org/10.1016/j.cpc.2012.09.005. URL: http://www.sciencedirect.com/science/article/pii/S0010465512002913.

[64] Butterworth, J., ET AL. PDF4LHC recommendations for LHC Run II. *Journal of Physics G: Nuclear and Particle Physics* 43, 2 (Feb. 1, 2016), 023001. ISSN: 0954-3899, 1361-6471. DOI: 10.1088/0954-3899/43/2/023001. arXiv: 1510.03865. URL: http://arxiv.org/abs/1510.03865.

[65] CMS Collaboration PDF Uncertainties and K-factor Calculations for the SSM W' at 13 TeV Collisions. CMS Internal CMS-AN-2014/240. 2014.

[66] CMS Collaboration Search for new physics in the lepton and MET final state with 2016 data. CMS Internal AN/2016/204. 2017.

[67] Sirunyan, A. M., ET AL. Particle-flow reconstruction and global event description with the CMS detector. *JINST* 12, 10 (2017), P10003. DOI: 10.1088/1748-0221/12/10/P10003. arXiv: 1706.04965 [physics.ins-det].

[68] Khachatryan, V., ET AL. Performance of Electron Reconstruction and Selection with the CMS Detector in Proton-Proton Collisions at $\sqrt{s}$ = 8 TeV. *JINST* 10, 06 (2015), P06005. DOI: 10.1088/1748-0221/10/06/P06005. arXiv: 1502.02701 [physics.ins-det].

[69] Adam, W., ET AL. Reconstruction of Electrons with the Gaussian-Sum Filter in the CMS Tracker at the LHC (2005).

[70] Bethe, H., AND Heitler, W. On the Stopping of Fast Particles and on the Creation of Positive Electrons. *Proceedings of the Royal Society A: Mathematical, Physical and Engineering Sciences* 146, 856 (Aug. 1, 1934), 83–112. ISSN: 1364-5021, 1471-2946. DOI: 10.1098/rspa.1934.0140. URL: http://rspa.royalsocietypublishing.org/cgi/doi/10.1098/rspa.1934.0140 (visited on 11/22/2017).

[71] The CMS Collaboration *EgammaIDRecipesRun2 < CMS < TWiki*. URL: https://twiki.cern.ch/twiki/bin/view/CMS/EgammaIDRecipesRun2 (visited on 01/04/2018).

[72] The CMS Collaboration *WorkBookMetAnalysis < CMSPublic < TWiki*. URL: https://twiki.cern.ch/twiki/bin/view/CMSPublic/WorkBookMetAnalysis (visited on 11/19/2017).

[73] The CMS Collaboration *IntroToJEC < CMS < TWiki*. URL: `https://twiki.cern.ch/twiki/bin/view/CMS/IntroToJEC` (visited on 11/19/2017).

[74] Sun, M. *Achieving the optimal performance of the CMS ECAL in Run II*. Tech. rep. CMS-CR-2016-325. Geneva: CERN, Nov. 2016. URL: `http://cds.cern.ch/record/2233637`.

[75] The CMS Collaboration *EcalSlewRateMitigation < CMS < TWiki*. URL: `https://twiki.cern.ch/twiki/bin/viewauth/CMS/EcalSlewRateMitigation` (visited on 11/17/2017).

[76] The CMS Collaboration *ECAL DPG meeting (7 December 2016) Â· Indico*. URL: `https://indico.cern.ch/event/590956/` (visited on 11/17/2017).

[77] Adzic, P., ET AL. Reconstruction of the signal amplitude of the CMS electromagnetic calorimeter. *The European Physical Journal C - Particles and Fields* 46, 1 (July 2006), 23–35. ISSN: 1434-6052. DOI: `10.1140/epjcd/s2006-02-002-x`. URL: `https://doi.org/10.1140/epjcd/s2006-02-002-x`.

[78] Sam Harper *EGamma report at PPD General Meeting (3 August 2017) Â· Indico*. URL: `https://indico.cern.ch/event/657763/` (visited on 11/17/2017).

[79] The CMS Collaboration *MissingETOptionalFilters < CMS < TWiki*. URL: `https://twiki.cern.ch/twiki/bin/viewauth/CMS/MissingETOptionalFilters` (visited on 11/21/2017).

[80] The CMS Collaboration *MissingETOptionalFiltersRun2 < CMS < TWiki*. URL: `https://twiki.cern.ch/twiki/bin/viewauth/CMS/MissingETOptionalFiltersRun2` (visited on 11/21/2017).

[81] Laurent Thomas *2016 Beam Halo Filter Update at MET Working Group Meeting (27 April 2016) Â· Indico*. URL: `https://indico.cern.ch/event/518559/` (visited on 11/21/2017).

[82] Halil Saka *HCAL Noise and Noise Filters in 2016 at Run Organization Meeting: Calorimeters Data Jamboree (27 May 2016) Â· Indico*. URL: `https://indico.cern.ch/event/534040/` (visited on 11/21/2017).

[83] Kenneth Remington Call *EcalDeadCellTriggerPrimitiveFilter and Variations on 2015D data at MET Working Group Meeting (9 March 2016) Â· Indico*. URL: `https://indico.cern.ch/event/502965/` (visited on 11/21/2017).

[84] The CMS Collaboration *SusyEcalMaskedCellSummary < CMS < TWiki*. URL: `https://twiki.cern.ch/twiki/bin/view/CMS/SusyEcalMaskedCellSummary` (visited on 11/22/2017).

[85] Isabell Melzer-Pellmann *Report from the MET Scanners atPPD General Meeting (1 December 2016) on Indico*. URL: `https://indico.cern.ch/event/591506/` (visited on 11/21/2017).

[86] The CMS Collaboration *HEEPElectronIdentificationRun2 < CMS < TWiki*. URL: `https://twiki.cern.ch/twiki/bin/view/CMS/HEEPElectronIdentificationRun2?rev=28` (visited on 11/14/2017).

[87] The CMS Collaboration *HEEPElectronID < CMS < TWiki*. URL: `https://twiki.cern.ch/twiki/bin/viewauth/CMS/HEEPElectronID` (visited on 11/15/2017).

[88] The CMS Collaboration Search for high mass di-electron resonances with the full 2016 data. CMS Internal CMS-AN-2016/404. 2017.

[89] *GitLab - aachen-3a / tapas*. URL: `https://gitlab.cern.ch/aachen-3a/tapas` (visited on 01/18/2018).

[90] *GitHub - cms-sw/cmssw: CMS Offline Software*. URL: `https://github.com/cms-sw/cmssw` (visited on 01/18/2018).

[91] Bretz, H.-P., ET AL. A development environment for visual physics analysis. *Journal of Instrumentation* 7, 08 (2012), T08005. URL: `http://stacks.iop.org/1748-0221/7/i=08/a=T08005`.

[92] Bayatyan, G. L., ET AL. *CMS computing: Technical Design Report*. Technical Design Report CMS. Submitted on 31 May 2005. CERN, Geneva, 2005. URL: `http://cds.cern.ch/record/838359`.

[93] The CMS Collaboration *PileupJSONFileforData < CMS < TWiki*. URL: `https://twiki.cern.ch/twiki/bin/viewauth/CMS/PileupJSONFileforData` (visited on 01/12/2018).

[94] *CMS Luminosity Measurements for the 2016 Data Taking Period*. Tech. rep. CMS-PAS-LUM-17-001. Geneva: CERN, 2017. URL: `https://cds.cern.ch/record/2257069`.

[95] Harland-Lang, L. A., ET AL. Parton distributions in the LHC era: MMHT 2014 PDFs. *Eur. Phys. J.* C75, 5 (2015), 204. DOI: `10.1140/epjc/s10052-015-3397-6`. arXiv: `1412.3989 [hep-ph]`.

[96] Rojo, J. PDF4LHC recommendations for Run II. *PoS* DIS2016 (2016), 018. arXiv: `1606.08243 [hep-ph]`.

[97] *Hypernews: Recommended cross section for pile-up reweigthing*. URL: `https://hypernews.cern.ch/HyperNews/CMS/get/luminosity/613/2/1/1/1.html` (visited on 01/03/2018).

[98] The CMS Collaboration Dielectron resonance search in Run 2 at $\sqrt{13}$ TeV pp collisions. CMS Internal CMS-AN-2015/222. 2015.

[99] The CMS Collaboration *JetEnergyScale < CMS < TWiki*. URL: `https://twiki.cern.ch/twiki/bin/viewauth/CMS/JetEnergyScale` (visited on 01/04/2018).

[100] The CMS Collaboration *JECDataMC < CMS < TWiki*. URL: `https://twiki.cern.ch/twiki/bin/view/CMS/JECDataMC` (visited on 01/04/2018).

[101] The CMS Collaboration *JetResolution < CMS < TWiki*. URL: `https://twiki.cern.ch/twiki/bin/view/CMS/JetResolution#JER_Scaling_factors_and_Uncertai` (visited on 01/04/2018).

[102] *MUSiC, a Model Unspecific Search for New Physics, in pp Collisions at $\sqrt{s} = 8$ TeV.* Tech. rep. CMS-PAS-EXO-14-016. Geneva: CERN, 2017. URL: http://cds.cern.ch/record/2256653.

[103] The CMS Collaboration *SWGuideHiggsAnalysisCombinedLimit < CMS < TWiki.* URL: https://twiki.cern.ch/twiki/bin/viewauth/CMS/SWGuideHiggsAnalysisCombinedLimit (visited on 12/19/2017).

[104] *HiggsAnalysis-CombinedLimit: CMS Higgs Combination toolkit.* original-date: 2013-06-21T15:34:08Z. Dec. 12, 2017. URL: https://github.com/cms-analysis/HiggsAnalysis-CombinedLimit (visited on 12/19/2017).

[105] The CMS Collaboration *WebHome < RooStats < TWiki.* URL: https://twiki.cern.ch/twiki/bin/view/RooStats/WebHome (visited on 12/19/2017).

[106] CMS Collaboration Search for high-mass resonances in final states with a lepton and missing transverse momentum at $\sqrt{s} = 13$ TeV. CMS EXO-16-033 PAPER. 2018.

[107] Aaboud, M., ET AL. Search for a new heavy gauge boson resonance decaying into a lepton and missing transverse momentum in 36 fb^{-1} of pp collisions at $\sqrt{s} = 13$ TeV with the ATLAS experiment (2017). arXiv: 1706.04786 [hep-ex].

[108] Materok, Marcel Search for New Physics with high pT tau-Leptons in Run 2 CMS Data. Master thesis. 2017. URL: https://web.physik.rwth-aachen.de/~hebbeker/theses/materok_master.pdf.

[109] Apollinari, G., ET AL. High Luminosity Large Hadron Collider HL-LHC. *CERN Yellow Report* 5 (2015), 1–19. DOI: 10.5170/CERN-2015-005.1. arXiv: 1705.08830 [physics.acc-ph].

[110] Sirunyan, A. M., ET AL. Search for massive resonances decaying into WW, WZ, ZZ, qW, and qZ with dijet final states at sqrt(s) = 13 TeV (2017). arXiv: 1708.05379 [hep-ex].

[111] *Search for heavy resonances decaying to pairs of vector bosons in the l nu q qbar final state with the CMS detector in proton-proton collisions at sqrt s = 13 TeV.* Tech. rep. CMS-PAS-B2G-16-029. Geneva: CERN, 2017. URL: http://cds.cern.ch/record/2296237.

[112] Combination of searches for heavy resonances decaying to WW, WZ, ZZ, WH, and ZH boson pairs in proton–proton collisions at s=8 and 13 TeV. *Physics Letters B* 774 (2017), 533–558. ISSN: 0370-2693. DOI: https://doi.org/10.1016/j.physletb.2017.09.083. URL: http://www.sciencedirect.com/science/article/pii/S0370269317307955.

[113] Kutzner, V. Search for new physics in the mono-electron channel with the CMS experiment in pp collision data at $\sqrt{s} = 13$ TeV. MA thesis. RWTH Aachen U., 2016-06. URL: https://web.physik.rwth-aachen.de/~hebbeker/theses/kutzner_master.pdf.

Danksagung